A Wannier-Stark Optical Lattice Clock With Extended Coherence Times

by

Tobias Bothwell

B.S., University of Arkansas, 2014

A thesis submitted to the

Faculty of the Graduate School of the

University of Colorado in partial fulfillment

of the requirements for the degree of

Doctor of Philosophy

Department of Physics

2022

Committee Members:

Jun Ye, Chair

Prof. James Thompson

Prof. Adam Kaufman

Prof. Ana Maria Rey

Prof. Penina Axelrad

Bothwell, Tobias (Ph.D., Physics)

A Wannier-Stark Optical Lattice Clock With Extended Coherence Times

Thesis directed by Prof. Jun Ye

The pursuit of ever improving accuracy and precision in atomic clocks is inextricably linked to discovery. With each new decade we gain deeper insight into nature, probing ever smaller energy scales. In this thesis we report a body of research advancing our 1D strontium optical lattice clock (Sr1) to the frontiers of accuracy, precision, and atomic coherence. We demonstrate a new record for strontium clock fractional frequency inaccuracy of 2.0×10^{-18}. We then leverage this in a series of comparisons, first comparing Sr1 with the Al^+ and Yb clocks at NIST to 18 digits of accuracy. Intra-lab comparisons with the 3D Sr lattice clock demonstrate record low instability between two independent clocks (3.5×10^{-17} at 1 s). High uptime characterization and steering of Si3 by the Sr1 system further demonstrates a proof of principle all-optical timescale system.

To move into the unknown, we introduce the newest version of Sr1. Utilizing a large waist, in-vacuum build up cavity we radically increase the homogeneity within the clock system. Operation at shallow trap depths allows us to realize a Wannier-Stark optical lattice clock. By tuning the delocalization of atomic wavefunctions we demonstrate the so called 'magic depth', where the clock frequency is free of atomic interaction induced frequency shifts regardless of atom number. Combining these advances in precision we demonstrate a fractional frequency uncertainty of 4.4×10^{-18} at 1 s of operation and 8×10^{-21} after 90 hours of operation, demonstrating nearly a factor of 100 lower uncertainty than the previous record. These advances allow us to rapidly evaluate gradients across our millimeter length atomic sample, resolving the gravitational redshift within a single clock.

Dedication

To my best friend Alex, without whom this would have been impossible.

Acknowledgements

It is impossible to thank everyone who has helped me along this journey, let alone to fully acknowledge everyone's contributions. Nonetheless, I will try.

First and foremost - Jun. Thank you for bringing me into the Ye Lab family and supporting me throughout my graduate career. I have learned more than I knew possible in your group, with each year serving to remind me how much more there is to explore. Leaving, I can't help but be excited for the next adventure!

My time on Sr1 has allowed me the privilege of working with fantastic colleagues. When I first joined the group Xibo Zhang and Sarah Bromley welcomed me. Xibo is an incredibly curious man. Sarah is a dedicated, thorough researcher who can always be relied on to ensure a project's success. The addition of Shimon Kolkowitz's deep scientific thinking and knack for focused problem solving further strengthened the team.

As the original crew left Sr1 I was joined by Dhruv Kedar and Colin Kennedy. Dhruv is a careful, thoughtful scientist who will undoubtedly be a boon wherever he goes. Combined with Colin's go-getter attitude it was quite the energetic environment for physics research. For a period we were joined by the Stable Lasers gurus - Eric Oelker and John Robinson. Any technology sufficiently advanced is indistinguishable from magic, and Eric's mastery of electronics and controls is close. John is one of the most meticulous people I know, with an ability to focus on and solve tasks that others would completely miss. Sr3 is sure to achieve success with him leading the charge. Over the last year I have had the joy of training my replacement - 'Alex Aeppli'. His ability and willingness to take over the operation of the machine made the latter results in this thesis possible.

With the addition of Kyungtae Kim, Sr1 will surely continue to lead the way in the advancement of atomic clocks.

Sr2 has always been near in lab, providing valuable insight into science and life. Throughout my graduate career I have overlapped with Ross Hutson, who seemingly always has a deep, nuanced perspective to offer. I am still only beginning to fully appreciate the wisdom of Aki Goban's advice. Sara Campbell, Ed Marti, Travis Nicholson, Cristian Sanner, Lindsay Sonderhouse, and William Milner all made lasting impressions on my development as a scientist. It will be exciting to watch the results unfold in the coming years with Will taking over Sr2 and Yee Ming Tso and Maya Miklos taking over Sr3.

The community is what makes JILA special. Collaboration through the years with the Rey group has been vital to the research in this thesis. Ana Maria with Anjun Chu and Peiru He were essential in the full realization of density-shift free Wannier-Stark optical lattice clock described in this thesis. James Thompson has been a source of ideas and inspiration, always giving generously of his time. The machine shop, particularly James Uhrich and Hans Green, kept our results moving foward. Jan Thomsen, Matt Norcia, Julia Cline, Tanya Roussy, and the whole KrB crew (you know who you are) were all a joy to exchange ideas with. J.R., Corey Keasling, Brian Lynch, Dan Lewis, and many others provided the support to make all of this possible.

Finally, family and friends kept this thesis going through the highs and lows. Jordan Stone, Dave Reens, and Eddie Meyers all helped keep me sane. My parents (on both sides) were always a font of positivity. My brothers were my brothers. And most importantly - Alex was always there. Also Heidi.

Contents

Chapter

Tables

Table

Figures

Figure

Chapter 1

An Introduction to the Wonderful World Of Clocks

> "The recent discoveries due to the Kinetic theory of gases and to Spectrum analysis (especially when it is applied to the light of the heavenly bodies) indicate to us *natural standard* pieces of matter such as atoms of hydrogen, or sodium, ready made in infinite numbers, all absolutely alike in every physical property. The time of vibration of a sodium particle corresponding to any one of its modes of vibration, is known to be absolutely independent of its position in the universe, and it will probably remain the same so long as the particle itself exists. The wavelength for that particular ray, *i.e.* the space through which light is propagated *in vacuo* during the time of one complete vibration of this period, gives a perfectly invariable unit of length..." (Lord Kelvin [136])

Central to our modern world is an international definition of units - Le Systéme international d'unités (SI). Consider your daily interactions with units that must be agreed upon for your life to proceed smoothly. You wake up to an alarm on your phone, based on an international timescale (the second). You buy food based on volume (the meter) or mass (the kilogram). Your electricity bill is tied to amperes, the speed limit to meters per second, the brightness of your phone to lumens, and your health to pascals. Like it or not, units define our lives!

The International Bureau of Weights and Measures (BIPM) is responsible for directly maintaining and distributing the SI units. The base units of the SI are shown in Figure 1.1 - all other units are derived from them. As of 2019, each base unit is now a defined quantity based on quantum phenomena - our job as metrologists is to then realize these standards with the utmost precision. Importantly, the more precisely we establish the base units the more precisely we realize the derived units.

To illustrate this consider the SI unit of time, the second. It is defined by 9,192,631,770

Figure 1.1: The SI Base units and defining constants. The second is defined by taking the fixed frequency for the cesium hyperfine transition $\Delta\nu$, the meter by defining the speed of light c, the kilogram by defining Planck's constant h, and so forth. All other units are derived from these seven base units.

oscillations of the ground-state hyperfine transition in cesium 133, an idea hearkening back to the opening quote. The fractional uncertainty with which modern clocks define the second has reached the low 10^{-16} level, the most accurate realization of any unit in the SI system. The meter, defined as the length traveled by light in vacuum during $\frac{1}{299792458}$ of a second, relies on our ability to measure the second. Fortunately, the uncertainty in the second is several orders of magnitude smaller than the uncertainty of our ability to determine the refractive index of the medium in which the meter is realized. This illuminates a key motivation for continually improving clocks - we want the accuracy of all units dependent on the second not to be limited by our best realizations. For now this remains true, but improvement of the fractional frequency uncertainty of the world's best cesium clocks has stalled. This suggests we should reconsider the definition of the second, specifically the atomic species and transitions.

So, what is an atomic clock in the simplest sense? Consider a standard clock. An oscillator (pendulum) ticks, the ticks are counted, and the number of ticks readout. An atomic clock can conceptually be broken down into similar pieces. Rather than a mechanical oscillator, our oscillator

is a laser, where the frequency of the electric field provides the ticks. Of course a laser, being a man-made device, is prone to drift so we require a reference. By shining the laser on carefully controlled atoms, we may steer the laser to constantly be at the correct frequency to cause the atoms to vibrate. Should those atoms be cesium (and the laser actually a microwave device) we would be realizing the definition of the second! Finally, we need some way to take our corrected laser and distribute its now highly accurate frequency across the electromagnetic spectrum, from microwave to optical. This is the role of the frequency comb.

Atomic clocks based on optical transitions are the natural candidates for the redefinition of the second. A key figure of merit for a clock is accuracy (Figure 1.2). We parameterize this by a clock's fractional frequency inaccuracy as given by $\frac{\Delta\nu}{\nu}$ where ν is the clock's frequency (number of ticks per second) and $\Delta\nu$ the absolute uncertainty of the clock's frequency. $\Delta\nu$ is usually comprised of two contributions: the statistical uncertainty of the clock (how well we know the frequency after measuring for a period of time) and systematic uncertainty (our limited knowledge of perturbations to the clock's frequency). From the definition of fractional frequency inaccuracy we may understand the advantage of optical clocks in comparison to traditional microwave clocks. For the same absolute frequency inaccuracy, the fractional frequency inaccuracy is decreased by nearly 5 orders of magnitude by moving the clock frequency from the microwave to the optical domain!

Our discussion of $\Delta\nu$ highlights the importance of the second key figure of merit for a clock - precision (Figure 1.2). In atomic clocks the fundamental limit of precision is given by the so called quantum projection noise (QPN)[68] - the inherent quantum noise arising from projecting atoms in a superposition of ground and excited clock states into either ground or excited state upon measurement. The fractional frequency instability of QPN scales as

$$\sigma_{QPN} \propto \frac{S}{\nu_0 T_c}\sqrt{\frac{T_c + T_d}{Nm(T_c + T_d)}}, \tag{1.1}$$

where S is a prefactor dependent on contrast and spectroscopy type (Rabi or Ramsey), T_c the clock

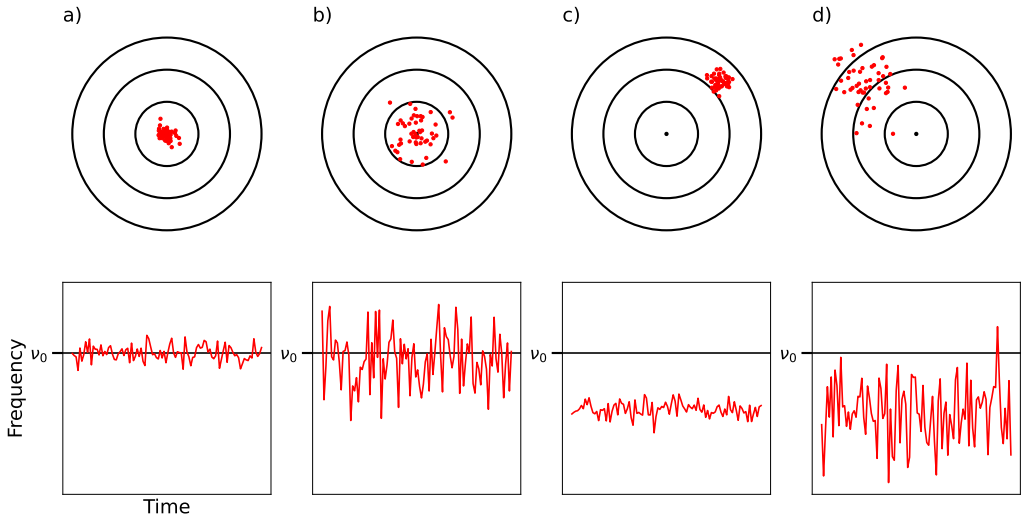

Figure 1.2: Accuracy and precision. The top row shows marks on a target, the bottom row frequency versus time of an oscillator that should be at frequency ν_0. Column a) shows high accuracy and high precision, b) high accuracy and low precision, c) low accuracy and high precision, and d) low accuracy and low precision.

interrogation time, T_d the time spent preparing the atoms for interrogation (atom preparation), ν_0 the clock frequency, N the number of atoms, and m the number of measurements of the clock frequency. This emphasizes the importance of low instability for clocks - our knowlege of the clock frequency only improves as $1/\sqrt{m}$. Consider the most accurate clock to date - the Al^+ clock with fractional frequency inaccuracy of 9.4×10^{-19} [24]. With the Al^+ instability slightly worse than 1×10^{-15} it would take more than 10^6 seconds to reach their reported accuracy! Clearly, for the realistic ability to evaluate these state-of-the-art clocks precision is vital.

Optical lattice clocks (OLCs) are the only platform with sufficient precision to provide a useful frequency reference at these levels of accuracy. Just like ion clocks, OLCs enjoy the benefits of long lived clock states enabling extended interrogation times. In contrast with ion clocks, OLCs can interrogate more than 10,000 atoms simultaneously, reducing the fundamental QPN limit of the clocks by a factor of more than 100. The fundamental motivation of the work in this thesis is the quest to push the 1D Sr OLC to uncertainties at the 10^{-19} level while simultaneously operating

in a regime of high precision. Equation 1.1 tells us that the tools we have at our disposal are extending laser interrogation times and increasing the number of atoms. In the chapters to come we will discuss the research carried out during my graduate career that has culminated in a level of precision capable of evaluating a clocks fractional frequency to 19 digits in 10 s. Critically, this result was obtained in an operational regime fundamentally compatible with accuracy well into the nineteenth decade, successfully wedding next generation accuracy and precision into one experimental platform.

1.1 Why Do We Want Better Clocks?

Let us briefly address the question of why we want better clocks. First and foremost, we want to redefine the second to an optical transition. Doing so will enable orders of magnitude improvement in the accuracy of our realization of the second, ensuring that the second plays no role in the uncertainty of derived units. Additionally, optical atomic clocks have orders of magnitude lower fractional frequency instability, meaning a given level of precision can be attained in orders of magnitude less time! Comparison to an ideal frequency standard should be accurate and rapid, with statistics not limited by the standard. OLCs excel in both metrics.

Improved clocks will allow us to probe the fundamental assumption of the SI units - the immutable nature of fundamental constants. Many beyond Standard Model theories do not guarantee the stability of our nicely defined units. By making better clocks, we can compare them and test these assumptions, ruling out new theories or perhaps some day discovering new physics [123]. Such research requires different atomic species, or at the least different clock transitions within one atom. Comparing two clocks drifting in the same way would reveal nothing, but comparing transitions with differential sensitivity to fundamental constants can open the door to testing a variety of new physics, such as changes in the fine structure constant.

An exciting, evolving frontier of clocks is space based applications. Centimeter scale accuracy in an updated global navigation satellite system wouldn't just improve navigation, but would allow accurate mapping of the Earth's geoid [99]. Deep space navigation is currently hampered by the

ability to send timing signals to distant space vehicles - integration of on-board, highly accurate atomic clocks would remove this limitation. Improvement in clock precision may even some day allow for space-based clocks to detect gravitational waves [77].

Beyond timescales and tests of fundamental constants, improved clocks will have valuable roles in terrestrial applications. Comparison of such clocks on Earth will provide a critical tool for relativistic geodesy at the sub-centimeter level [47]. Advanced communications networks, entangled networks of clocks [78], improved very-long-baseline interferometry - the list goes on!

1.2 1D ^{87}Sr Optical Lattice Clocks

This thesis discusses two generations of the Sr1 project at JILA, both using the 1D ^{87}Sr optical lattice clock (OLC) architecture. We will quickly review the operation of a 1D Sr OLC, referring the extremely curious reader to detailed theses for further in depth discussion [21, 88, 146, 95, 25], with experimental details of the new version discussed in Chapter 4.

Sr is in many ways the Goldilocks of the Alkaline-Earth elements. With atomic number 38, the outermost valence electrons completely fill the $5s^2$ configuration, giving rise to the energy structure shown in Figure 1.3. The two valence electrons may align their spins such that S=0 (singlet state $^1S_0$) or S=1 (triplet states ^3P_J). This has immediate relevance for creating a frequency standard since dipole selection rules in LS coupling [39, 40, 63, 4] tell us that, for an E1 excitation, $\Delta S = 0$. This means in pure LS coupling transitions from $^1S_0 \nLeftrightarrow {}^3P_J$ are forbidden.

Let's turn our attention to the clock transition at 698 nm. This transition is also forbidden by the angular momentum triangle rule (J=0$\not\Rightarrow$J'=0), a significantly more rigorous rule than $\Delta S = 0$ (check the linewidth of the $^3P_1$ versus $^3P_0$ transitions in bosonic strontium). So, our clock transition is doubly-forbidden! How do we drive the clock transition? LS-coupling is an approximation, neglecting spin-orbit coupling (SOC). SOC weakly perturbs the $^3P_0$ state, mixing in small contributions of $^1P_1$ and $^3P_1$ [21]. Even with SOC mixing we can't reliably probe the ultra-narrow bosonic clock linewidth, so we must either 1) apply a large magnetic field to further induce the clock transition or 2) work with the fermionic isotope. In fermionic strontium, ^{87}Sr (I=9/2), the

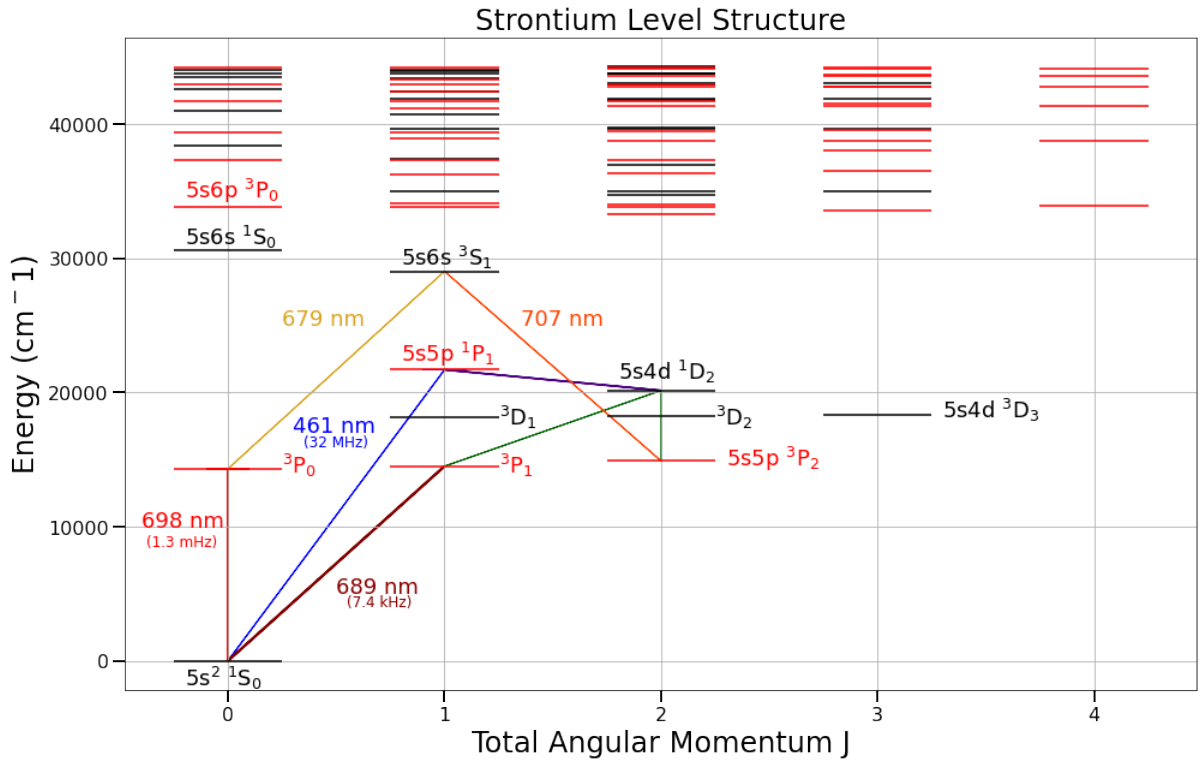

Figure 1.3: Strontium energy levels. Even (odd) parity levels shown in black (red). The strong dipole transition (461 nm) serves for initial cooling and trapping of hot strontium atoms. A weak decay channel from $^1P_1$ to $^1D_2$ (purple line) leads to population in $^3P_1$ and $^3P_2$ (green lines). While $^3P_1$ decays to the ground state, $^3P_2$ is metastable and leads to significant loss. The addition of repumps at 679 and 707 nm ensures cycling of metastable states back to the ground state, enhancing MOT operation and enabling excited state readout. Narrow-line MOT operation at 689 nm is cycling and enables efficient preparation of cold, dense samples of Sr.

hyperfine interaction further perturbs LS coupling, creating an extremely narrow but usable clock linewidth of 1.3 mHz which we use to form our frequency reference [21].

So, we have a doubly forbidden clock transition between two J=0 states, ensuring SU(N) symmetry [12, 25] and suppressing vector related clock shifts. How do we leverage our clock transition as a frequency reference? First we must prepare our atomic sample [21, 88], all within ultra-high vacuum. A small piece of strontium is heated to around 400° C, causing the sample to effuse strontium atoms. The atomic flux is collimated, cooled, and loaded into a magneto-optical trap (MOT) first operating on the 461 nm transition and then a second MOT stage on the 689 nm transition (Figure 1.3). After the second MOT stage the $\sim \mu K$ atoms are loaded in an optical

lattice where further cooling and nuclear spin-polarization may be performed. Atoms are tightly confined to spatial dimensions much less than the wavelength of the lattice light, enabling Doppler-free clock spectroscopy (the so called Lamb-Dicke regime [21, 88]). Critically, the lattice wavelength is such that the ground and excited clock state polarizabilities are identical, preventing deleterious frequency shifts to the clock transition.

Clock spectroscopy proceeds as in Figure 1.4 [88, 111, 112]. Every experiment corresponds to loading atoms, preparing a single nuclear spin, probing the atoms with clock light, and finally reading out the excitation fraction using the 461 nm transition. This is performed on the left and right side of the Rabi lineshape for each nuclear spin transition. Excitation fractions are converted to frequency corrections, which provide feedback to the clock laser. The average frequency of the two nuclear spin transitions rejects vector shifts and is used for tracking the atomic frequency, while the differential frequency between opposite nuclear spin states tracks vector frequency perturbations.

1.3 Thesis Outline

This dissertation discusses experiments probing the frontiers of accuracy, precision, and applications of atomic clocks. All work was performed as part of the Sr1 group at JILA (the 1D strontium optical lattice clock experiment) in close collaboration with the full Ye Lab's Sr team, consisting of Sr2, Sr3, and Stable Lasers.

In Chapter 2 we present the current (2022) record accuracy evaluation for a strontium clock and third most accurate clock demonstrated to date, documenting improvements from the previous Sr1 fractional frequency inaccuracy of 5.3×10^{-17} [17] and Sr2 (1D) inaccuracy of 2.1×10^{-18} [109] to a new inaccuracy of 2.0×10^{-18} in 2019. We notably include an updated accounting of lattice light shifts to account for corrections beyond the dipole approximation.

Chapter 3 gives a brief overview of the studies enabled by this accuracy evaluation. Our advances in accuracy were motivated by our participation in an extensive clock comparison between the Sr1 system and Al^+ and Yb clocks at NIST. With Sr1's improved accuracy and Sr2's precision expertise we were able to demonstrate record low instability inter-clock comparisons between the

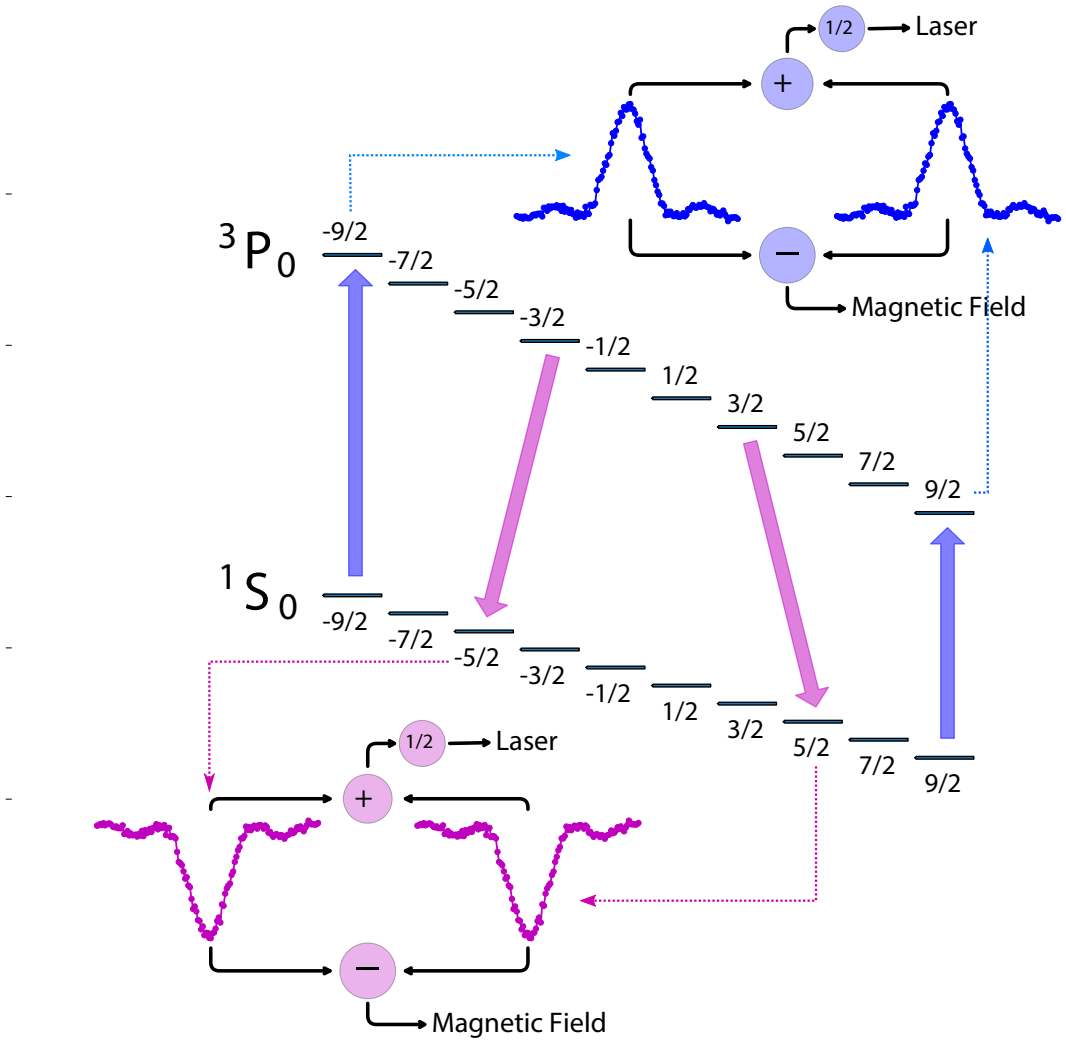

Figure 1.4: Clock spectroscopy of nuclear spin states [112]. Traditional stretched state spectroscopy is shown in blue, where the $|g, m_F = \pm 9/2\rangle \leftrightarrow |e, m_F = \pm 9/2\rangle$ transition is probed. Recent clock operation has become limited by magnetic field noise, necessitating operation with the least magnetically sensitive transition in strontium, $|g, m_F = \pm 5/2\rangle \leftrightarrow |e, m_F = \pm 3/2\rangle$. In each sequence (assuming a perfect atomic reference) 1/2 of the sum of the nuclear spin state transition frequencies corresponds to laser noise while 1/2 of the difference corresponds to magnetic field noise. During spectroscopy the frequency of each nuclear spin transition is found by probing both the left and right of the lineshape, providing a frequency correction based on excitation fraction differences and the corresponding lineshape.

Sr1 and Sr2 clocks. Sr1 was further used to help characterize the labs newest clock laser, Si3, enabling demonstrations of an all-optical timescale and searches for dark matter.

In Chapter 4 we switch gears, discussing the newest iteration of the Sr1 experiment. By

utilizing a large waist in-vacuum build-up cavity for the optical lattice the atomic density is reduced by nearly an order of magnitude, supporting advances in precision owing to large atom-number operation. The ability to initially load and cool the atomic sample in a deep trap enables a new regime of temperatures for the 1D lattice clock architecture, building on the lessons learned from the 3D experiment [33].

Chapter 5 introduces the concept of the Wannier-Stark OLC [81]. Operation at depths near 10 lattice recoil energies results in the delocalization of atomic wavefunctions, enabling engineering of atomic interactions. We demonstrate the ability to operate nearly free of atomic-interaction induced frequency shifts by engineering on- and off-site atomic interactions to cancel, eliminating the largest impediment to precision in the 1D clock platform.

Chapter 6 discusses advancements enabled by combining atomic coherence as demonstrated in the 3D and tweezer platforms [33, 154] with the proven accuracy of the 1D platform [98, 19]. In-situ imaging of the atomic cloud [93] with differential systematic characterization allows us to resolve the frequency gradient arising from the gravitational redshift across a millimeter scale atomic sample. This observation is enabled by record precision, demonstrated by comparing two regions of the cloud for nearly 90 hours allowing frequency resolution of 21 digits.

Finally, Chapter 7 revisits the fundamental limiting systematic of Chapter 2 - the lattice light shift. We discuss the origin of higher order terms in the light shift and outline a possible plan of attach for reducing their uncertainties.

Chapter 2

Record Accuracy For a Strontium Clock

The research in this chapter is reported in the publication: Bothwell et al., 'JILA Sr1 optical lattice clock with uncertainty of 2.0×10^{-18},' Metrologia (2019) [19].

Atomic clocks based on optical transitions have led to rapid advances in clock accuracy. In 2010 the NIST Al^+ clock was the first system to reach a fractional frequency inaccuracy below 1×10^{-17}, evaluating the system to 8.6×10^{-18} [36]. The 1D version of Sr2 became the first OLC to reach this milestone in 2014, achieving an inaccuracy of 6.4×10^{-18} [17]. A year later, in 2015, they further reduced their inaccuracy to 2.1×10^{-18}. Concurrently, Riken performed a comparison of two cyrogenic 1D Sr OLCs with inaccuracies of 7.2×10^{-18}, solidifying Sr as the leading platform. In 2018, the Yb OLC team at NIST similarly compared two clocks with inaccuracies of 1.4×10^{-18} and differential inaccuracy below 1×10^{-18} [98]. PTB's Yb ion clocks have never been far behind, evaluating a clock inaccuracy of 3.0×10^{-18} in 2016 [66] and further improving to 2.7×10^{-19} in 2019. Finally, NIST's Al^+ system reported the current record inaccuracy of 9.4×10^{-19} in 2019 [24].

While the leading clock platform for accuracy has been traded back and forth between ion and OLC, OLCs are the superior platform for precision. The Yb OLC team at NIST demonstrated fractional frequency instability below $1 \times 10^{-16}/\sqrt{\tau}$ (τ being averaging time in seconds) in 2016. A year later, the 3D lattice version of Sr2 compared two regions of their atomic cloud with an instability of $3.1 \times 10^{-17}/\sqrt{\tau}$ [33], a record held until the work presented in Chapter 6. A record low instability comparison between Sr1 and Sr2 of $3.5 \times 10^{-17}/\sqrt{\tau}$ is reported in Chapter 3. These

advances in precision are critical for the ability to faithfully evaluate clock uncertainties of $< 1 \times 10^{-18}$.

2.1 Introduction

The unprecedented levels of stability and accuracy of modern clocks has enabled their use in a variety of applications ranging from the proposed redefinition of the SI second [86, 45, 13], to searches for variations of fundamental constants [43, 144, 122, 74], and increased capabilities for positioning, navigation, and timing applications [44]. However, in order to fully realize the potential for these applications, controlling the temporal drift of systematic offsets poses a potential barrier to control of the system at and below the 10^{-18} level. While it is possible to evaluate the systematic uncertainty of optical clocks at this level, active control of all systematics is now urgently needed [53, 65] to realize a robust optical frequency reference that maintains this level of uncertainty over long time periods. A systematic shift can be measured to an extremely high precision but if it varies significantly over time the clock frequency will appear to drift unless real-time frequency corrections are applied. An alternative approach is to instead control the atom environment to the level where the temporal variations of systematic effects are well within the clock's uncertainty budget and frequency post-corrections need not be applied. This is the guiding principle taken in upgrading the JILA Sr1 optical lattice clock. Here, we demonstrate clock performance where fluctuations in systematic offsets are routinely bounded below 4×10^{-19} for times up to 10^4 seconds.

In implementing these upgrades the systematic uncertainty of the Sr1 clock, last evaluated at 5.3×10^{-17} in 2013 [17], has been improved by more than a factor of 20 to 2.0×10^{-18}. This surpasses the uncertainty record for a strontium optical lattice clock and places this clock among the most accurate clocks in the world [109, 98, 24]. The active control of clock operating conditions, including the thermal environment, allows the clock to run in a robust manner without needing real-time frequency corrections to average to the level of its accuracy. In this paper, we detail the control of each major systematic effect in JILA Sr1.

2.2 Experimental Methods

The experimental sequence begins with a collimated atomic beam of Sr generated from a effusive oven. Atoms of ^{87}Sr in the beam undergo 2D transverse cooling and Zeeman slowing using the broadband 461 nm $^1S_0$-$^1P_1$ transition ($\Gamma = 2\pi \times 32$ MHz). The slowed atoms are then loaded into a magneto-optical trap (MOT) operating on the same transition, and cooled to mK-level temperatures. After 100 ms of loading, the atoms are transferred to a second narrow-linewidth ($\Gamma = 2\pi \times 7.5$ kHz) MOT operating on the dipole-forbidden $^1S_0$-$^3P_1$ line at 689 nm, cooling the atoms to a temperature of 3 μK. The sample is then transferred to a one-dimensional, 813 nm red-detuned optical lattice, which exhibits minimal differential polarizability for the two clock states, and is optically pumped into one of the $|F = \frac{9}{2}, m_F = \pm\frac{9}{2}\rangle$ stretched states of the $^1S_0$ manifold. The lattice is initially loaded at a depth of 180 E_r to maximize the number of captured atoms and is then adiabatically ramped down to a nominal operating depth of 45 E_r (where E_r is the recoil energy associated with the 813 nm trapping light) to minimize the effects of systematic shifts associated with the trapping light.

With state preparation complete, clock spectroscopy is performed on the $\sim$ 1 mHz natural linewidth, 698 nm $^1S_0$ - $^3P_0$ transition using a narrow-linewidth ultrastable laser. A bias magnetic field of 57 μT (570 mG) splits the $|\frac{9}{2}, \pm\frac{9}{2}\rangle$ states by 556 Hz, and the clock transition is interrogated with a 600 ms long π-pulse with polarization collinear with the quantization axis. After interrogation with the clock laser, the resulting excitation fraction is measured by first detecting the ground state population via fluorescence on the 461 nm transition, and then detecting the excited state population by repumping atoms back to the ground state and again collecting fluorescence on the 461 nm transition. This procedure is performed for detunings from resonance of $\pm\frac{\Gamma}{2}$, one-half of the Rabi linewidth, and the resulting difference in excitation fraction specifies the detuning of the clock laser from resonance. By alternately probing the two stretched states, we reject fluctuations in the first-order Zeeman shift arising from magnetic field noise, further details of which are offered in [112].

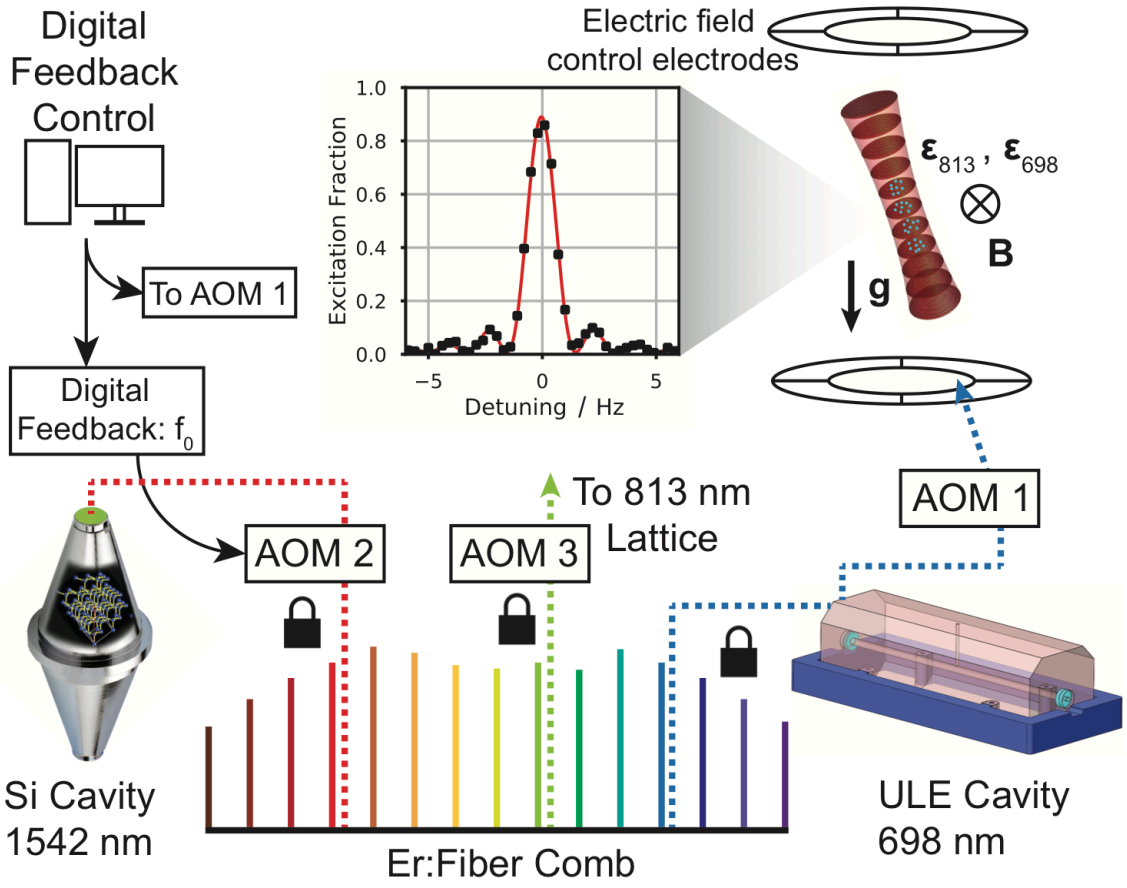

Figure 2.1: **Schematic view of the Sr1 clock**. Ultrastable laser light is generated at 1542 nm by referencing a diode laser to a crystalline silicon optical cavity operating at 124 K (red, dotted line). The stability of this laser is then transferred via an Er:fiber comb to an external-cavity diode laser pre-stabilized by a 40 cm ULE cavity operating at 698 nm (blue, dotted line). An acousto-optic modulator (AOM 1) is then used to steer the cavity light into resonance with the Sr clock transition. The excitation fraction after probing the clock transition is detected by collecting fluorescence from both ground and excited state atoms. A frequency step applied to AOM 1 produces an error signal for locking by alternately probing both sides of the $|\pm 9/2\rangle$ stretched state transitions. Frequency corrections to the average of the $|\pm 9/2\rangle$ frequencies are applied to AOM 2 such that the cavity-stabilized light is steered onto the transition frequency of the Sr atom. In addition, frequency corrections to the difference of the $|\pm 9/2\rangle$ frequencies are applied to the AOM 1 frequency. An in-plane magnetic field, $\mathbf{B}$, providing a quantization axis for the atoms, is aligned to be collinear with both the 1D optical lattice polarization, ϵ_{813}, and the clock laser polarization, ϵ_{698}. Out-of-vacuum quadrant ring electrodes generate a DC electric field to cancel the ambient field at the position of the atoms. Finally, a phase lock of the 813 nm trapping laser to the Er:fiber comb stabilizes the frequency of the trapping light (green, dotted line). The trapping light is delivered to the atoms through a high power optical fiber and is intensity stabilized by actuating the RF power on AOM 3.

As depicted in Fig. 2.1, the ultrastable laser used to probe the clock transition consists of a pre-stabilized 698 nm laser locked to a commercial Er:fiber comb which is phase-stabilized to a master 124 K silicon cavity. A frequency step applied to an acousto-optic modulator (AOM 1 in Fig. 2.1) alternately probes either side of the $|\frac{9}{2}, \pm\frac{9}{2}\rangle$ transitions and generates an error signal. A digital servo filter (PI^2D) is applied to this error signal to apply frequency feedback to AOM 2 in Fig. 2.1. This loop configuration has the effect of stabilizing both the light after the AOM 2 and the frequency of each comb tooth to the spectroscopic precision and accuracy of clock operation. Under typical operating conditions (i.e. sample preparation time of 570 ms, interrogation time of 600 ms, and an atom number of $N = 1000$) the clock achieves a stability of $4.8 \times 10^{-17}/\sqrt{\tau}$ [112].

2.3 Systematic Evaluation

Accurate determination of the unperturbed ^{87}Sr clock transition frequency requires characterization of all systematic effects which produce energy shifts between the $^1S_0$ ground state and the $^3P_0$ metastable excited state. These effects range from the interaction of a single atom with an external field to two-particle collisions and many-body effects. For each shift, the perturbing effect is either directly measured - as in the case of the thermal electric field produced by room temperature radiation - or the effect is inferred by modulation of the applied field and the corresponding measurement of a frequency shift - as in the case of the lattice light shift. Subsequently, the systematic shifts relative to the unperturbed atomic transition frequency can be extrapolated to daily operating conditions using well-characterized theoretical models of each effect.

For shifts evaluated using the lock-in technique, the record-low clock instability demonstrated in Ref. [112] allows the rapid determination of these systematic offsets - without the need to apply a large lever arm - at the 1×10^{-18} level in less than one hour. However, the capability to rapidly evaluate shifts does not preclude the need for applying real-time frequency corrections to compensate for non-stationary systematics. A systematic offset can have temporal variations if its source (e.g. atom number) or calibration (e.g. fluorescence to atom number conversion) fluctuates throughout the day. In the following subsections, we show how, by active stabilization of the thermal

environment and careful control of the operating parameters, drifting systematic offsets can remain below 4×10^{-19} fractional instability over six hours of operation (Figs. 2.2a, b). Consequently, a frequency comparison of the Sr1 clock against a stable reference (the JILA 3D clock [33]), Fig. 2.2c, can average well into the 10^{-19} decade without systematic effects impacting the clock stability.

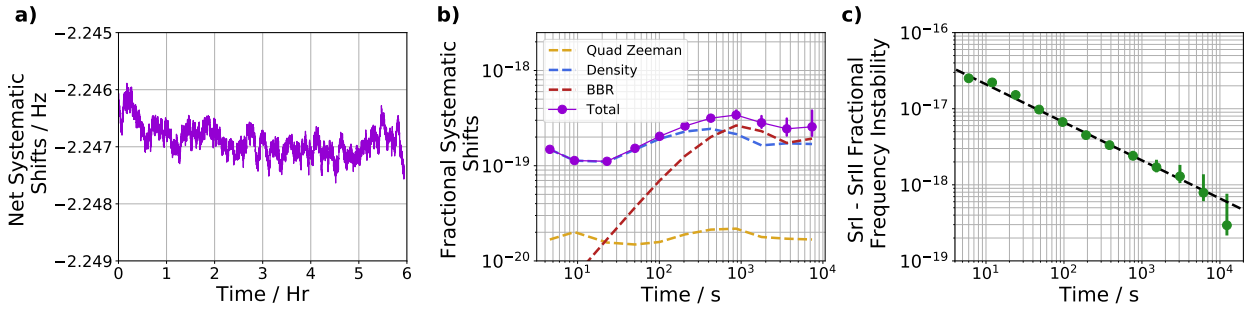

Figure 2.2: **Systematic shifts.** **(a)** Plot of the time record of the systematic shifts. Changes in atom number, ambient temperature, or magnetic field all result in corrections to the clock frequency, and their total magnitude is shown over a six hour data campaign. The clock achieves 98.9% uptime over the course of this single comparison day and slight gaps in the data indicate brief periods where the laser is not locked to the atoms. **(b)** The same data is plotted as a fractional instability normalized to the Sr clock frequency. The individual contributions of density shift (blue), BBR (red) and second order Zeeman shift (yellow) are shown as the dashed curves. For operation times up to 10^4 seconds, fluctuations in systematic offsets are bounded below 4×10^{-19}. **(c)** Nonsynchronous comparison with the JILA 3D optical lattice clock demonstrates that the beat between the two clocks averages below the quoted total systematic uncertainty. All error bars are derived from a white noise model and the black line is a white noise $\tau^{-1/2}$ fit to the single clock instability.

2.3.1 Blackbody Radiation

The frequency shift induced by blackbody radiation (BBR) is the largest systematic shift and a dominant source of uncertainty in state-of-the-art optical lattice clocks. Aside from cryogenic systems [139], the BBR-induced clock shift for strontium is approximately 5×10^{-15} at room temperature. The BBR shift of a thermal electric field distribution characterized by a temperature, T, may be expressed as:

$$\Delta\nu_{BBR}(T) = \nu_{stat}\left(\frac{T}{T_0}\right)^4 + \nu_{dyn}\left[\left(\frac{T}{T_0}\right)^6 + \mathcal{O}\left(\frac{T}{T_0}\right)^8\right] \tag{2.1}$$

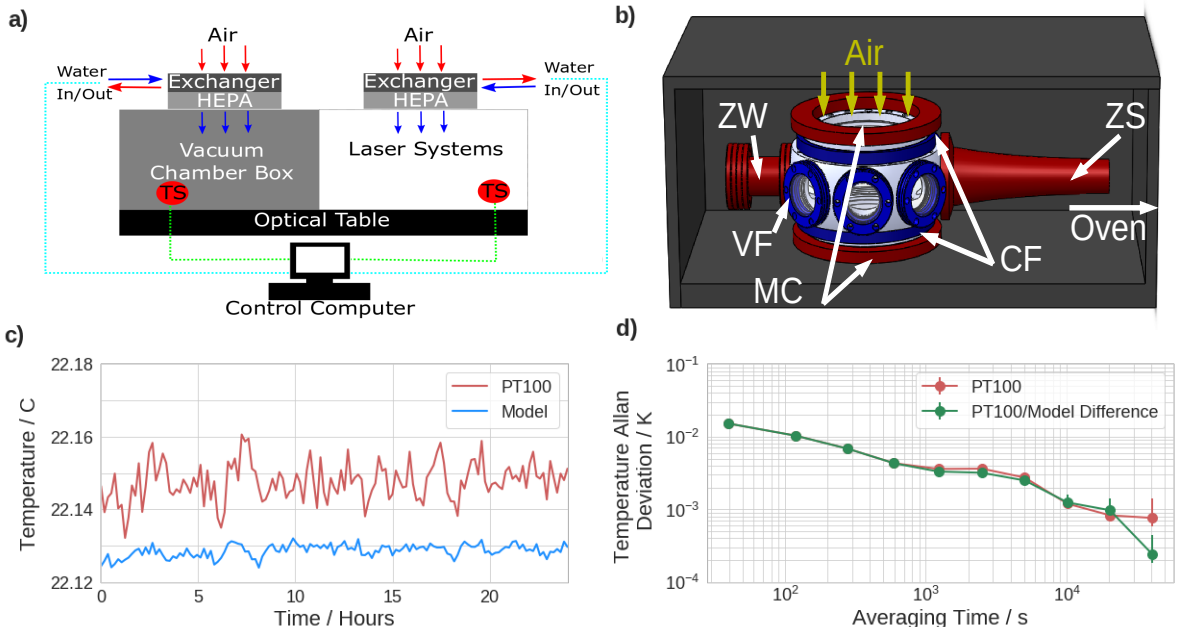

Figure 2.3: **Active Temperature Control. (a)** The optical table is divided into independently controlled sections (grey and white shaded regions) and isolated from the room temperature by a laser curtain. Around the vacuum chamber is an additional black box. Temperature sensors (TS) monitor each table half, allowing feedback (dotted lines) for controlling the flow of cooling water through a water/air exchanger above each table half. Commercial HEPA filters pull room air into the box. **(b)** The Sr1 vacuum chamber is contained in a black box to protect it from stray light and ensure thermal homogeneity. Heat sources that are temperature controlled are shown in red: Zeeman window (ZW), Zeeman slower (ZS), and MOT coils (MC). Temperature control of vacuum viewports is shown in blue: water temperature controlled copper tubes around the top and bottom 6" CF flanges (CF) and thermoelectric cooler (TEC) controlled 2.75" CF viewport faces (VF). The oven (not shown in the figure) is located past the Zeeman slower. The nozzle (6 mm in diameter and 575° C) is the only heated oven component visible to the atoms. **(c)** The temperature at the location of the atomic sample is directly measured using a thin-film platinum resistance thermometer (TFPRT) sensor and compared to a model derived from ray-tracing and temperature sensors mounted on the chamber, verifying the stability afforded by our extensive thermal control. The measurements shown are binned into 10 minute intervals. **(d)** At several hours averaging times the TFPRT shows sub-mK level stability. The difference between the TFPRT and model shows similar temperature stability, providing verification that long-term fluctuations in the temperature experienced by the atoms are accurately captured by the ray-tracing model.

where $\nu_{stat} = -2.13023(6)$ Hz [100], $\nu_{dyn} = -148.7(7)$ mHz [109], and $T_0 = 300$ K.

Characterizing the room temperature BBR shift at the low 10^{-18} level requires absolute knowledge of the thermal environment of the atoms to within 50 mK. To date this challenging technical requirement has been met using two approaches. In the JILA Sr2 clock, NIST-calibrated in-vacuum sensors were used to directly measure the thermal environment of the atoms to an uncertainty of 5 mK [109]. In the Yb OLC at NIST an in-vacuum radiation shield was characterized using precision thermometry and thermal modeling [6]. Here we take components of both approaches by actively stabilizing and monitoring the thermal enclosure of the atoms while also utilizing in-vacuum thermometry.

Our primary objective is to create a frequency reference with low 10^{-18} level systematic uncertainty that does not require point-by-point corrections to attain a similar instability. A homogeneous thermal environment is essential for accurate and precise characterization of the surroundings with a finite array of temperature sensors and for avoiding complications which arise when evaluating the dynamic BBR correction of a non-thermal spectrum of the electric field driven by temperature gradients [109]. Furthermore, actively maintaining a constant operating temperature leads to a more stable and reproducible BBR shift that is crucial for post-correction-free operation of the clock at the low 10^{-18} level.

For our evaluation of the BBR shift in Sr1, we utilized both a Monte-Carlo ray-tracing based thermal model and an in-vacuum thermal probe to determine the temperature at the atoms in two complementary ways. One method involves actively stabilizing and carefully measuring the thermal environment around the vacuum chamber using 16 servo loops and over 30 sensors. The temperature at the atoms can then be computed from this array of temperature monitors using a detailed thermal model based on ray tracing as described in Appendix 2.5.1. We then verify the first approach by installing a PT100 thermal sensor in-vacuum to directly measure the BBR environment. Excellent agreement between the thermal model and the in-vacuum temperature measurement demonstrates that our model accurately predicts changes in the temperature experienced by the atoms from our external vacuum sensors readings at sub-mK levels. Our technical efforts focus on (1) active

temperature stabilization of our system, (2) creating an array of accurate temperature sensors to characterize the thermal boundary conditions, and (3) calibration of an in-vacuum temperature probe. To this end, we improve the overall thermal homogeneity of JILA Sr1 by more than a factor of 10, limiting thermal gradients across the chamber to less than 100 mK.

We construct a model of the temperature T_i at the location of the atoms, modeled by a small spherical surface i, by mapping the measured temperatures on the surrounding surfaces of the vacuum chamber to T_i by:

$$T_i^4 = \sum_j F_{i\to j} T_j^4, \tag{2.2}$$

where the index j enumerates the different surfaces of the vacuum chamber surrounding the atoms and $F_{i\to j}$ is the exchange factor defined as the fraction of total energy emitted by surface i that is absorbed by surface j directly or by reflection [103]. A description of our exchange factors is given in Appendix 2.5.1. In the limit where the chamber temperature is nearly uniform, the uncertainty in T_i can be expressed as

$$\delta T_i \approx \sum_j F_{i\to j} \delta T_j. \tag{2.3}$$

This limit is important for understanding how to prioritize temperature control of the experimental apparatus: surfaces with large exchange factors dominate the thermal environment of the atoms and are subsequently the most important to control. A useful heuristic for identifying the largest exchange factors, and therefore the most critical surfaces for thermal control, is to find the most highly emissive surfaces in the vacuum system subtending the largest solid angles at the location of the atoms. Often, and in our case, these surfaces are large vacuum windows.

To achieve the required temperature uniformity and stability, we began by stabilizing the air temperature around the experimental apparatus (Fig. 2.3a). The optical table is partitioned to isolate the vacuum chamber from the auxiliary laser systems and the entire table is surrounded by curtains to isolate it from the room air temperature fluctuations. Around the vacuum chamber

a black box is installed to provide additional thermal homogeneity and to block stray laser light. The box is made of readily available black hardboard, black acrylic, and aluminum framing. Both sides of the table are actively temperature stabilized by controlling their inlet air temperature. Our chamber has several heat sources including the MOT coils, Zeeman slower, heated Zeeman window, and oven (Fig. 2.3b). Each heat source is accompanied with water cooling such that the relative heating/cooling rate allows us to actively control the steady-state temperature of each.

The equilibrium temperature at the atoms is determined from Eqns. 2.2 and 2.3, which are dominated by the contributions from the fused silica viewports due to their high emissivity and large solid angles with respect to the atomic sample. Therefore, stabilization and accurate measurement of the viewport temperatures is of paramount importance. To stabilize their temperature, we fix the thermal boundary conditions of all viewports (Fig. 2.3b). The stainless steel flanges of the 6" viewports are wrapped in copper tubing carrying temperature controlled water to stabilize the temperature of the steel around the glass. A copper ring with two embedded temperature sensors and lined with thermally conductive silicon matting is pressed against the outer edge of the glass (leaving a small aperture in the middle for optical beams to pass through) to achieve thermal homogeneity across the surface and allow direct monitoring of the glass temperature. All 2.75" viewports are controlled using custom, TEC temperature controlled aluminum attachments backed by water cooling.

This unique approach to active temperature control creates a stable thermal environment where temperature-controlled viewports and flanges act as thermal reservoirs with boundary conditions set by the servo setpoints. All setpoints for temperature control are set to 22°C. To characterize the homogeneity of this thermal environment, 30 witness sensors with accuracy of 50 mK were placed around and on the chamber. Each viewport has an independent witness sensor, with the larger 6" viewports each having two. With the data from this sensor array and a detailed 3D model of the vacuum chamber as inputs to our thermal model, one can now compute the temperature seen by the atoms using Eqn. 2.2.

Upon completion of clock operation, an in-vacuum thermal probe is inserted into the vacuum

chamber in order to directly measure the temperature at the position of the atoms. Placement of the probe at the position of the atoms is ensured by aligning the sensor to overlap with both the clock and the Zeeman slowing laser beams and the temperature is measured under identical run conditions to clock operation. This measurement allows for both the direct verification of the thermal model connecting temperatures measured on the vacuum chamber to the temperature seen by the atoms as well as the reduction of uncertainties associated with the emissivity of different vacuum components. The in-vacuum thermal probe consists of a 60 cm evacuated glass tube with a calibrated ($\pm$1.4 mK) PT100 sensor epoxied at the end. The sensor design and calibration details can be found in Appendix 2.5.2. After installing the in-vacuum sensor, a small static offset of 19.1 mK was discovered between the temperature measured by the zero power resistance of the probe and the temperature derived from the thermal model using parameters given in literature, shown in Fig. 2.3c. This offset is attributed to a limited knowledge of material emissivities as well as calibration uncertainties of the thermistors (50 mK) of the majority of the sensor array. The in-vacuum probe measurement allows for the characterization of any static offset between the thermal model and the directly measured temperatures. Active stabilization of the thermal environment allows this offset to remain stable over clock operation where the thermal model successfully captures all fluctuations in the temperature to better than 1 mK over >10,000 s of averaging as indicated by the Allan deviation of the difference between the model and the measured temperature shown in Fig. 2.3d. All parameters of the thermal model and a more detailed discussion of the construction of the model can be found in Appendix 2.5.1.

The total temperature uncertainty quoted in Table 2.1 has contributions from the calibration uncertainty of the in-vacuum sensor, immersion error, self heating, modification of the thermal environment by the sensor (insertion error), and statistical error of the agreement between the probe and thermal model. Immersion error in the Sr1 chamber was measured by changing the base flange temperature and monitoring the in-vacuum sensor, giving a slope of (0.65 $\pm$ 0.62) mK/K. During clock operation, this flange is controlled to 0.2 K, and so we assign the total immersion error uncertainty to be the quadrature sum of the overall offset and the coefficient

uncertainty, arriving at a 1.8 mK uncertainty. Insertion error is bounded to 1.5 mK from previous work comparing the temperature measured at one thermistor to the temperature measured at another as the position of the second is translated away from the chamber center [109]. The total uncertainty in the temperature of blackbody radiation seen by the atoms is then evaluated to be $\delta T = 2.9$ mK corresponding to an uncertainty of 2.0×10^{-19}. Uncertainty in the combined static and dynamic BBR coefficients accounts for the atomic response contribution to our BBR uncertainty, at 1.49×10^{-18}.

Table 2.1: Atomic Temperature Uncertainty

Shift	Correction (mK)	Uncertainty (mK)
Sensor calibration	0	1.4
Self heating	-1.4	0.3
Immersion error	0	1.8
Sensor - model	20.5	1.0
Insertion error	0	1.5
Total	**19.1**	**2.9**

2.3.2 Density Shift

The high-degree of stability demonstrated by Sr1 and more generally by optical lattice clocks is due to the ability to interrogate thousands of atoms simultaneously and read-out the measured clock frequency with high signal-to-noise at the limit set by quantum projection noise (QPN) [112]. However, the presence of multiple spin-polarized atoms per lattice site introduces systematic frequency shifts due to p-wave interactions. The different triplet collision channels between ground and excited atoms have been shown to have different scattering lengths which subsequently produce density-dependent differential clock shifts. These effects have been studied and characterized in ^{87}Sr [95, 155].

During clock operation, the gas is spin-polarized by optical pumping into either the $|\frac{9}{2}, \frac{9}{2}\rangle$ or the $|\frac{9}{2}, -\frac{9}{2}\rangle$ ground hyperfine state before interrogation in order to suppress frequency shifts due to s-wave collisions. However, s-wave interactions can still occur if impurity atoms remain present after the optical pumping process. To mitigate this effect - and suppress temporal variation of this

effect due to fluctuations in the efficiency of optical pumping - we perform clock spectroscopy on impurity nuclear spin states and optimize the optical pumping process to reduce the population in other nuclear spin states below the detection threshold of our system. In this regime, the dominant density-dependent frequency shift is a collective p-wave interaction between identical fermions.

To reduce the QPN-limited clock stability to the low-$10^{-17}/\sqrt{\tau}$ level, we initially prepare more than 1000 atoms in the optical lattice. For these atom numbers in the deepest optical lattice depths $\sim$180 E_r, on-site densities are high enough that sub-percent-level changes in the trap depth or atom distribution can produce variations of the shift at the 10^{-18} level. The effect of these fluctuations is suppressed to the 10^{-19} level and below by lowering the lattice depth to 45 E_r thereby reducing the peak atomic density during clock interrogation. Vertical orientation of the 1D lattice ensures suppression of tunneling due to the difference in gravitational potential energy between lattice sites.

In addition, fluctuations in the atomic density and the resulting density shift can be driven by changes in the laser-cooling process which transfers the atoms from the narrow-line red MOT into the lattice. This loading process is influenced by the relative frequency, intensity, polarization, and alignment stability of the red MOT lasers. To control these processes, the lasers are stabilized to an ultra-stable cavity to a linewidth of 1 Hz. Temperature stabilization of the experimental apparatus - as discussed in the previous section - serves the dual purpose of stabilizing the alignment of the red MOT and enables robust, alignment-free operation of the clock over many consecutive months. After implementing these measures, we find both the sample temperature and the spatial distribution of atoms in the lattice are insensitive to daily linewidth-level frequency drifts and alignment drifts. Linear scaling of the temperature with the loading lattice depth indicates that final temperatures in the lattice are dominated by the large AC Stark shift of the 813 nm lattice on the $^3P_1$ cooling transition. Since the lattice depth is actively stabilized, the atomic distribution within the lattice remains static over time leading to a density shift with stability at the 10^{-19} level.

To measure and confirm this stability, the density-dependent shift is determined by modu-

lating the atom number by varying the loading time of the blue MOT which then varies the atomic density in the lattice. Care is taken to ensure that, at the highest atom numbers, the spectroscopic lineshape remains Fourier-limited with high peak excitation fraction unblocked by a many-body excitation gap [95]. A model of the density shift which is linearly dependent on atom number is applied to extrapolate the measured shift to the atom number in the lattice on any particular experimental realization. To demonstrate the stability of the shift, repeated density shift evaluations were performed at our nominal clock lattice depth of 45 E_r over the course of several weeks, with a weighted standard error of 3.9×10^{-19} and $\chi^2 = 1.07$ for all these measurements (Fig. 2.4).

Finally, by verifying that the radial and axial trap frequencies in the lattice scale with trap depth as expected for a thermal gas, we confirm the shift scaling of $\Delta\nu_{density} \propto U^{5/4}$ as reported in [132]. Fig. 2.5a shows the result of this evaluation where each point has error bars evaluated to the low 10^{-18} level. The data fits well to a model with the functional form: $a + bU^{5/4}$, where U is the trap depth and a and b are fit parameters. Though we independently measure the density shift for a particular lattice depth each day during clock operation, this scaling becomes highly useful when evaluating shifts at several trap depths, as done during the AC Stark evaluation described in the next section.

2.3.3 Lattice AC Stark

To eliminate Doppler shifts, the atoms are tightly confined in a one-dimensional optical lattice to perform clock spectroscopy in the Lamb-Dicke limit. This confinement induces a differential AC Stark shift between the ground and excited clock states. To minimize this effect, we operate our lattice near the so-called magic frequency where the differential polarizability between the ground and excited states is nearly zero.

To constrain the lattice Stark shift at the 10^{-18} level, recent work has highlighted the importance of accounting for higher-order effects such as hyperpolarizability and the magnetic dipole and electric quadrupole terms [140, 117]. These manifest in light shifts scaling with nonlinear powers in trap depth. Recent work [27] has demonstrated that, given a thermal scaling of axial and radial

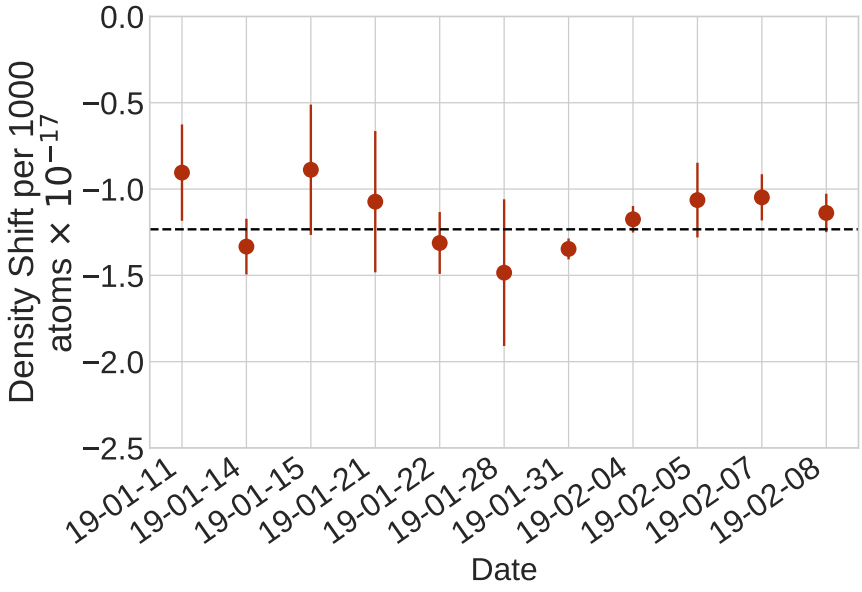

Figure 2.4: **Density shift evaluations.** Density shift measurements were performed over four weeks at the same trap conditions. The weighted mean of all measurements is shown with a dashed, black line, with a reduced chi-squared of 1.07.

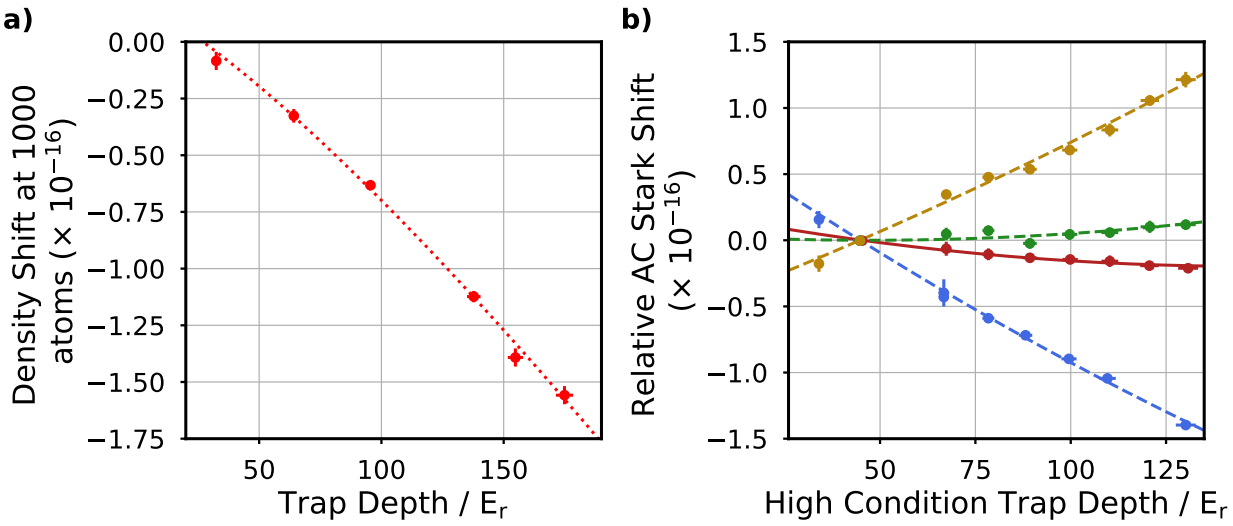

Figure 2.5: **Scaling of the light shift with trap depth** U **(a)** Density shift evaluated at different trap depths, scaled to a shift with 1000 atoms. The dashed red line is a fit to the data with the expected scaling of the shift as $U^{5/4}$. **(b)** Lattice Stark shifts measured relative to a trap depth of $45E_r$. Four different lattice frequencies are shown: $\nu_L = 368.55452610$ (blue), 368.55447610 (red), 368.55446610 (green), and 368.55442610 THz (gold). The three curves with dashed lines are independently fit using the model in Eqn. 2.4, obtaining a weighted mean of their β^*'s. Using this β^*, the red curve is then fit for α^*_{clock}, fully characterizing our AC Stark shifts for clock operation at the red curve. Vertical error bars are obtained from fits to the Allan deviation of each evaluation, extrapolated to the total measurement time, and scaled by the lever arm of the measurement. Horizontal error bars are uncertainties on our determination of the trap depth, obtained from axial sideband scans.

modes with trap depth U, these nonlinear shifts can be greatly simplified to a linear and quadratic term, expressed as:

$$\frac{\nu_{LS}}{\nu} \simeq \alpha^* U + \beta^* U^2. \tag{2.4}$$

Eqn. 2.4 shows that characterization of the lattice light shift requires the measurement of experiment-specific coefficients α^* and β^*. A discussion of the uncertainty associated with the use of this model in the Sr1 system can be found in Appendix 2.6. Note that α^* and β^* not only depend on atomic coefficients, but also on the atomic distribution in both the radial and axial directions. As such, care should be taken to evaluate these coefficients under reproducible sample temperatures and lattice trapping frequencies.

To evaluate the lattice light shift a series of differential measurements of the light-induced frequency shift between a series of lattice depths ranging from 34 E_r to 141 E_r and a reference depth of 45 E_r is performed. These measurements are repeated for four different lattice frequencies, ν_L, encompassing both positive and negative detunings from the magic frequency. This enables accurate determination of ν_L dependent α^*'s and a ν_L independent β^*. The resulting data is shown in Fig. 2.5b. We perform this evaluation by relying on measurement precision as opposed to a large measurement lever arm, enabling us to stay close to the clock operational trap depths and atomic distributions. To remove trap depth dependent density shifts from the lattice light shift evaluations, we perform a series of density shift measurements over a range of lattice depths to which we fit a $U^{5/4}$ model, shown in Fig. 2.5a. The residual uncertainty of the $U^{5/4}$ model fit to the density shift data in Fig. 2.5a is then propagated to the lattice light shift measurements and added in quadrature with the statistical uncertainty of the measurement.

Lattice lights shifts are evaluated at four different lattice frequencies, shown by the four different curves in Fig. 2.5b. The determination of the lattice light shift at the operational lattice frequency proceeds in two steps. First, data from three different lattice frequencies (blue, green, and yellow points) is used to determine the wavelength-independent quantity β^* by least-squares

fitting to the model in Eqn. 2.4. Taking the weighted mean and weighted standard error of the mean of the three β^* values from these fits results in $\beta^* = 1.93(20) \times 10^{-21}$. Second, β^* is then used to fit α^*_{clock} to the data taken at the operational lattice frequency (red points), resulting in $\alpha^*_{\text{clock}} = -5.61(22) \times 10^{-19}$. The total AC Stark uncertainty is found in Tab. 2.2 and includes uncertainties coming from α^* and β^* as well as additional contributions from a 2% uncertainty in trap depth and a model uncertainty. In total, this procedure allows the evaluation of the lattice light shift with a total uncertainty of 1.2×10^{-18}.

To maintain this low uncertainty, we eliminate temporal variations of the lattice light shift. To accomplish this, the trapping light is spectrally filtered and frequency stabilized. First, broadband amplified spontaneous emission (ASE) from the high power Ti:sapphire laser which generates the trapping light is suppressed by reflecting the laser light off two volume Bragg gratings each providing in excess of 30 dB of suppression of ASE power outside the ∼10 GHz wide passband. The Ti:sapphire laser is then phase-locked to an Er:fiber frequency comb which is stabilized to a cryogenic silicon reference cavity [96]. As a result, the drift of the lattice frequency is limited to the low and well characterized drift rate of the cavity (-7.4 Hz/day at 813 nm), which produces negligible drift of the lattice Stark shift. With this stabilization scheme, measurement of the cavity frequency by routine clock operation allows determination of the absolute lattice frequency at the sub-Hz level. In addition, alignment of the lattice polarization to the bias magnetic field and alternately probing the stretched states suppresses the vector contribution and sensitivity to fluctuations in the tensor term. Fluctuations in the relative direction of the magnetic field and the polarization axis are additionally suppressed by the active temperature control of the experimental apparatus with residual background field fluctuations observed at the 100 nT (1 mG) level, corresponding to a shift constrained below the 10^{-19} level. To suppress drifts in the lattice intensity, the laser power is actively stabilized by monitoring the reflection of the incident light from the top surface of the vacuum window. To ensure consistent overlap of the in-going and retroreflected lattice beams, a small amount of power from the retroreflection which is transmitted back through the optical fiber used for beam delivery is monitored to ensure stability of the lattice alignment. Finally, examining

Eqn. 2.4, we see that the light shift is sensitive to fluctuations in the atomic distribution. As covered in the discussion of the density shift, several steps were taken to ensure robustness of both temperature and density and this is reflected in the high reproducibility of the density shift in Fig. 2.4.

Table 2.2: Lattice light shift uncertainty contributions

Parameter	Value (Uncertainty)	Uncertainty (10^{-19})
α^*	-5.61(22) $\times 10^{-19}$	9.7
β^*	$1.93(20)\times 10^{-21}$	4.1
$U(E_r)$	45.0(9)	3.5
Model		3.3
Total		**11.6**

2.3.4 DC Stark Shift

Stray DC electric fields or patch charges on vacuum viewports can induce a frequency shift due to the differential DC polarizability (α_0) between the two clock states. To directly measure this effect with the atoms, a pair of ring electrodes are placed on the top and bottom viewports which have the closest proximity to the atoms. Each ring consists of four copper quadrants which can each be independently biased. By applying a large lever arm of $\pm$100V to the correct combination of electrodes a shift can be measured along any of the three Cartesian axes.

Due to the quadratic dependence of the shift on the total electric field, the magnitude of the background field along each direction can be determined by performing a two-point measurement. We measure $\Delta\nu_+$, the frequency shift when a large field is applied along one direction and compared to the reference case where both electrodes are grounded. The field direction is then reversed and the frequency, $\Delta\nu_-$, is recorded. The direction of the background field, along with its corresponding field amplitude, can then be computed from these two measurements by noting that $\Delta\nu_\pm = -\frac{1}{2}\alpha_0(E_a \pm E_r)^2$ for applied and residual fields E_a and E_r. We observe a modest background field at the low 10^{-18} level in the vertical direction and no clearly resolvable field at the 10^{-20} level along the horizontal axes. By applying ($-$4.2V, +4.2V) to the (top , bottom) electrodes, respectively, we

cancel this background shift to an uncertainty of 2.5×10^{-19}.

2.3.5 Second Order Zeeman Shift

As described in Section 2, the Zeeman shift is cancelled to first order by averaging frequency measurements of the $m_F = \pm\frac{9}{2}$ clock transitions. However, the Zeeman Hamiltonian contains a term with a quadratic dependence on the magnetic field which is not suppressed by this technique. The 57 μT (570 mG) bias field applied to resolve the hyperfine structure of the clock states induces a second order Zeeman shift of ≈ 77 mHz. This shift is typically expressed as

$$\Delta\nu_{B,2} = \xi \left(\Delta\nu_{B,1}\right)^2 \tag{2.5}$$

where ξ is the quadratic Zeeman coefficient for $m_F = \pm\frac{9}{2}$ and $\Delta\nu_{B,1}$ is the first-order Zeeman splitting in Hz between the $m_F = \pm\frac{9}{2}$ transitions due to the applied bias field. Previous uncertainty in the value of ξ introduced a sizeable term in our error budget, motivating a more precise evaluation of the coefficient.

The determination of ξ is complicated by the fact that the observed splitting Δ between the $m_F = \pm\frac{9}{2}$ transitions also contains a contribution from the vector AC Stark shift $\delta\nu \approx 0.4$ Hz. In analogy with $\Delta\nu_{B,1}$, the vector AC Stark term is often thought of as arising from a synthetic magnetic field. We evaluate ξ in the limit where the applied bias field is much larger than this synthetic field so that changing the bias field magnitude does not significantly rotate the total effective field vector. We validate that we are in the appropriate limit by measuring the lattice vector shift directly in an AC Stark evaluation to determine the magnitude of the synthetic field. In this limit, the second-order Zeeman shift can be expressed as $\Delta\nu_{B,2} = \xi(\Delta - \delta\nu)^2$. By performing differential measurements of the clock transition frequency f_0 at three different bias field values, we may determine both ξ and $\delta\nu$ from the following system of equations:

$$f_{0_2} - f_{0_1} = \xi(\Delta_2^2 - \Delta_1^2) - 2\xi\delta\nu(\Delta_2 - \Delta_1)$$
$$f_{0_3} - f_{0_2} = \xi(\Delta_3^2 - \Delta_2^2) - 2\xi\delta\nu(\Delta_3 - \Delta_2) \tag{2.6}$$

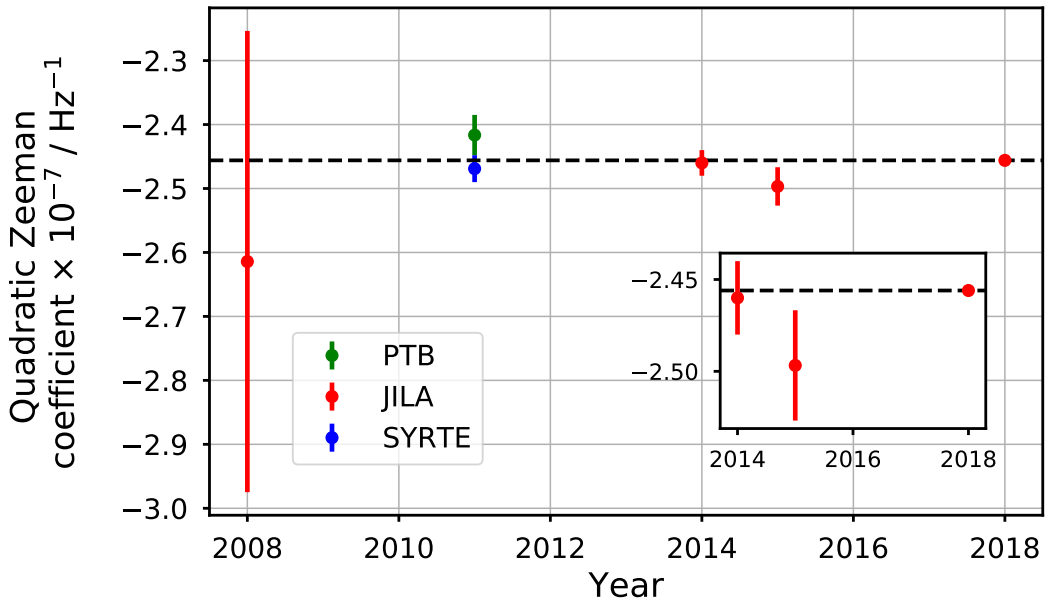

Figure 2.6: **Evaluation of second order Zeeman coefficient.** A history of evaluations of the Sr second order Zeeman coefficient completed by the PTB [45], SYRTE [145], and JILA [30, 17, 109] Sr OLCs. The dashed black line is a weighted mean of all six measurements and the inset shows the three most recent evaluations.

This measurement is repeated at three different sets of bias field values all yielding consistent measurements of ξ. We report the weighted mean of these three evaluations yielding a value of $\xi = -2.456(3) \times 10^{-7}$ Hz^{-1}. Fig. 2.6 shows this result along with historical evaluations showing good agreement with previous measurements. Improved knowledge of this coefficient reduced the uncertainty associated with the second-order Zeeman shift by a factor of 5 to 2×10^{-19}.

2.3.6 Background Gas Collisions

Two-body collisions between a cold ^{87}Sr atom and a room temperature hydrogen molecule or a hot Sr atom emitted by the atomic beam source have the potential to cause a systematic shift. In an uncorrelated thermal gas, a high-energy collision which removes an initially trapped atom from

the sample does not produce a systematic shift. However, atom-light coherence can be affected by collisions with low momentum transfer that produce phase-shifts while leaving the atom trapped. In the process of a collision, the ground and excited states shift differentially as a function of the distance between the Sr atom and its collision partner. When an atom is placed in a superposition of ground and excited states during clock interrogation, the integrated energy difference over the time of the collision produces an undesirable phase shift which appears as a systematic frequency shift varying linearly as a function of the background gas density.

Under ultrahigh vacuum conditions, this frequency shift can be well-approximated by considering collisions between ^{87}Sr and hydrogen molecules [102]. The Sr1 vacuum chamber is stainless steel and contains no getter pump, so the dominant background gas contribution is primarily molecular hydrogen gas. The SYRTE collaboration recently measured a background gas collisional shift of $(-3.0 \pm 0.3) \times 10^{-17}/\tau$ for a hydrogen-limited vacuum lifetime τ [2]. For the Sr1 clock, the lifetime of a dilute sample of ^{3}P$_2$ atoms trapped in the quadrupole field of the MOT is measured to be 8.1(2) s after correcting for BBR-induced decay [152]. The measured lifetime of ground state atoms trapped in the optical lattice is the same as the lifetime in the quadrupole trap [95] and leads to a background gas collisional shift of $(-3.7 \pm 0.4) \times 10^{-18}$.

In addition, two-body collisions with hot Sr atoms emitted from the atomic beam source may also cause a frequency shift. To evaluate this possible systematic shift, an atomic beam shutter is in place to block line of sight to the oven during clock interrogation. The oven flux is increased above the normal operating condition by a factor of 21, and interleaved interrogation of the clock frequency with and without the atomic beam shutter closed is performed. With this lever arm, no significant shift is observed at a measurement precision of 1.0×10^{-18}, therefore bounding the shift at normal operating conditions to below the 10^{-19} level. The shutter is not used for normal clock operation due to intermittent failure of the shutter in the closed position. No difference in atom number or lifetime in the trap is observed with the beam shutter closed versus open.

2.3.7 Doppler Shift and AOM Phase Chirp

For narrow line spectroscopy, Doppler shifts between the clock laser and atoms trapped in the optical lattice are eliminated by active optical path length stabilization [91]. Ideally, the surface which serves as a reference for the laser phase for clock interrogation is the same as the surface which serves as the phase reference for the optical lattice. However, when the clock laser intensity is suddenly changed from zero to a finite value to drive the clock transition, the response of the active stabilization loop experiences transient phase shifts which may impart systematic frequency shifts.

Simultaneous laser phase stabilization and atomic spectroscopy is accomplished with two AOMs – one before an optical fiber that is the actuator for path length stabilization, and a second after the fiber that is the actuator for steering the laser frequency to the atomic resonance. In the 2013 systematic evaluation of the Sr1 clock the stabilization of the laser phase was accomplished by retroreflecting the zeroth order of the second AOM from the mirror to which the optical lattice is referenced while the first negative order was used for atomic spectroscopy. When the clock pulse turns on, this stabilization method produces a differential path length change between the zeroth- and first-diffracted orders due to thermal changes in the AOM crystal. In addition, both differential path length changes driven by air currents between the two diffracted orders and reflections from the tip of the optical fiber add phase noise above the level of the clock laser in the path length stabilization servo.

To circumvent the problems associated with thermal effects in the AOM crystal, fiber tip reflections, and differential path length noise, the path length stabilization scheme is revised such that the first negative diffracted order from the AOM after the fiber is now used for both spectroscopy and path length stabilization – eliminating all differential optical path between the path length stabilization light and the light used for atomic spectroscopy. Mounting a wedged beam sampler to the back surface of the optical lattice retroreflector mirror allows 10% of the incident clock light to be used for path length stabilization. Additionally, Rabi pulses are implemented by

first turning on clock light at a large (1 MHz) detuning for 7 ms and then performing a 3.4 ms ramp onto resonance. This method allows the clock intensity servo to settle before spectroscopy and eliminates all thermally-induced differential path length transients in the AOM crystal. Furthermore, phase transients in the path length stabilization in-loop error signal that arise when operating the servo in a pulsed fashion now occur when the clock light is detuned and the atomic sensitivity function is zero. Eliminating sensitivity to these transients removes a potential source of systematic frequency offsets [46]. The fractional frequency shift due to the linear frequency ramp to resonance is estimated with the Landau-Zener transition probability for the parameters above and is calculated to be 2×10^{-22} for a 600 ms pi-pulse.

2.3.8 Line Pulling

In addition to collisional shifts, off-resonant excitation of an impurity spin population can produce a systematic line pulling frequency shift. The impurity spin population is determined by performing clock spectroscopy on impurity spin states and detecting the number of atoms promoted to the excited state. The total impurity spin population is determined to be less than 0.5%, limited by the detection threshold of the fluorescence measurement. The line pulling effect is subsequently bounded by taking the maximum population in the $\pm|5/2\rangle$ and $\pm|7/2\rangle$ states after dark-state optical pumping and calculating their maximum contributions to the excitation fraction observed on the $\pm|9/2\rangle$ transition. For a 600 ms pi-pulse and a 62 Hz splitting between the $|9/2\rangle$ and $|7/2\rangle$ clock transitions, the maximum off-resonant excitation is given by the ratio of Clebsch-Gordon coefficients squared and the off-resonant Rabi frequency: $(\frac{0.49}{0.82}) \times (\pi/0.6)^2/((2\pi \times 62)^2 + (\pi/0.6)^2) \approx 1 \times 10^{-4}$. Combining the upper bound of the atom number in impurity spin states (0.5%) with this excitation fraction and converting to frequency units, an upper bound on the line pulling effect is set at the 6×10^{-22} level.

2.3.9 Servo Error

The servo error systematic arises from the linear frequency drift of the clock laser that serves as a local oscillator, or from a drifting background magnetic field, producing a systematic bias of the excitation fraction error away from the desired lock point. To minimize this effect, a PI^2D digital servo is used for locking the clock laser to the atomic transition. The servo loop is tuned by optimizing the attack time of the lock error signal with respect to the steering control signal. As a result, for a measurement time of 200000 seconds, a mean servo error of 4×10^{-20} is recorded, which averages to an uncertainty of 2×10^{-19}.

2.3.10 Gravitational Redshift

The gravitational redshift of the clock transition does not effect the systematic uncertainty of the local realization of the clock. However, for accurate comparison of a clock to any other frequency reference the fact that each clock is generally realized at a different gravitational potential must be taken into account as another source of systematic uncertainty. In the absence of another clock to compare to in this work, the clock frequency can be reported relative to an agreed upon reference frame, for example the International Terrestrial Reference Frame (ITRF). In Boulder, a precise characterization of the geopotential of USGS marker Q407 found a clock shift of $179853(6) \times 10^{-16}$ relative to ITRF [115]. Local surveying in Boulder has evaluated the height of the JILA Sr1 in-lab marker (S1B60V1) to be $9.7874(0.0025)\,\mathrm{m}$ below Q407. Accounting for the atom's height relative to S1B60V1 and thus relative to Q407, we find a fractional shift of $178766.4(6.0)10^{-18}$ relative to ITRF. Note that the uncertainty in the gravitational potential in Table 2.4 dominates over the clock systematic uncertainty, and suggests that terrestrial all-optical timescales of the future will be limited by the current knowledge of Earth's gravitational potential.

Table 2.3: Sr1 systematic uncertainty

Systematic	Shift (10^{-18})	Uncertainty (10^{-18})
BBR (environment)	-4974.1	0.2
BBR (atomic)	0	1.5
Density	-12.3	0.4
Lattice AC Stark	-21.3	1.2
DC Stark	0	0.3
Probe AC Stark	0	<0.1
1st order Zeeman	0	<0.1
2nd order Zeeman	-176.9	0.2
2nd order Doppler	0	<0.1
Servo error	0	0.2
Line pulling	0	<0.1
Background gas	-3.7	0.4
AOM phase chirp	0	<0.1
Total	**-5188.3**	**2.0**

Table 2.4: Sr1 uncertainty relative to ITRF

Systematic	Shift (10^{-18})	Uncertainty (10^{-18})
Local systematic uncertainty	-5188.3	2.0
Gravitational shift to ITRF surface	178766.4	6.0
Total shift to ITRF surface	**173578.1**	**6.2**

2.4 Summary

In summary, we demonstrate a significant advance in the characterization of strontium optical lattice clocks resulting in a low systematic uncertainty of 2.0×10^{-18}. In conjunction with its high uptimes as well as the highly predictable frequency evolution of the cryogenic silicon cavity, such a clock will be a core component of an optical timescale. Indeed, the JILA Sr1 clock has already been used in an atom-cavity frequency intercomparison which highlights the long term stability of cryogenic crystalline cavities for timescales applications [101] and the search for time-variation of fundamental constants [123]. As illustrated in Fig. 2.2, fluctuations in systematic offsets are bounded below 4×10^{-19} over 10^4 seconds of operation. We additionally detail a powerful new technique to combat blackbody radiation shifts that provides a stable thermal environment in which in-vacuum thermometry is only needed as calibration of sophisticated temperature modeling. As clocks are pushed into the next decade of accuracy, the ability to remove the temporal variation of systematics will be a highly powerful tool. With the main limitations to our uncertainty being insufficient knowledge of atomic coefficients, this system sets the path for developing strontium optical lattice clocks at the 10^{-19} level.

2.5 Thermal Environment Evaluation

2.5.1 Thermal Modeling

Radiative heat transfer between specular greybody radiators is a well-studied problem in a variety of systems ranging from ovens to satellites [103]. To characterize the thermal radiation experienced by the atoms we must understand the radiative contributions from each surface of the vacuum chamber. We start by modeling the atoms as a small spherical surface, hereafter referred to as the probe, in thermal equilibrium with the vacuum chamber. The temperature T_i of this

surface, or equivalently of the radiation bathing the atoms, is given by

$$\epsilon_i \sigma T_i^4 A_i = \sum_j \epsilon_j \sigma A_j F_{j\to i} T_j^4 \tag{2.7}$$

where j enumerates the surrounding vacuum chamber surfaces, ϵ_j is the surface's emissivity, σ is the Stefan-Boltzman constant, A_j the surface area, and $F_{j\to i}$ the exchange factor. The exchange factor $F_{j\to i}$ is defined as the fraction of total energy emitted by surface j that is absorbed by surface i, either directly or after reflection from any intermediate surfaces. In this language, Equation 2.7 is telling us that at thermal equilibrium, the total power radiated by our modeled atom surface must be equal to the total incoming power from the surrounding vacuum chamber. Similarly, the exchange factors in Equation 2.7 tell us what portion of radiated power from each surrounding surface j is incident on the probe surface.

Using our understanding of the system's behavior at thermal equilibrium we can simplify Eqn. 2.7 significantly. First, energy conservation requires that $\sum_j F_{i\to j} = 1$, meaning all emitted energy must be absorbed by the surrounding surfaces. Second, reciprocity demands that $\epsilon_i A_i F_{i\to j} = \epsilon_j A_j F_{j\to i}$ [103]. This can be understood by considering all of the paths that emitted BBR (rays) can propagate between surfaces i and j - whether the ray goes from i to j or j to i the paths connecting the surfaces are the same. With these two conditions we can simplify Eqn. 2.7 as

$$T_i^4 = \sum_j F_{i\to j} T_j^4. \tag{2.8}$$

Note that the probe temperature no longer depends on the probe surface's emissivity - consistent with Kirchoff's radiation law. Also note that the exchange factors now consider radiation propagating from the probe surface. Once we have the exchange factors we then have the connection between the array of sensors on our vacuum chamber and the temperature experienced by the atoms.

Calculation of the exchange factors is performed using Monte Carlo ray tracing. This begins with a 3D CAD replica of our vacuum system which is broken into several pieces to address the

different temperatures, emissivities, and reflective qualities (specular and diffusive) of each chamber component. From the location of the atoms we propagate rays with random orientations to evenly sample the 4π steradians around the atoms. For each ray we find the intersection of that ray with the vacuum chamber boundary. Each surface has a probability to absorb (emissivity), diffusively reflect, or specularly reflect the incident ray. If a ray is absorbed, the location and surface is recorded. For reflected rays, the new ray direction is found and the process repeated until every ray has been absorbed by a boundary surface. We perform this process for 50 million initial rays to ensure sufficient ray intersections with all surfaces. Specifically, this ensures that the least intercepted surface, the oven nozzle, absorbs more than 1000 rays for sufficient simulation convergence. From this record we calculate what fraction of the total number of rays are absorbed by each surface. This fraction yields the exchange factor for a given component of the vacuum chamber.

The emissivity and specular reflectivity values used in the ray tracing analysis are given in Table 2.5 and Table 2.6 respectively. Uncertainties of these parameters may result in the small static offset between the temperature determined by a ray-tracing model and the in-vacuum sensor; however, using the calibrated sensor to account for this offset removes the need to propagate uncertainties associated with both emissivities and reflectivities. Our calculated exchange factors are given in Table 2.7. With these values we can evaluate the temperature at the atoms using Eqn. 2.8. We find a stable offset between our model and the temperature measured with our in-vacuum thermometer as illustrated in Fig. 2.3d.

Table 2.5: Emissivities of vacuum chamber components

Surface	Emissivity
Viewports (glass)	0.91 [135]
Vacuum chamber (stainless steel)	0.08 [5, 148]
Sapphire	0.54 [150]
Oven nozzle	0.82 [119]

Table 2.6: Specular steel reflectivities based on [11]

Component	Specular Reflectivity
Polished Chamber	0.95
Other Steel Surfaces	0.1

Table 2.7: Vacuum chamber generalized exchange factors

Component	Exchange Factor
Heated sapphire window	8.81×10^{-4}
2.75" CF viewport glass - extended flanges	1.47×10^{-2}
2.75" CF viewport glass - direct flanges	1.18×10^{-1}
6" CF viewport glass	5.39×10^{-1}
Glass cell	1.08×10^{-3}
Metal chamber, tubing, and slower	3.26×10^{-1}
Oven nozzle	2.15×10^{-5}

2.5.2 Temperature Sensor Calibration

In order to calculate the temperature at the atoms using Eqn. 2.8, an array of sensors to monitor the temperature of various points on the vacuum chamber is required. This array is composed of commercially available 50 kΩ negative temperature coefficient thermistors (US Sensor PR503J2), specified by the manufacturer to be accurate to within 50 mK. Due to the relative importance of the 6" CF viewports (exchange factor of 0.539) to the thermal model, the calibration of the thermistors on these viewports is improved to a 13 mK uncertainty via comparison to a thin-film platinum resistance thermometer (TFPRT) calibrated to fixed-point realizations of the ice melting point and the gallium melting point.

Figs. 2.7a and 2.7b show typical melt curves and associated Allan deviations for both the gallium ice and water ice phase transitions as measured by a TFPRT. The ITS-90 temperature scale defines these melting plateaus to be at temperatures of 29.7646°C (302.9146 K) and 0°C (273.15 K), respectively, allowing for the calibration of the TFPRT - up to systematic uncertainties - at these points. The 2 mK offset from 0°C in our ice point cell is a consequence of performing our calibration measurements at an elevation of 1650 m above sea level [61]. Dissolved air in water serves to suppress the ice point temperature at sea level, where the ice melting point corresponds

to 0°C by definition. Upon applying this known correction, the dominant uncertainty at 22°C is then the unknown non-linearity of the TFPRT between the two fixed point temperatures. After calibration of these crucial thermistors, this array of 50 kΩ thermistors is used as inputs to the thermal model. Using these inputs in conjunction with literature values for the different emissivities of the materials which compose the vacuum chamber, shown in Table 2.5, a real-time prediction for the temperature seen by the atoms is generated.

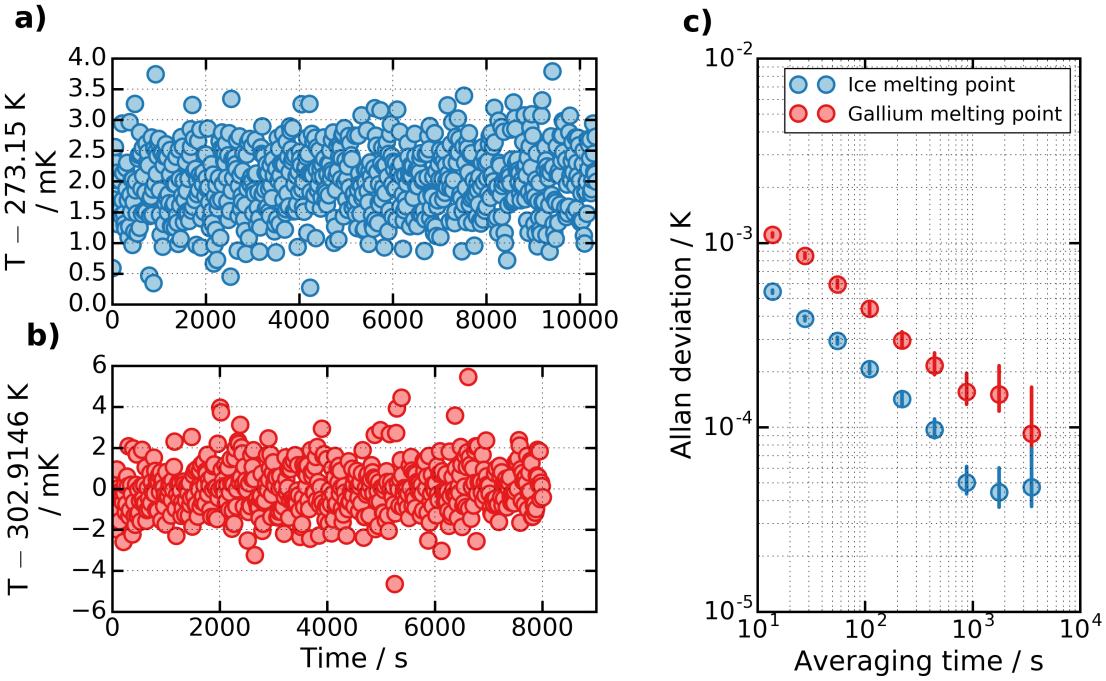

Figure 2.7: **JILA fixed-point realizations.** Data from the **text(a)** water ice melting point and **(b)** gallium melting point realization. **(c)** Allan deviation of the gallium melt curve (red) and the ice melt curve (blue), showing the capability of averaging down to below 100 μK on each fixed-point in 10^4 seconds or less.

As discussed in the main text, in order to evaluate the accuracy of the prediction generated by the ray-tracing-based thermal model, a TFPRT is installed at the position of the atoms in the vacuum chamber. This in-vacuum thermometer allows the characterization and removal of a static offset between the thermal model and the measured temperature and also serves as verification that the thermal model successfully captures all fluctuations in the temperature below the level of 1 mK. In order to achieve an accurate measure of the in-vacuum temperature from the TFPRT,

the probe was hand-carried to NIST Gaithersburg for calibration in the Sensor Sciences Division facilities. There, a water bath comparison calibration with Standard Platinum Resistance Thermometers (SPRT) traceable to the ITS-90 temperature scale enabled the in-vacuum thermometer to be calibrated to an uncertainty of 1.4 mK.

Fig. 2.8b shows the different contributions to the final sensor uncertainty. Immersion error is the largest systematic effect, arising from heat flow between the room temperature environment and the probe, producing a systematic temperature difference between the TFPRT and the bath. To characterize this effect, a second TFPRT is mounted on the upper flange of the test chamber, which lies just above the water line of the bath. To evaluate immersion errors in the water bath calibration, two sets of measurements were undertaken, one under vacuum conditions ($< 3 \times 10^{-6}$ Torr), and another under 30 Torr of back-filled helium. Figure 2.8a shows the measured difference in zero power resistance for these two conditions as a function of the temperature gradient between the flange and the bath, $T_{flange} - T_{bath}$. The immersion error is well-described by a linear function of temperature, with a fitted $T_{flange} - T_{bath} = 0$ systematic offset of (0.3 $\pm$ 0.4) mΩ, which can be converted to (0.69 $\pm$ 1.1) mK. Since the offset is consistent with zero, we simply take the standard uncertainty of 1.1 mK as the immersion error contribution, plotted as the green line in Figure 2.8b. We also include the bath homogeniety as the largest observed gradient as indicated by the two SPRT's in the bath of $\pm$ 0.5 mK, shown as the cyan line. The calibration coefficient uncertainties are shown as the blue and orange curves. The red line shows the sum of all other minor errors, including SPRT calibration, bridge nonlinearity, resistance standard and bath stability [134]. We also account for the offset of 3.0 mK between ITS-90 and the definition of thermodynamic temperature, and it's corresponding uncertainty of 0.3 mK is included in the minor errors [134].

2.5.3 BBR Dynamic Shift Correction

The dynamic BBR shift is described by

$$\Delta\nu_{dynamic} = \nu_{dyn}\left(\frac{T}{T_0}\right)^6. \tag{2.9}$$

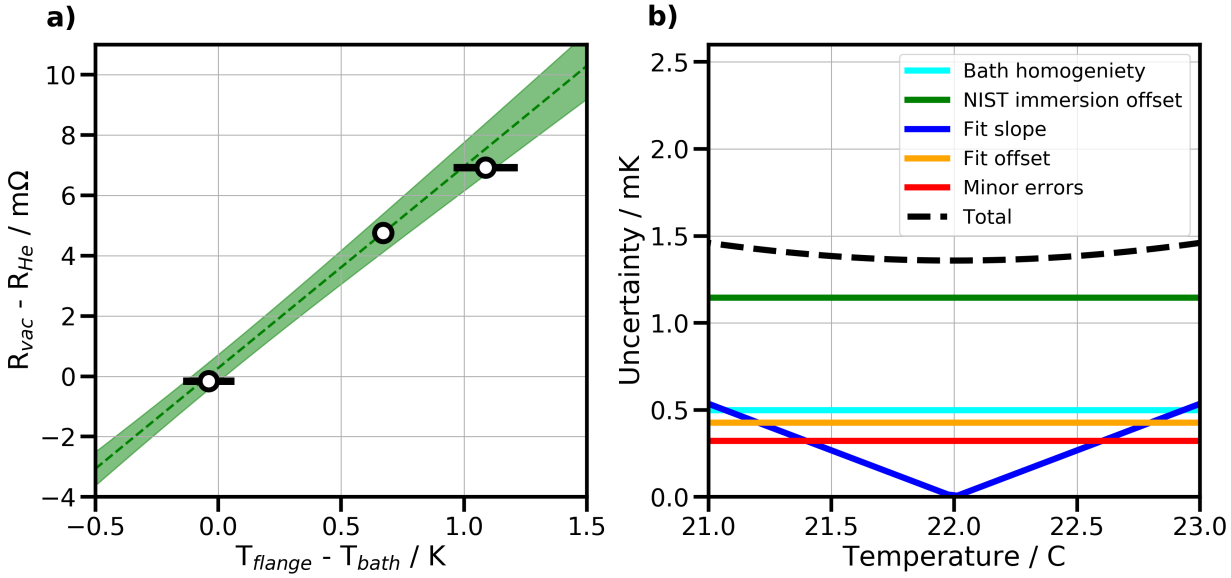

Figure 2.8: **Calibration of the in-vacuum probe. (a)** Immersion error data in the water bath comparison. We measure the difference between the high vacuum resistance R_{vac} and the He back-filled case R_{He} as a function of axial gradient $T_{flange} - T_{bath}$. The data is fit to a linear function, and the fitted offset at zero axial gradient is (0.3 ± 0.4) mΩ. This can be converted to temperature by using the sensitivity of the TFPRT of 2.57 Ohms/Kelvin. **(b)** Breakdown of uncertainties stemming from the NIST calibration. The green is the systematic error in the immersion error offset from panel (a). The cyan color is the maximum temperature gradient observed in the bath. The blue and orange curves are the fit interpolation errors from the slope and offset respectively. The red line is the quadrature sum of several minor errors relating to the calibration. The black dashed line is the quadrature sum of the errors.

Care must be taken since the often reported value of ν_{dyn} contains higher order terms in T (T^8 and T^{10}) [124]. The reported coefficient ν_{dyn} therefore requires corrections for temperatures deviating away from $T_0 = 300$ K. For our temperature near 22°C, we find we must correct our dynamic BBR shift by an amount of 1.48×10^{-18}.

2.6 Lattice Light Shift Evaluation - Model Uncertainty

Optical lattice clocks have reached an accuracy level where higher order polarizability terms require careful consideration. Two separate approaches have dealt with this to high accuracy. At NIST, the Yb clock group [27] demonstrated that in a system where the spatial modes have certain scalings with trap depth the lattice light shifts can be well characterized by a so-called thermal model, containing effective terms that are linear (α^*) and quadratic (β^*) in U:

$$\Delta\nu_{AC} = \alpha^* U + \beta^* U^2. \tag{2.10}$$

The dipole polarizability α_{E1} and multipolarizability α_{QM} are contained in α^* while the hyperpolarizability β is contained in β^*. This approach is robust as it does not require explicit knowledge of atomic coefficients or the axial and radial atomic mode numbers. A second approach is to work on a microscopic model, where for a given radial temperature and axial mode occupation a light shift can be calculated [140]. While a microscopic model offers the prospect of accuracy below the 10^{-18} level, it requires significantly more input information, a potential source of systematic errors in reporting atomic coefficients. Recent work [107] has highlighted this importance by illustrating that different methods of preparing the atomic sample can result in different measurement values of β in Yb.

For determining the operational light shift in the Sr1 clock the thermal model is employed. This avoids reliance on atomic coefficients and characterizes an experiment-specific light shift model. The characterization in the main text discusses the results of the fitting of the thermal model to the data. The limitation to this analysis is that it requires addressing model error - deviations

from linear and quadratic behavior in light shifts that are described by the microscopic model. To address the deviations from linear and quadratic scalings in the Sr1 light shifts we adopt the approach in [27], writing the light shift as:

$$\frac{\Delta\nu_{\mathrm{AC}}}{\nu_{\mathrm{clock}}} = -A_n\alpha_{\mathrm{E1}}U - B_n\alpha_{\mathrm{QM}}U - C_n\beta U^2 \tag{2.11}$$

where A_n, B_n, and C_n are spatial averages given by

$$A_n = \left\langle \mathbf{n} \middle| \exp\big(-\frac{2(x^2+y^2)}{w_0^2}\big)\cos^2(kz) \middle| \mathbf{n} \right\rangle$$
$$B_n = \left\langle \mathbf{n} \middle| \exp\big(-\frac{2(x^2+y^2)}{w_0^2}\big)\sin^2(kz) \middle| \mathbf{n} \right\rangle$$
$$C_n = \left\langle \mathbf{n} \middle| \exp\big(-\frac{4(x^2+y^2)}{w_0^2}\big)\cos^4(kz) \middle| \mathbf{n} \right\rangle.$$

The $\frac{1}{e^2}$ beam radius is given by w_0, the lattice wavenumber by k, and $|\mathbf{n}\rangle = |n_x, n_y, n_z\rangle$ where n_i is spatial coordinate i's mode number. To address gravitational sag resulting from the $\theta = 19°$ tilt with respect to vertical in the lattice, the component of gravity (g) along $\hat{x}$ is included by substituting $x \to x - mg\sin(\theta)/\omega_r^2$ where ω_r is the radial trapping frequency.

The gravitational tilt lifts the radial degeneracy so A_n, B_n, and C_n are broken into orthogonal bases such that $A_n = A_{nx}A_{ny}A_{nz}$, $B_n = B_{nx}B_{ny}B_{nz}$, and $C_n = C_{nx}C_{ny}C_{nz}$, expanding each to

fourth order. The system is then described by following series of equations:

$$\gamma = \frac{g^2 \sin^2(\theta)}{w_0^2 \omega_r^4} \tag{2.12a}$$

$$A_{nx} = 1 - \frac{\sqrt{2}}{w_0 k \sqrt{U}}(n_x + 1/2)(1 - 6\gamma) + \frac{3}{2k^2 w_0^2 U}(n_x^2 + n_x + 1/2) - 2\gamma + 2\gamma^2 \tag{2.12b}$$

$$B_{nx} = A_{nx} \tag{2.12c}$$

$$C_{nx} = 1 - \frac{2\sqrt{2}}{w_0 k \sqrt{U}}(n_x + 1/2)(1 - 6\gamma) + \frac{3}{k^2 w_0^2 U}(n_x^2 + n_x + 1/2) - 4\gamma + 4\gamma^2 \tag{2.12d}$$

$$A_{ny} = 1 - \frac{\sqrt{2}}{w_0 k \sqrt{U}}(n_y + 1/2) + \frac{3}{2k^2 w_0^2 U}(n_y^2 + n_y + 1/2) \tag{2.12e}$$

$$B_{ny} = A_{ny} \tag{2.12f}$$

$$C_{ny} = 1 - \frac{2\sqrt{2}}{w_0 k \sqrt{U}}(n_y + 1/2) + \frac{3}{k^2 w_0^2 U}(n_y^2 + n_y + 1/2) \tag{2.12g}$$

$$A_{nz} = 1 - \frac{(n_z + 1/2)}{\sqrt{U}} + \frac{(n_z^2 + n_z + 1/2)}{2U} \tag{2.12h}$$

$$B_{nz} = \frac{(n_z + 1/2)}{\sqrt{U}} - \frac{(n_z^2 + n_z + 1/2)}{2U} \tag{2.12i}$$

$$C_{nz} = 1 - \frac{2(n_z + 1/2)}{\sqrt{U}} + \frac{5(n_z^2 + n_z + 1/2)}{2U}. \tag{2.12j}$$

In the above equations U is the trap depth in units of the photon recoil energy E_r.

To quantify the model error, Eqn. 2.11 is utilized with input data from measured n_i values and α_{QM} from [140]. The axial and radial mode occupation numbers are derived from carrier sideband asymmetry measurements, radial trapping frequencies, and transverse clock spectroscopy [14]. The final two inputs for the model, α_{E1} and β, are evaluated at each point in a two dimensional space of input parameters spanned by plausible values of α_{E1} and β. Limits on these parameters are chosen to encompass the full range of α_{E1} values from the four curves in Fig. 2.5b. Similarly, the range for β is chosen to encompass the weighted mean of values from published literature [109, 145, 140] to one which is consistent with what is observed in Fig. 2.5b. For each pair of α_{E1} and β in this two dimensional space of values, Eqn. 2.4 is used to simulate lattice light shifts over the range of trap depths used in the experimental data. The thermal model from Eqn. 2.4 is then fit to this simulated data. For each set of simulated and fitted curves, the mean and standard

deviation of the difference between the two models is calculated. All mean differences are below 1×10^{-19}, ensuring that the standard deviation of the differences is not overlooking a constant offset between curves. The resulting average of all standard deviation values shown in Fig. 2.9 is 3.3×10^{-19}. This number is thus interpreted as the model error. We note that use of the theory value for α_{QM} [117] provides a lower estimate of model uncertainty.

We additionally investigate the effect of a running wave in our system arising from reflectivity on the viewports. We find that the only nonlinear and nonquadratic additional term provides a negligible 2×10^{-20} level effect.

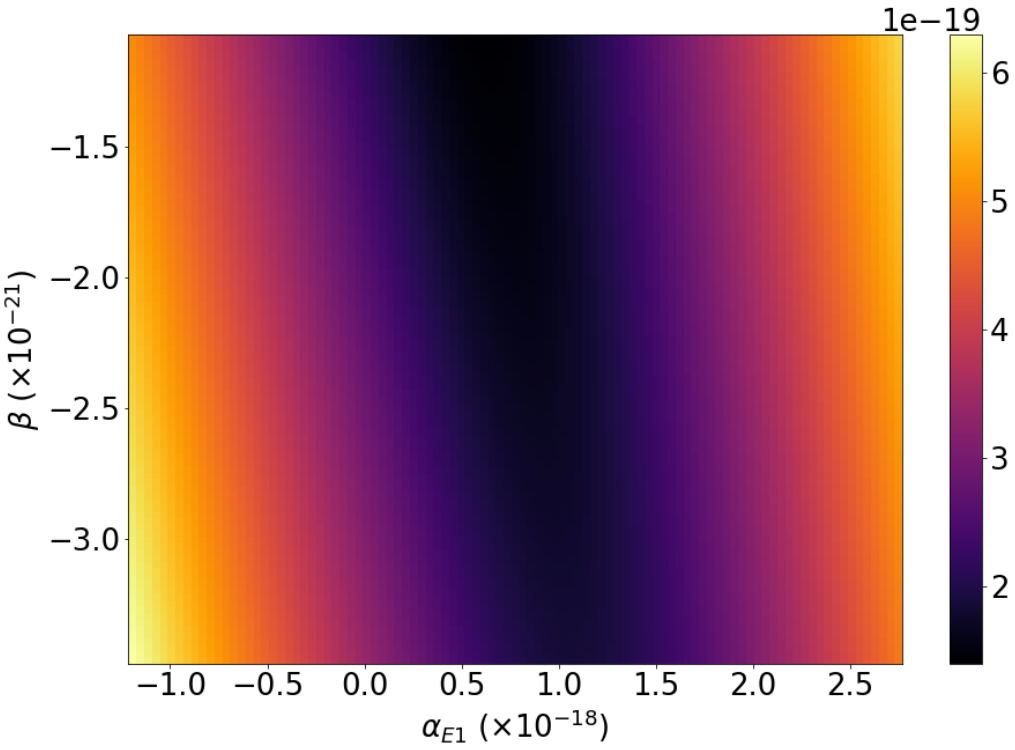

Figure 2.9: **Model Error** Colormap showing the standard deviation between simulated AC Stark data (Eqn. 2.11) and a simple linear and quadratic fit to the data (Eqn. 2.4). The average standard deviation is 3.3×10^{-19} which we take to be our model error.

Chapter 3

Comparisons and Demonstrations

In 2017, we decided to perform clock comparisons between JILA and NIST. At the time, the original JILA Sr2 system with uncertainty of 2.1×10^{-18} had been dismantled and replaced with the 3D lattice clock. The Sr1 system, having been evaluated in 2014 to an uncertainty of 5.3×10^{-17}, was chosen to participate in the frequency comparisons. This motivated the upgrade and systematic reevaluation of the original Sr1 clock as described in Chapter 2, achieving a record low uncertainty of 2.0×10^{-18} for a strontium optical lattice clock and third lowest uncertainty for any atomic clock to date. This prepared the Sr1 system to perform clock comparisons with the two most accurate clocks in the world - the Yb OLC and Al^+ ion clock at NIST. An immediate benefit of systematically characterizing and comparing a state-of-the-art clock is the ability to bootstrap additional research. Sr1 served as a vetted reference for record precision inter-clock comparisons between Sr1 and Sr2 as well as a high up-time reference for an all-optical timescale. This chapter summarizes these results, motivating the idea that accuracy and precision go hand in hand. In the language of quantum information, coherence follows careful quantum state control.

3.1 Towards the Redefinition of the Second

As metrologists a primary objective in the coming decade is to redefine the second to an optical transition. The accuracy and precision of today's best optical clocks are now orders of magnitude better than that of microwave clocks [98, 24, 19, 126, 33, 93, 154], encouraging discussion about how such a redefinition may be done. In 2018 a CIPM working group established a set of

potential criteria for such a redefinition, summarized below [121].

(1) A minimum of three different optical clocks (different labs or species) have validated fractional frequency uncertainties two orders of magnitude lower than the best Cs clocks.

(2) A minimum of three independent measurements of at least one frequency standard from (1) between different institutes at a level of $\Delta\nu/\nu < 5 \times 10^{-18}$.

(3) Three independent measurements of any frequency standard from (1) compared with three independent Cs primary clocks, with uncertainty limited by the Cs clocks.

(4) Candidate frequency standards regularly contribute to international timescales.

These criteria are designed to ensure that a frequency standard is reproducible, consistent with the current Cs definition, and capable of operating as a timescale. An additional criteria was listed in [121]: (5) sufficient frequency ratio measurements between different frequency standards at the level of $\Delta\nu/\nu < 5 \times 10^{-18}$. This criteria is essential to ensure closure relationships. A frequency closure relationship between clocks a,b, and c is defined as

$$C = \left(\frac{\nu_a}{\nu_b}\right)\left(\frac{\nu_b}{\nu_c}\right)\left(\frac{\nu_c}{\nu_a}\right), \tag{3.1}$$

where the level at which one measures 1 provides demonstration of the validity of the standards. Due to the large number of optical secondary frequency standards being considered for a new primary frequency standard, (5) is meant to ensure a smooth transition to a new definition that does not void other standards or lead to inconsistent frequencies at the 5×10^{-18} level.

Criteria (5) is in some sense a political necessity. Today there are numerous optical standards in development, with no standard so far ahead that a redefinition should clearly favor it. Which frequency standard should be chosen? Should a system based on ratios or multiple transitions be used? These are the questions CIPM must debate in the coming decade. Before transportable clocks regularly begin comparing at the 10^{-18} level, such discussions are speculative. Let us instead focus on fulfilling these criteria. In Chapter 2 we fulfilled (1), let's discuss the progress towards (5).

3.2 The Boulder Atomic Clock Optical Network

The Boulder Atomic Clock Optical Network (BACON) is an extensive collaboration comprised of members from both the National Institute of Standards (NIST) and JILA. NIST has two major research clocks (Yb and Al^+), state of the art optical frequency combs (OFCs), and a UTC traceable maser network (Figure 3.1). JILA contains Si3 (critical for connecting the fiber and free-space links), Sr1, Sr2, and the JILA frequency comb. This provides a unique opportunity owing to three of these systems being the three most accurate clocks in the world [98, 24, 19], all within several kilometers. This establishes Boulder as a premier location for high accuracy clock comparisons between three different next-generation frequency standards.

Clock comparisons compare clock frequencies through an optical comb, allowing frequency ratios to be measured. This is critical since the absolute frequency of any of the three BACON clocks would be limited by the realization of the Cs standard, but the ratios of the three clock frequencies can be realized with precision below the accuracy limits of three clocks. To compare Sr to the NIST based clocks, 1542 nm light (from the Si3 clock laser system) is transmitted through a 3.6 km fiber link through the 'Boulder Research and Administration Network' (Figure 3.1). This is a shorter version of similar fiber networks between other national labs, such as in Europe. NIST's expertise provided an additional novel connection between clocks - a free-space link [18]. Using optical two-way time-frequency transfer (O-TWTFT) techniques, signals from optical frequency combs at two locations (NIST and Duane tower at CU) are sent both directions in the link, allowing calibration of common-mode noise from air turbulence. The NIST O-TWTFT OFC is locked to Yb, while the JILA O-TWTFT OFC is locked to Sr, enabling the Yb/Sr ratio to be compared through free-space in addition to fiber, a first for optical comparisons [38].

The systematic tables of the three clocks (and combs) are well described in [38], with the Sr clock being slightly worse than reported in [19]. This is owing to incomplete upgrades/characterizations performed for the accuracy paper, published in 2019, from the ratio data as taken in 2018 for Sr. For the clock comparison, we briefly review the differences. The density shift uncertainty was larger

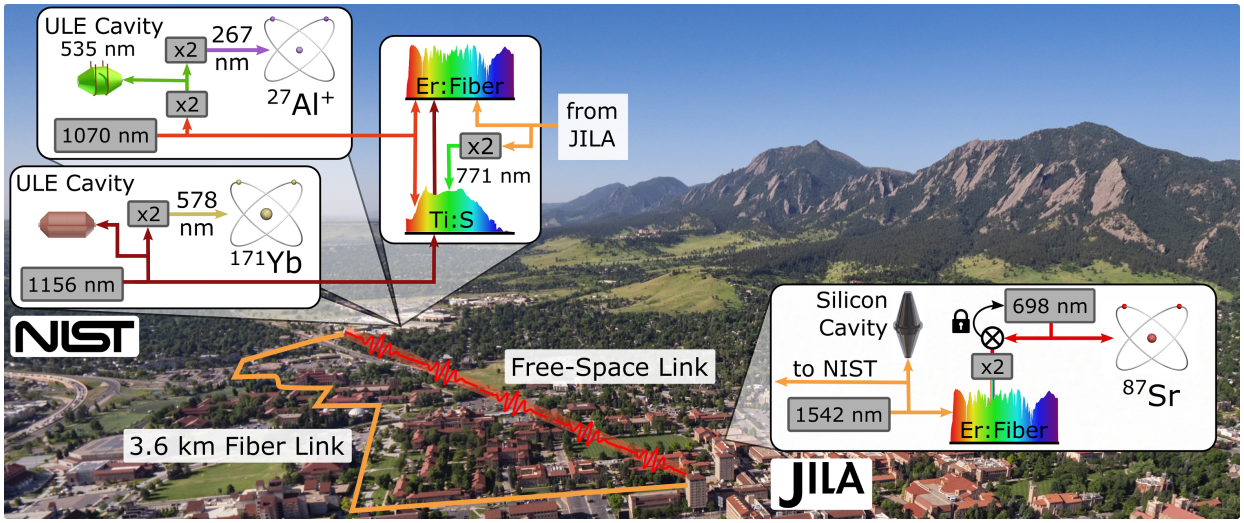

Figure 3.1: Overview of the Boulder Atomic Clock Optical Network (BACON). Network locations at NIST (JILA) are shown in the left (right) of the image. The two institutes are linked both by a 3.6 km fiber link as well as free-space link. NIST is home to the Al^+ ion clock, Yb OLC, and OFCs used for measuring the 3 clock ratios. The Sr clock is located at JILA.

than in [19], owing to a less stable system as well as higher operational trap depth, increasing the density shift per atom. This higher operational trap depth (and uncertainty in daily depth) resulted in a larger uncertainty in the lattice light shifts for Sr1. Thermal conditions were not as stable during the clock comparison, necessitating a modest increase in BBR uncertainty dependent upon the thermal stability during the course of each measurement. Additional temperature uncertainty for aging thermistors (relative to the calibration performed in [19]) was included. Finally, the probe chirp systematic was larger owing to traditional zeroth order retro-reflection, causing an abrupt thermal shock upon Rabi excitation [109].

Over the course of Fall 2017 through Spring 2018 the three clocks were compared. Sr1 was found to have an uncontrolled density shift systematic that prevented inclusion of the Fall 2017 data. The results for each day's clock comparison are shown in Figure 3.2. An example of the data analysis for instability is shown in Figure 3.3.

Analysis of the data shown in Figure 3.2 presented a significant hurdle. Datasets were non-overlapping owing to the downtime of the various clocks. Standard reduced chi-squared analysis presented issues. The Yb/Sr ratio was over scattered, owing to the ability of the lattice clocks to average below their combined uncertainties each day. Meanwhile the Al/Sr ratio was significantly under scattered, an abnormal situation in clock comparisons. To resolve these challenges, a comprehensive Bayesian framework was developed as detailed in [38]. The framework incorporates a fluctuating dark uncertainty, accounting for under reported or unaccounted systematic errors with the assumption of a normal distribution about zero. This allows a Bayesian estimate of the likelihood of observing the measured ratios for a given statistical uncertainty. The results and corresponding uncertainties are:

$$\begin{aligned} \nu_{Al^+}/\nu_{Yb} &= 2.162887127516663703(13), \\ \nu_{Al^+}/\nu_{Sr} &= 2.611701431781463025(21), \\ \nu_{Yb}/\nu_{Sr} &= 1.207507039343337 8482(82). \end{aligned} \tag{3.2}$$

The result of the collaboration was the measurement of three ratios with fractional uncer-

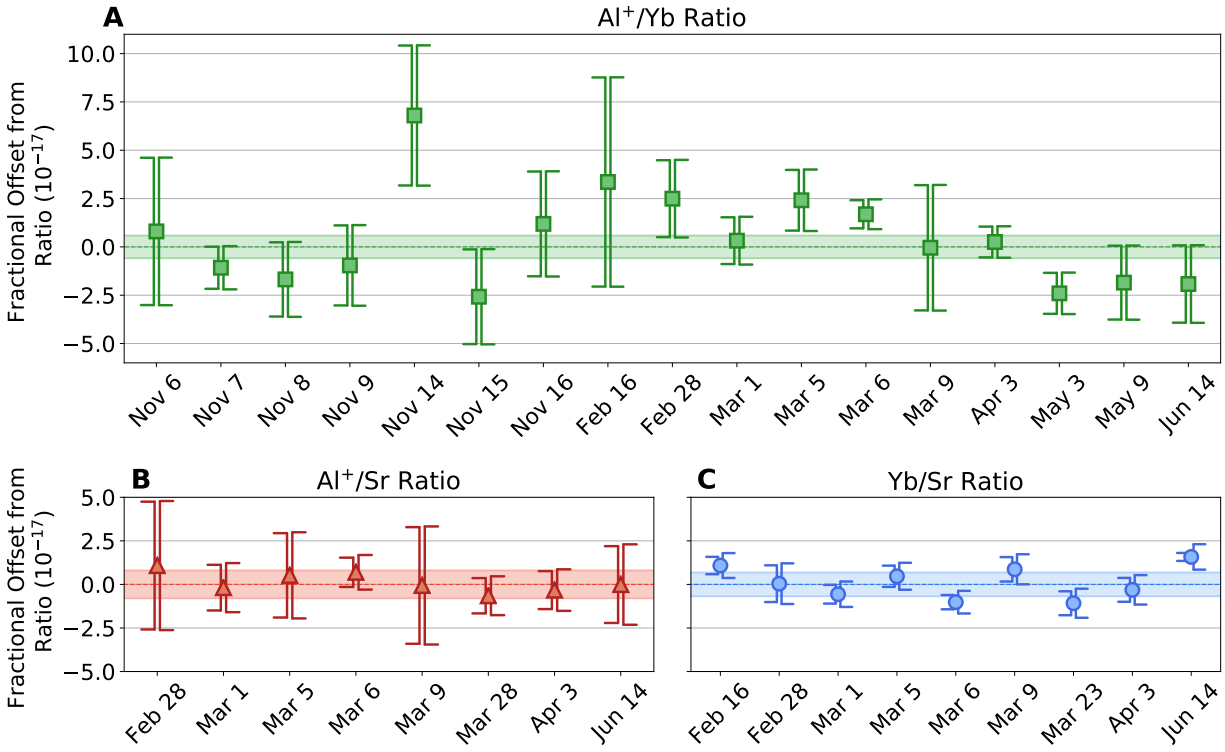

Figure 3.2: Time record of ratio measurements. Frequency ratios were measured from November 2017 to June 2018. Results are shown as fractional offsets from the reported values. Left error bars represent pure statistical uncertainty, whereas error bars on the right include systematic uncertainties added in quadrature to statistical uncertainties.

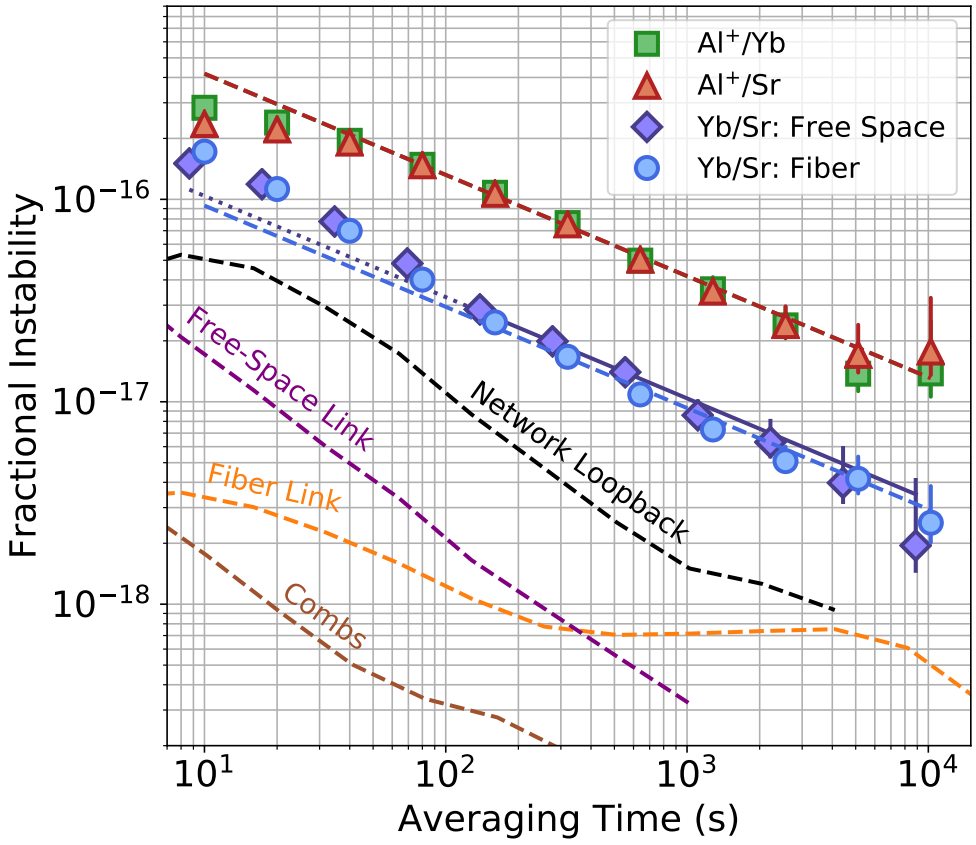

Figure 3.3: Example of daily ratio measurement. Uncertainties for each day are derived from overlapping Allan deviations of the corresponding beat. Instabilities for network elements are shown, all well below the measured instabilities of the atomic ratios.

tainties of 8×10^{-18} or lower. While this fell just fell of the goal of (5), it represented a massive step forward from the previous best ratio measurement of 5×10^{-17} of Yb and Sr in 2015 [108].

3.3 Absolute Frequency

Clock comparison data campaigns provide a wealth of data that can be analyzed for purposes beyond frequency ratios (see the dark matter bounds in [38]). Data taken during the comparison, as measured by NIST's OFCs, links the frequency of each clock to International Atomic Time (TAI), providing a SI traceable absolute frequency measurement of each clock [83, 82]. This absolute frequency calibration work linked the Sr1 clock to Cs through TAI, fulfilling criteria (3). The Sr frequency was found to be [83]

$$\nu_{Sr} = 429,228,004,229,873.19(0.15) \text{ Hz}. \tag{3.3}$$

3.4 Intra-lab Stability

Concurrent with the clock comparison was a major effort by the Stable Lasers team to bring the next-generation cavity system online. In December of 2017, the 21 cm silicon cavity sytem (Si3) became the Ye Lab's newest workhorse. Utilizing a custom commercial comb, the previous laser system dubbed 'MJM' at 698 nm is steered at low frequencies to the Si3 system at 1542 nm [129]. Not only did this radically improve clock precision within the lab, but the 1542 nm light facilitated clock comparisons through the BRAN link owing to the ultra-low loss in the telecom C-band. Throughout the clock comparison, Sr1 not only compared frequencies with NIST, but also served to characterize the long-term stability of the new Si3 system, allowing upgrades such as improved thermal shielding and intensity servos. An example of exemplary Si3 stability data is shown in Figure 3.4.

As the clock comparison finished during the summer of 2018, a major focus became a demonstration of the enhanced stability afforded by the Si3 system. An additional goal was to verify the fractional frequency stability measured via the Sr2 self-synchronous imaging technique (3×10^{-17}

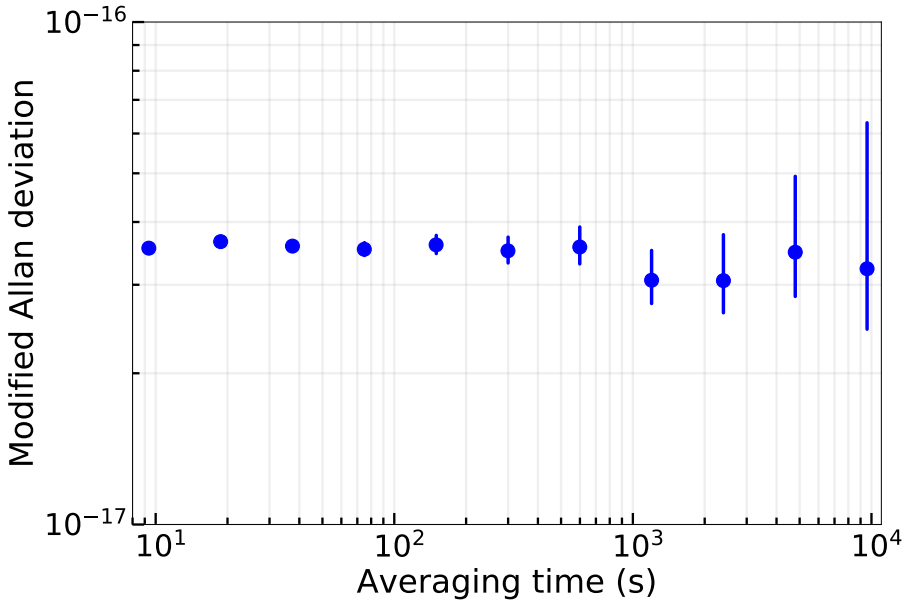

Figure 3.4: Si3 stability. Long-term stability data of Si3 as measured by the Sr1 system showing nearly thermal noise limited stability of just under 4×10^{-17} from 10 to 10,000 seconds.

at 1 s [33, 93]). Critical to this work was combining the vetted accuracy and long term stability of the Sr1 system with the record precision expertise of the Sr2 team.

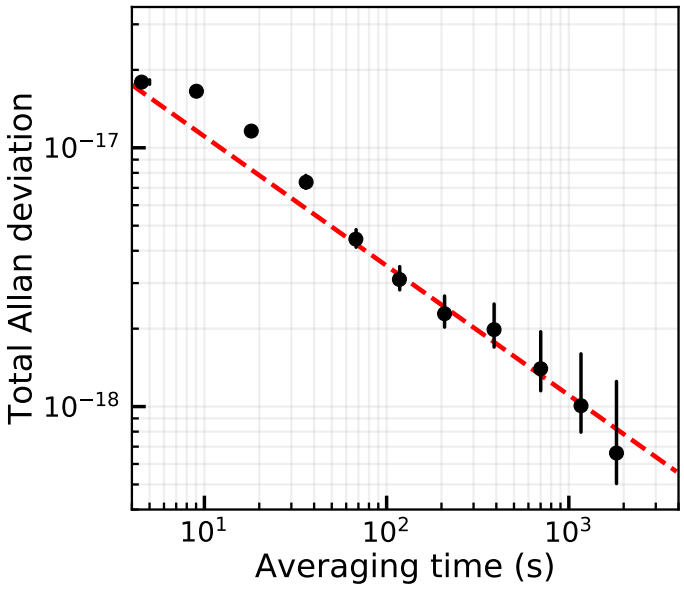

Figure 3.5: Sr1/Sr2 synchronous comparison. Each clock operated with 600 ms π-pulses and 570 ms deadtime, triggering the clock pulse at the same time. The redline corresponds to a fractional frequency instability of $3.5 \times 10^{-17}/\sqrt{\tau}$, consistent with the expected QPN contribution of each clock.

Initial comparisons between Sr1 and Sr2 uncovered several issues. On both systems, fiber noise cancellation was not conducive to stability at $< 10^{-16}$ at 1 s, owing to the differential air path between retro-reflected zeroth order beams and the diffracted clock beam used for clock interrogation. An updated technique, where the clock laser is turned on with a MHz detuning and then swept to resonance, allowed direct retro-reflection of the clock beam used for interrogating the atoms, minimizing differential path noise between FNC and atoms. On Sr1, magnetic field noise was found to limit clock stability, requiring a dedicated effort to find several noisy culprits, most notably a Thor-Labs shutter with moving magnets. Sr2 had similar magnetic field issues, but opted to use the least magnetically sensitive clock transition (see Chapter 1). Finally, Sr2 upgraded their thermal control to prevent flickering from an uncontrolled thermal environment.

With these upgrades, Sr1 and Sr2 were able to compare both asynchronously and synchronously (Figure 3.5). The asynchronous comparison, sensitive to laser noise, was consistent with the Si3 noise model as developed from 3-corner hat comparison with the MJM and Si4 laser systems [112]. The synchronous fractional frequency instability ($3.5 \times 10^{-17}/\sqrt{\tau}$) set a new record for instability between independent clocks, capable of resolving a gravitational redshift of 1 cm in 15 minutes. This improved stability importantly allows fulfillment of the majority of the criteria discussed for the reevaluation of the second in less than 100 s.

3.5 Towards Optical Timescales

Dissemination of current timescales is based on well developed microwave technology linked to Cs standards. While impressive, the accuracy and precision are far off the levels promised by optical clocks. Just as the best clocks now operate in the optical domain, future timescales will also require all-optical operation to avoid degradation of the accuracy and precision of future primary optical frequency standards. Such advances will also benefit microwave stability thanks to the technology of the frequency comb [106].

The development and maturation of cryogenic, crystalline silicon cavity based lasers over the last 10 years [75, 97] has opened the possibility for proof-of-principle demonstrations of all-optical timekeeping. With the consistent, high-uptime operation of Sr1 a long-term record of Si3's frequency and drift rate began to develop. Spurred on by datasets like that shown in Figure 3.4, we realized that Si3 was essentially an 'optical' MASER, with sufficiently well behaved frequency drifts that it could serve as the frequency flywheel for periods where an optical clock isn't running.

To demonstrate the use of silicon cavities as tools for all-optical timescales, the Sr1 clock was operated nearly daily over a 34 day interval, with 25% uptime. By tracking the Si3 frequency both with Sr1 as well as a TAI referenced maser array at NIST (AT1), we were able to compare Si3's performance against the current US civilian timescale. As shown in Figure 3.6, Si3 outperforms AT1 at timescales under 10^5 s, suggesting daily corrections to Si3 using Sr1 should outperform Cs steered MASER arrays.

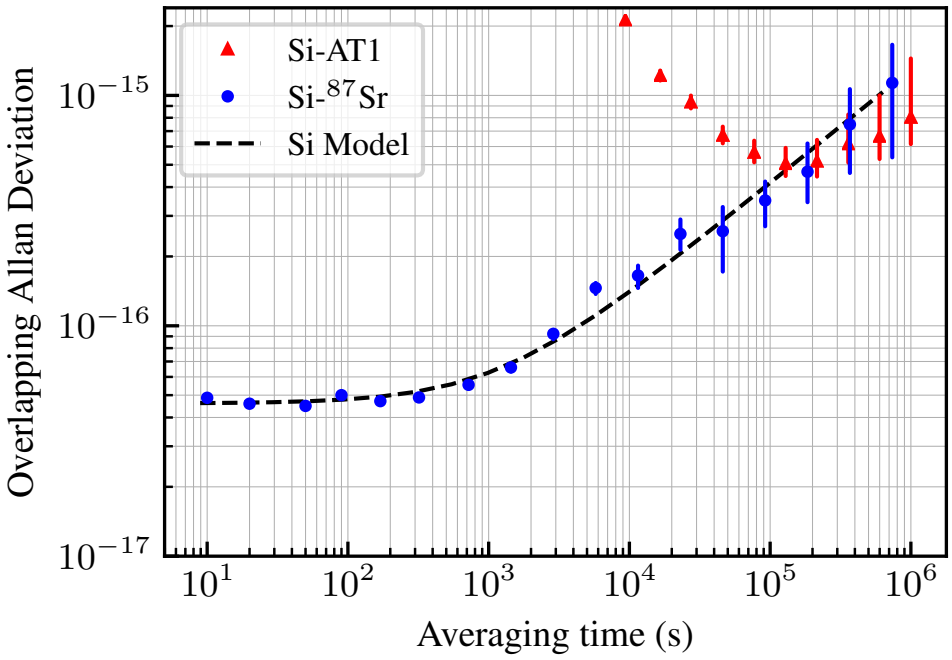

Figure 3.6: Si3 stability. Si3 was compared against Sr1 and NIST's AT1 MASER array. For timescale below 10^5 Sr resolves Si3 instability well below the current timescale. Around 10^5 Si3 stability sufficiently degrades such that it becomes comparable to AT1.

From Sr1 and AT1, the performance of a Si3 based timescale can be modeled and compared to MASER based timescales (see [101] for details). As shown in Figure 3.7, Si3 steered by even 1 hour of Sr1 per day outperforms all MASER based timescales, even with Sr1 steering the MASERs. Importantly, fractional frequency uncertainties below 1×10^{-17} become realizable within 1 year of averaging with an optical timescale. A few additional observations from Figure 3.7 are apparent. Daily interrogation results in a significant bump in the Allan deviation at the day timescale. Considering the nature of the Sr1 machine at the time of this data, obvious gains could come from increased uptime. A dedicated effort to automate relocking of lasers and improve several experimental weaknesses could extend Sr uptime significantly and would be well within the realm of a national lab's expertise. An advantage of Si based timescales would be the ability to instantly improve timescale performance with continued advances in optical clock precision, accuracy, and reliability.

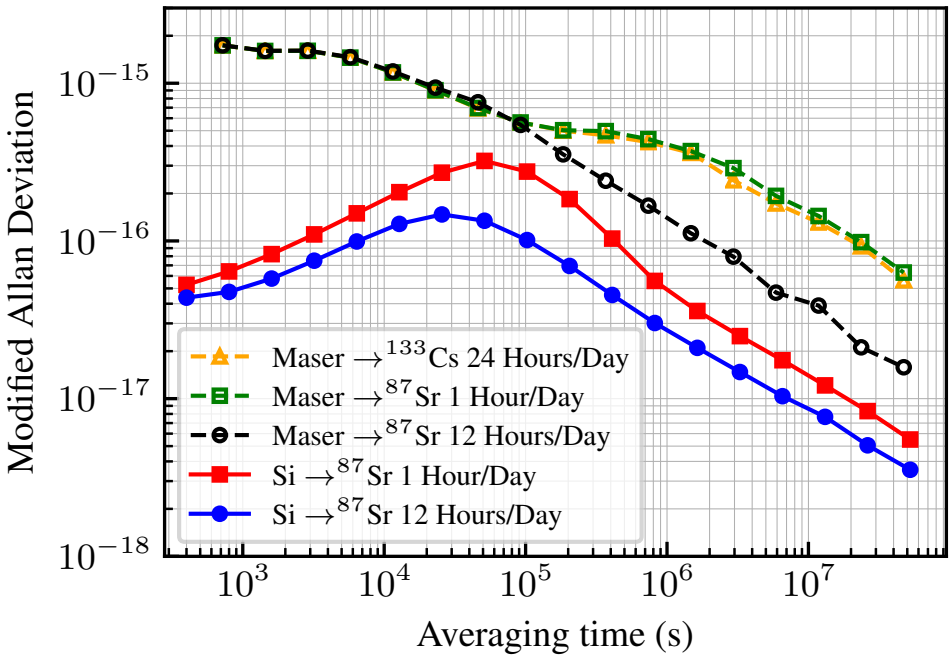

Figure 3.7: Modeled fractional frequency stability of different potential timescales. Si3 steered daily by Sr1, even for one hour, outperforms MASER based timescales. Both Si3 models support fractional frequency uncertainties below 1×10^{-17} at less than one year of averaging.

3.6 Searches For Ultralight Dark Matter

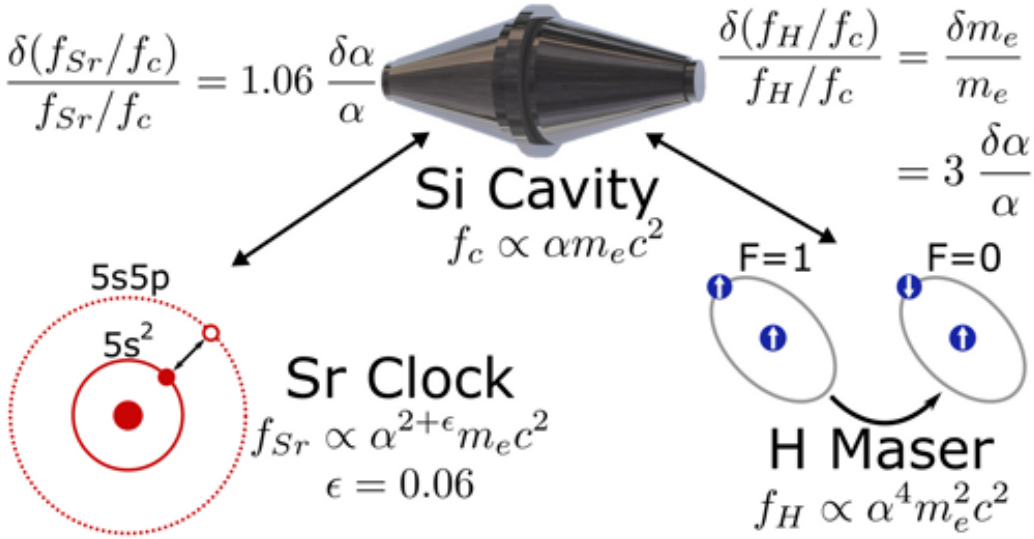

Figure 3.8: Comparison of α sensitivity of the Sr clock transition, Si3 cavity frequency, and H Maser frequency.

The integration of Sr1 into the BACON network provided a unique opportunity to place bounds on the existence of ultralight dark matter owing to varying α sensitivities between Sr1, Si3, and the hydrogen masers at NIST (Figure 3.8). Hypothetically, ultralight dark matter may couple to the fine structure constant α, causing variation in α as a function of time. By performing frequency comparisons of references with energies scaling to different powers of α, oscillations in the frequency record at Compton frequency corresponding to the dark matter candidate mass can be searched for. While our search yielded a result consistent with no detection, it established a further impact of continued development and operation of clock networks.

Chapter 4

The New Sr1 Wannier-Stark Optical Lattice Clock

Let's briefly set the stage for the remainder of this thesis. The last two chapters discussed the original workhorse of Jun's Sr group - the old Sr1 machine. The machine had been used for early MOT studies [151, 87], some of the original absolute frequency measurements of the ^{87}Sr clock transition [31] , demonstrations of SU(N) symmetry [155], and increasingly impressive clock comparisons [90, 16, 112, 38]. Unfortunately the machine was showing its age, from poorly AR coated viewports to challenging magnetic field stabilization issues. Meanwhile clock precision was advancing in the 3D lattice machine (Sr2) and the lab's dream of spin squeezing was growing more vivid (Sr3).

In the spring of 2019 a successful pitch was made by T. Bothwell to separate what was dubbed 'SrE' (spin squeezing, accuracy, near zero deadtime) into a rebuilt Sr1 and new Sr3 project (a dedicated spin-squeezing machine). By rebuilding Sr1 separately, the lab would have a high-uptime, accuracy focused machine. Chapter 3 made clear how vital such a machine is for a large clock group. Let's outline some of the key design goals of a newly rebuilt Sr1.

(1) **High uptime.** A clock that runs robustly and ideally continuously provides a constant reference, be it for a timescale or one of the other 5 Sr projects in JILA. It also accelerates the data taking rate, making both adviser and students happy.

(2) **Improved vacuum lifetime.** The old Sr1 machine had a vacuum lifetime of 8 seconds, limiting interrogation times and increasing the background gas collision systematic.

(3) **Vertical lattice.** Sr1 had run for years with a lattice tilted with respect to gravity at 18°, leading to an inability to operate at < 25 E_{rec} before atoms were lost. This creates problems for Raman scattering and lattice light shifts. Exploration of shallow trap depths was a longstanding goal.

(4) **813 nm build-up cavity inside vacuum.** The retro-reflected lattice setup in Sr1 was a major hindrance to clock operation. Alignment drifts required regular correction, limiting uptime and operational stability. To reduce atomic interactions with a reasonable trap waist, a high power Ti:sapphire laser system was required which regularly broke leading to weeks of unpredictable downtime every year. A build-up cavity enables a solid state diode based lattice system, provides geometrical stability to the system, and supports a significantly larger trap waist for reduction of atomic interactions. To enable reasonable finesse for power enhancement and ensure a pristine wavefront the cavity must be in-vacuum.

(5) **Improved thermal stability.** The original Sr1 had numerous heat sources, from poorly cooled MOT coils to the Zeeman slower. These presented a challenge both in terms of characterizing the BBR environment of the atoms as well as placing demands on environmental control in order to robustly operate the machine. Incorporation of temperature monitoring and stability during construction would be beneficial.

(6) **Increased atom-light interaction times.** There was no physical reason that suggested the 1D architecture should be limited to the 600 ms pulses used for the Sr1/Sr2 comparisons. We had tried longer pulses, but Rabi spectroscopy at the second timescale was unreliable in the Sr1 machine. An important clue however, was the increase in contrast and interrogation times when we switched to larger trap waists for Chapter 2, enabling reduced atomic densities.

To accomplish these goals Sr1 was rebuilt. Let's introduce the new system.

4.1 The New Sr1 System

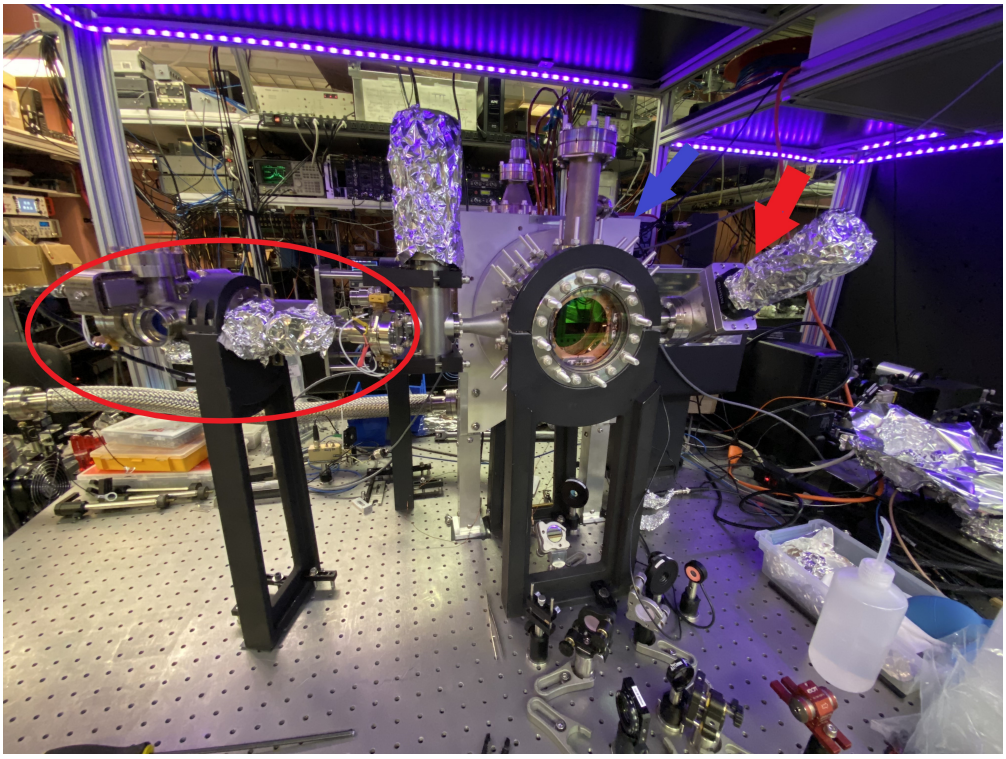

Figure 4.1: Post bake Sr1 system. The system is supported by black anodized aluminum supports. To the left is the AOSense atomic beam system (circled in red) for providing a steady stream of cooled strontium into the MOT. Center is the Kimball Physics 6" Spherical Octagon, with the 6" CF viewport facing the camera. All viewports were mounted using silver coated threaded studs, washers, and nuts for use in mounting important clock hardware. The large white G7 piece (blue arrow) mounted to the raw aluminum legs is the MOT coil that required construction and mounting before baking. Optics on the table were used to check the cavity alignment post bake.

At the heart of the system is the original Sr1 Kimball Physics 6" spherical octagon (Figure 4.1). The chamber is oriented with a pair of 2.75" CF flanges coaxial with gravity and the 6" CF flanges perpendicular. This allows incorporation of the in-vacuum build-up cavity into the groove grabbers on the 2.75" axis and improved imaging and conductance through the 6" CF flanges.

Vacuum quality is significantly improved compared to the previous Sr1 system [95]. Vacuum conductance through a pipe scales as $(\text{diameter})^3$, giving a factor of 10 improvement in the new design by pumping through the 6" versus 2.75" CF flange. The ion pump is upgraded from a 40 L/s to 150 L/s Starcell design for enhanced pumping of noble gases. The addition of two 400 L/s

non-evaporable getters provides pumping for getterable gases (particularly H).

The chamber is supported by milled aluminum pieces (Figure 4.1). The ion pump is supported by a solid block of aluminum. All pieces are coated black to prevent light scattering. Compliance between supports and chamber is ensured through the use of Viton, providing additional dampening.

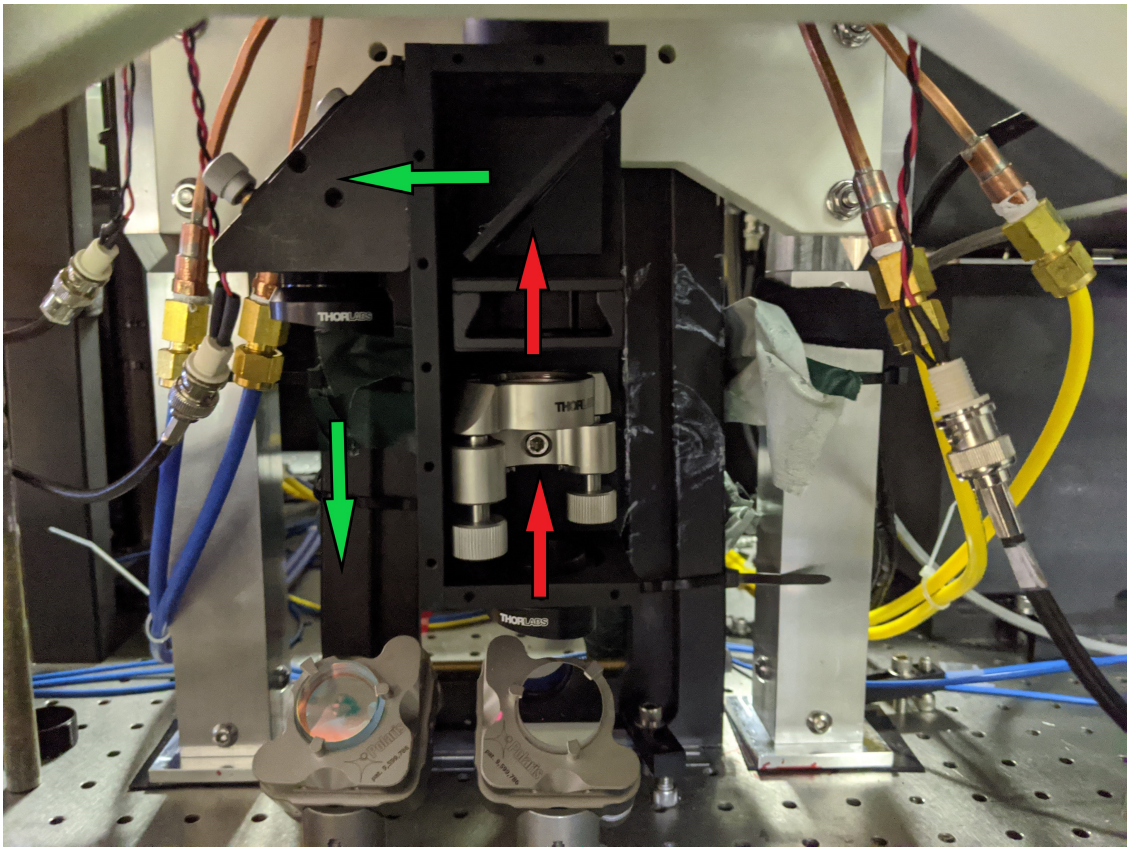

Figure 4.2: Image of clock retro box without cover. The assembly is attached to the threaded rods of the bottom 2 3/4" viewport, ensuring a rigid connection between chamber (lattice retro) and box (clock retro). Lattice light (green arrows) is introduced to the cavity from above, with leakage below used for intensity stabilization. Clock light (red arrows) comes from the table and is partially reflected by a wedged mirror in the Thor Labs mirror mount enabling fiber noise cancellation nearly to the viewport. A slot enables various neutral density filters for clock power attenuation. A high quality dichroic beamsplitter separates lattice light (813 nm) from clock light (698 nm).

Magnetic fields are controlled by the Anti-Helmholtz (AH or MOT) coils and 3 pairs of Helmholtz (bias) coils. A particular nuance in this design is the necessity to build and install the AH coil in the middle of the system before before baking the chamber. The AH coils are built using G7, a commercial composite built of glass fabric and temperature resistant resin, allowing baking

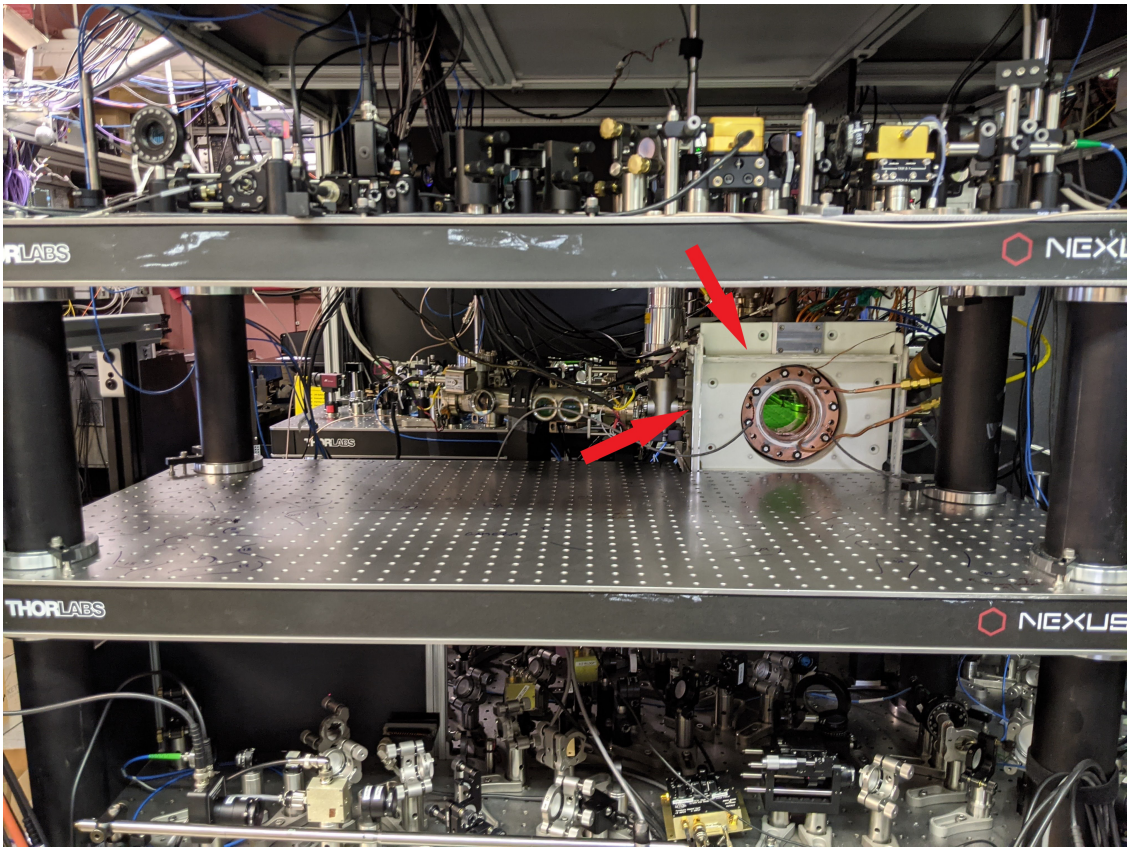

Figure 4.3: Installed mezzanines around the Sr1 chamber. Red arrows show installed bias coils. The copper attachment within the front MOT coil assembly contains the B_x bias coil, with water cooling lines for temperature control. The top mezzanine supports optics for the 813 nm lattice system while cavity transmission optics, clock optics, and MOT optics are on the table.

up to 200° C. The MOT coils are constructed out of hollow core copper tubing with temperature resistant insulation potted in a temperature resistant epoxy. The coils are supported by hollow, square aluminum pieces filled with lead shot. All components of the MOT coil assembly can be baked up to 200° C. After baking, the second MOT coil was installed. The bias coils are mounted to the MOT coil assembly as shown in Figure 4.3. The bias coils were wound in place (using equal lengths of wire to ensure equal numbers of turns) and then potted to provide structural robustness. The B_x bias (axis through the 6" CF flanges of the main chamber) is built into 6" copper pieces used for temperature control of the chamber. More details of temperature control will be specified in the following sections.

A major improvement in the rebuild of Sr1 is the removal of degrees of freedom. Threaded rods were used for the mounting of all viewports, enabling attachment of system pieces directly the chamber (Figures 4.2 and 4.9). This was a valuable lesson learned during the work to modernize the Sr1 system for the clock comparison (Chapter 3) - if it can be adjusted it can drift. Each MOT axis incorporates a temperature control apparatus (itself attached to the threaded rods) threaded using standard Thor Labs SM threads. This enables MOT waveplates, retros, and irises for alignment to be attached to the chamber with excellent precision. Since initial construction and optimization (1.5 years ago), none of these have been touched.

One final improvement in the new system is the use of mezzanines around the chamber for optics (Figure 4.3), eliminating the prevalence of periscopes prone to drift in the previous machine. Each mezzanine is a standard 24"×48" honeycomb breadboard. Legs are black coated aluminum tubing filled with lead shot for vibration dampening [32]. Note - it is important to use non-magnetic steel or aluminum. We found during the studies of Chaper 6 that we had magnetically charged the original Thor Labs breadboard next to the 6" imaging window. Exchange of this breadboard to an aluminum version reduced the background magnetic field gradient across the atomic sample nearly an order of magnitude.

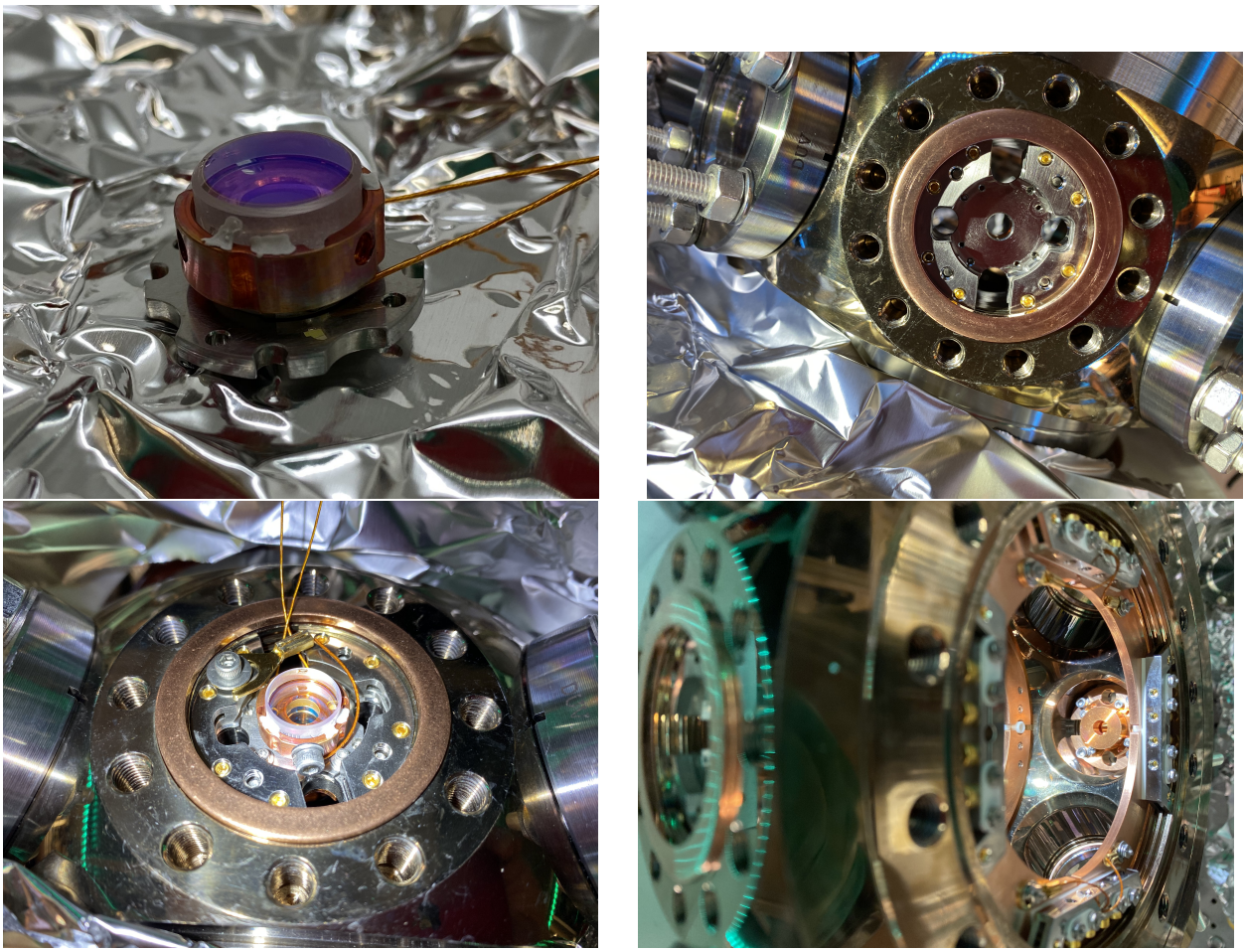

Figure 4.4: Cavity mirror pictures. **Top left:** Top mirror assembly, with bottom stainless steel plate for mounting to groove grabbers, mirror glued to grounded copper piece, and piezo sandwiched between copper and steel. This ensures charges from applied voltages to the piezo do not charge the mirror. **Top right:** Groove grabber cavity mirror support structure inside 2 3/4" CF flange. **Bottom left:** Installed top mirror assembly. **Bottom right:** Picture of Faraday shielding cage between atoms and mirror.

4.1.1 The Build-Up Cavity

At the heart of the new Sr1 system is the in-vacuum build-up cavity for the lattice laser [1] . The basic design criteria are:

(1) **Vertical mounting.** We want the lattice to be parallel to gravity, enabling the lowest operational trap depth possible without atom loss. This is critical for reduction of both Raman scattering and lattice light shifts.

(2) **High quality 698 nm AR coating.** We need quality clock spectroscopy, meaning no significant standing wave at 698 nm.

(3) **Large build-up factor.** For lattice light shift evaluations trap depth operation over 500 E_r is desirable. Commercial diodes offer around 500 mW of power at 813 nm and would be a far more robust solution for the optical lattice than a commercial Ti:sapphire system (and much cheaper!). Finally a large build-up factor would enable a larger trapping waist.

(4) **A large waist.** The previous sytem used a 80 micron waist. Increasing this by a factor of three would increase trapping volume by nearly a factor of 10, reducing the density shift systematic significantly. Furthermore, a large waist corresponds to a large Rayleigh range, which when combined with a modest finesse (near 1000) ensures homogeneous lattice trapping conditions throughout the atomic sample.

(5) **Faraday shielding.** Patch charges may build up on the cavity mirrors, and the piezo for cavity stabilization may provide additional fields [85]. The atoms require shielding from these electric field sources to avoid deleterious DC Stark shifts.

To address (1) the cavity mirrors are mounted using Kimball Physics groove grabbers in the 2 3/4" CF flanges oriented along gravity (Figure 4.4). By using the precisely machined, one-piece

[1] Special shout-out to John Robinson and Eric Oelker. The robust, well designed in-vacuum build-up cavity is the heart of the new Sr1 system and would not be the same without their cavity expertise. John led the design, in-vacuum construction, and initial testing. Eric put together the locking infrastructure and careful mode-matching solution. John's original notes are the starting motivation for this section.

vacuum chamber as the cavity spacer we gain a robust, stable lattice that forms the physical basis for our experiments.

Mounting the cavity within the groove grabbers set the spacing between mirrors to ~ 15 cm. The waist for a symmetric resonator in vacuum is given by [105]

$$\omega_0^2 = \frac{\lambda}{\pi}\sqrt{\frac{dR}{2} - \frac{d^2}{2}} \tag{4.1}$$

where λ is the cavity wavelength, d the cavity length, and R the radius of curvature of the mirrors. For standard mirrors and our dimensions we settled on $R = 1$ m, giving $\omega_0 \approx 260$ micron, a 3x increase compared to the lattice from Chapter 2. This corresponds to a Rayleigh range of $z_r = 26$ cm. **Measurements of the free spectral range of the cavity ($\nu_{FSR} = c/2d$) performed after completion gave a cavity length of $d = 16.9$ cm, corresponding to a waist of 262 μm.**

To ensure sufficient power enhancement of the cavity for deep trap depths while using a diode laser system, an over-coupled design was chosen. The power enhancement factor is given by [128]

$$\frac{I_{circ}}{I_{inc}} \approx \frac{4\delta_1}{(\delta_1 + \delta_2)^2} \tag{4.2}$$

where $\delta_i = \ln(1/R_i)$ with R_i being the reflectivity of mirror i. Equation 4.2 assumes ideal mirrors with no loss besides transmission. The corresponding finesse for the coefficient of reflection $r_i = \sqrt{R_i}$ is given by [105]

$$F = \frac{\pi\sqrt{r_1 r_2}}{1 - r_1 r_2}. \tag{4.3}$$

np.

To optimize power buildup while ensuring sufficient transmission through the low loss mirror for intensity control mirrors were chosen to have a transmission of $T_1 = 1 - R_1 = 6000$ ppm and $T_2 = 1 - R_2 = 100$ ppm, corresponding to $B = 643$ and $F = 1027$.

4.1.1.1 Finesse Measurement

To measure the finesse of the cavity recall that the average time light remains inside the cavity is given by $t_0 = 2\pi c/dF$ where c is the speed of light, d the standing wave resonator length, and F the finesse. For reasonably high finesse, t_0 is found by quickly turning off the light incident on the cavity and measuring the exponential decay of transmitted power P as a function of time t, as given by [105]

$$P(t) = P_0 e^{-t/t_0} = P_0 e^{-(2\pi c/dF)t}. \tag{4.4}$$

The results of a post-bakeout finesse measurement are shown in Figure 4.5. The finesse was found to be $F = 1020(60)$, with the uncertainty due to the pulling of the fit based on initial cuts of data points. The associated decay time constant (Figure 4.5) is quite fast for an AOM, requiring exclusion of datapoints at the onset of extinction of the ingoing cavity light. The results are consistent with the designed mirror specifications previously listed.

4.1.1.2 Birefringence Measurement

For rejection and/or control of differential AC Stark shifts to the ground and excited clock state (lattice light shifts) it is usually ideal to operate with linear polarization for the lattice light. Circular polarization introduces several complications, most notably by altering the tensor shift of the lattice. A small mixture of non-circular polarization acts a fictitious magnetic field, changing the alignment of lattice polarization relative to the quantization axis set by a bias field. This perturbation is given by [127]

$$\Delta\nu_{vt} = -\gamma_{vt}|\vec{\epsilon}\cdot\vec{\epsilon_B}|^2\xi\cos\theta U_0^2. \tag{4.5}$$

Here $\gamma_{vt} = 11\ \mu\text{Hz/E}_r^2$ for a 1 G field. $\vec{\epsilon}$ describes the lattice polarization and $\vec{\epsilon_B}$ the unit vector of the bias field. θ describes the angle between the lattice light wavevector and bias field and U_0 the trap depth. ξ is the ellipticity of the lattice light.

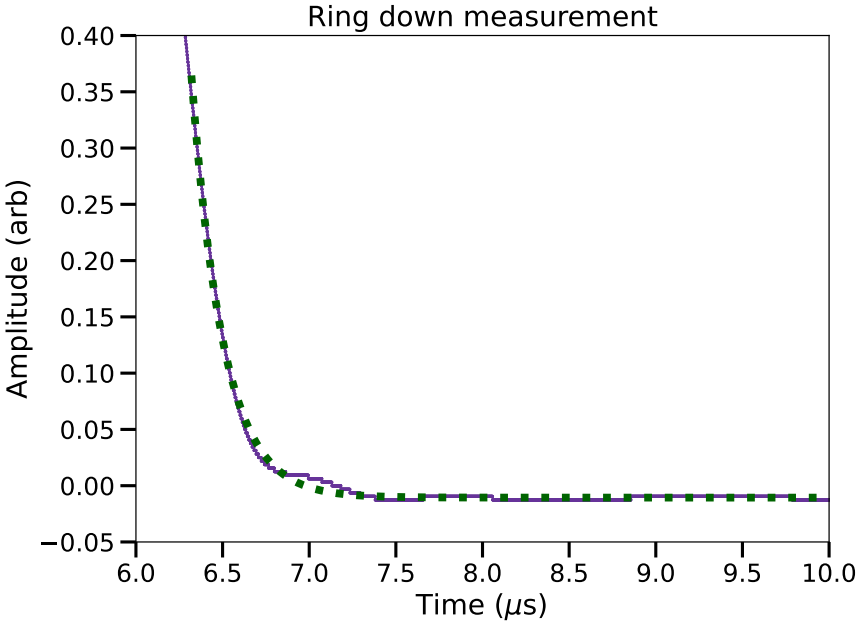

Figure 4.5: Cavity ring-down measurement. Transmitted intensity through the cavity is measured on a PD. The light is extinguished by an acousto-optic modulator (AOM) and the decaying exponential fit, finding a decay time constant of 183 ns. From this decay and measured cavity length a finesse of $F = 1020(60)$ is found, with the large uncertainty arising from the sensitivity of the fit to the number of data points cut before fitting.

Equation 4.5 tells us that we have a scaling with U_0^2, the same as the hyperpolarizability coefficient. We would therefore like to make sure that our ellipticity 1) is such that evaluations of the hyperpolarizability coefficient will not be polluted and 2) provides no meaningful contribution on our path towards accuracy at the 19th digit.

The ellipticity parameter is given by

$$\xi = \sqrt{\frac{P_{min}}{P_{max}}} \tag{4.6}$$

where P_{min} (P_{max}) is the minimum (maximum) power transmitted through a rotated polarizer after the optic in question. To ensure pure polarization before entering the cavity (including viewports), a polarizer was placed before the chamber. A polarizer placed on the opposite side was rotated 360° to probe the transmitted light, noting the minimum and maximum power through the polarizer. the measurement was repeated a second time after rotating the initial clean-up polarizer 45° to bound

a worst-case ellipticity should the cavity be probed off the eigen-axis of birefringence. We bounded the extinction ratio to 3.2×10^{-5} ($\xi = 5.7 \times 10^{-3}$), likely limited by the achievable extinction ratios of the given polarizers.

For our system, even with applied fields as small as 200 mG, we anticipate $\Delta\nu_{vt}$ contributing at $< 1/100$ of the level of hyperpolarizability.

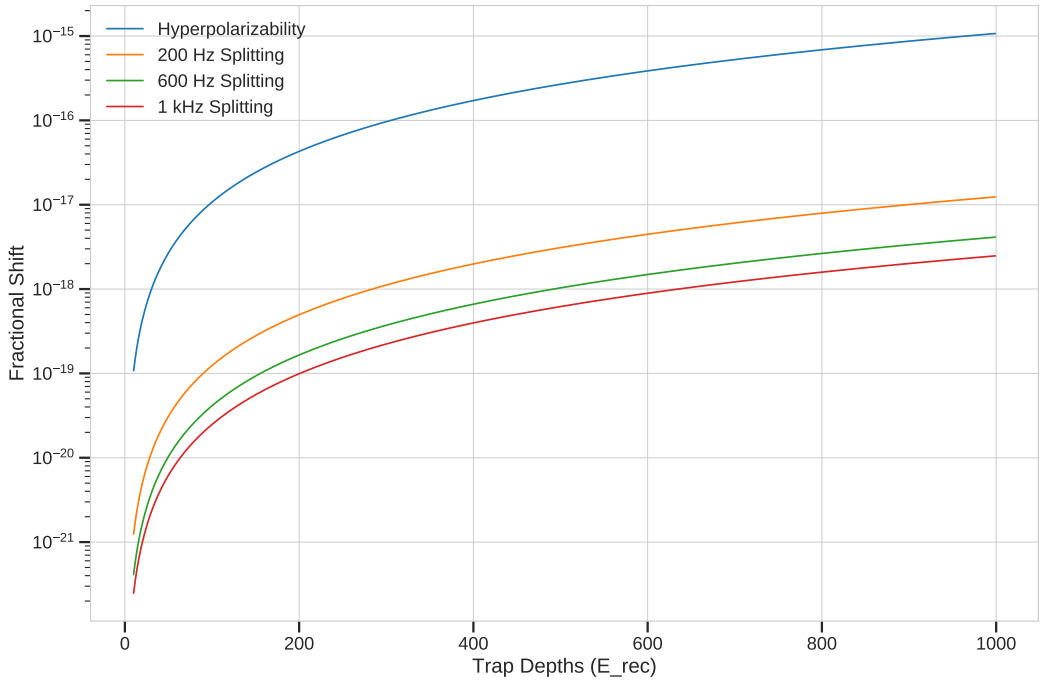

Figure 4.6: Comparison of hyperpolarizability and birefringence induced flock shifts as a function of trap depth as bounded by worst case ellipticity. Results are reported for $m_F = \pm 9/2$.

4.1.2 DC Stark Plates

In the early days of Sr OLC research, SYRTE was a major proponent of in-vacuum build-up cavities [29]. Unfortunately they found large DC Stark induced systematic shifts (10^{-13} level), hindering accuracy and requiring extensive work to cancel [85]. Care must be taken when attempting to cancel a DC electric field across an atomic sample as the DC Stark shift is quadratic (Chapter 2),

meaning a global measurement of the DC Stark shift (and elimination) may still be contaminated by a gradient, resulting in a residual shift.

Figure 4.7: DC Stark plate construction. **Top left:** Example of a quadrant plate split in half, showing groove grabber assembly for both assembling all four quadrants together and mounting to the chamber. Note the use of alumina to electrically isolate each quadrant. **Top right, bottom left:** Picture of the plates installed into the Kimball Physics chamber, showing wiring. **Bottom right:** Assembly for routing quadrant plate wires around 2 3/4" CF port.

To avoid the above issues, it is always best to begin with as close to zero DC Stark shift as possible. From the previous Sr1 machine we know that viewports don't spontaneously develop patch charges - one must polarize them. To avoid patch charges from the cavity and residual fields from the cavity piezo, the atoms are shielded from each mirror assembly by a grounded copper Faraday shield. The shield of copper is 5 mm thick with an ID of 6 mm, matching the piezo ID. COMSOL simulations showed that the design would provide sufficient attenuation of any reasonable

patch charges and fields from the piezo.

In the previous machine, quadrant plates for applying an electric field across the atoms enabled probing and elimination of DC Stark shifts in all three spatial dimensions. A constant worry was the the issue of developing charges around the chamber from application of large electric fields near dielectrics (we did temporarily create a background field but it dissipated quickly [25]). To avoid this issue in the previous machine the applied fields were regularly switched during the sequence (atom preparation period), enabling a nearly zero time average for the applied field. In the new machine we incorporated bias plates inside the vacuum chamber. By reducing the distance between the plates we readily increase the strength of applied field. By building the plates in vacuum, worries about charging dielectrics is removed.

The DC Stark bias plates in the new system are shown in Figure 4.7. They are built into the 6" CF flange groove grabbers of the Kimball Physics chamber, with each side having an assembly of 4 copper plates. They are electrically isolated from each other by the use of alumina spacers. Each plate has a separate electrical connection out of the chamber, allowing each quadrant to be controlled separately. The wires pass though a grounded braid to eliminate bias fields from the wires themselves.

For initial DC Stark evaluations we applied voltages of ± 80 V to the X, Y, and Z directions. Recall X is the axis of the 6" CF flanges and Z the axis of the cavity. Figure 4.8 shows the results for X, with no statistically meaningful field found at the 2×10^{-19} level. Y and Z additionally showed no statistically meaningful field found at the 2×10^{-19} level. After installation of imaging, DC Stark gradients were also not found at any meaningful level for accuracy purposes (Chapter 6).

4.1.3 Temperature Control

Extensive temperature control of the new system was installed during construction, eliminating the need for painful installation of a thermistor array after the full rebuild. Baseline thermal control is ensured by utilizing temperature controlled air pulled through a HEPA filter unit onto both the chamber and laser side of the table (portioned for light control and independent temper-

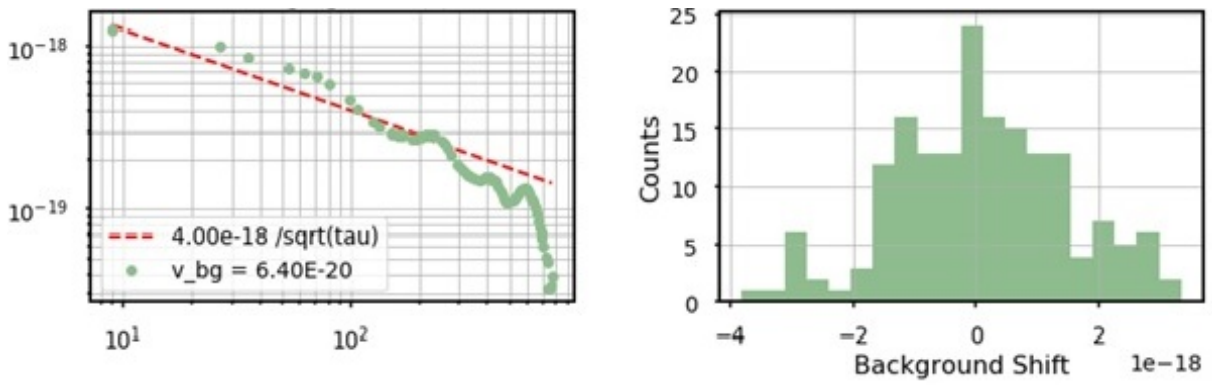

Figure 4.8: DC Stark evaluation along X. On the left is the Allan deviation of the evaluated background shift for voltages biases of ±80 V applied to each plate (160 V difference). A background shift of $6(23) \times 10^{-20}$ was found, consistent with zero. The right plot shows a histogram of background shifts.

ature control), as in Chapter 2. MOT coil temperatures are controlled by a powerful recirculating chiller, itself water chilled ensuring removal of heat from the lab. Each MOT coil, while electrically connected, is split into two in regards to water connections allowing significantly improved cooling compared to the previous Sr1 design. The blue MOT is additionally operated with <1/2 of the gradient of the previous machine, further reducing the heatload.

50 mK interchangeable thermistors (PR503J2) for monitoring the chamber and air temperatures were mounted after baking using thermally conductive epoxy. Building on the lesson of Chapter 2, each viewport has a dedicated temperature control apparatus installed, providing both temperature control and an insulating air pocket over the airport for improved homogeneity (Figure 4.9). The pieces are constructed of copper to provide maximum thermal homogeneity to minimize any temperature gradients.

A major improvement to the new machine is the elimination of heatloads present in the previous design. The AOSense atomic beam system uses permanent magnets, eliminating current controlled bias coils - a large negative of the previous machines Zeeman slower design. The AOSense system furthermore steers the atomic beam around a corner, eliminating line of sight between heated Zeeman window and atoms. The camera used for imaging is water cooled. The summation of these improvements and controls is a stable, robust system. Alignment is robust over the timescale of

Figure 4.9: Temperature control/optics mounting pieces for the 2 3/4" CF flanges (viewports). **Top left:** The main control piece is a copper cylinder wrapped with hollow copper tubing soldered in place. The tubing allows temperature controlled water to flow around the piece, stabilizing the temperature. Holes for mounting to the chamber (**bottom left**), top piece installation (**top right**), and thermistor installation are included. **Bottom right:** An installed assembly including Thor Labs SM2 lens tube for mounting of MOT optics is shown. Jack screws enable fine alignment of the retros but are not needed thanks to the Kimball Physics chamber and careful machining of copper pieces. A thin layer of high thermal-conductivity paste is used between the piece shown in the **top left** and the vacuum chamber, ensuring good thermal conduct and compliance for any slight imperfections.

many months, radically reducing the maintenance required in the previous version. Examples of the temperature control stability on the chamber (viewports) are shown in Figure 4.10 (4.11).

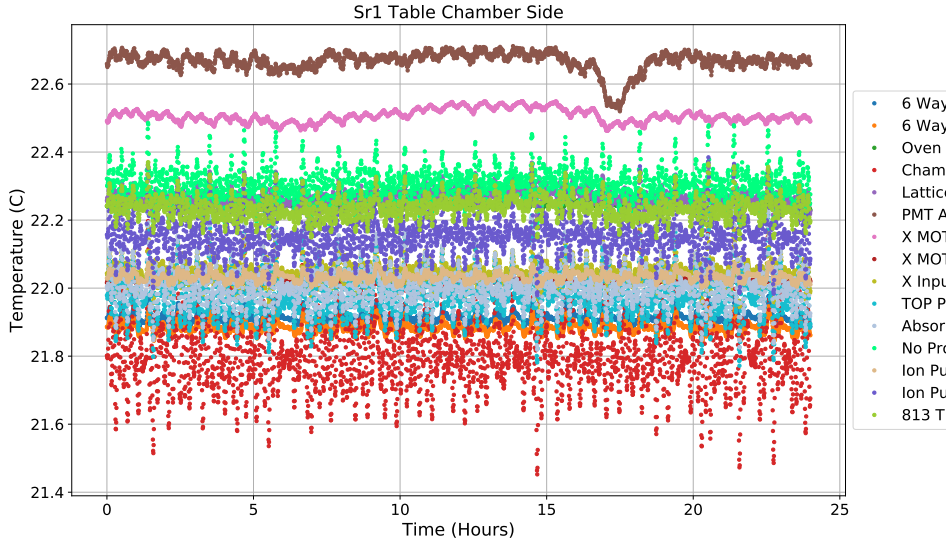

Figure 4.10: Chamber temperatures from 8/14/21. Monitoring thermistors are mounted to the chamber.

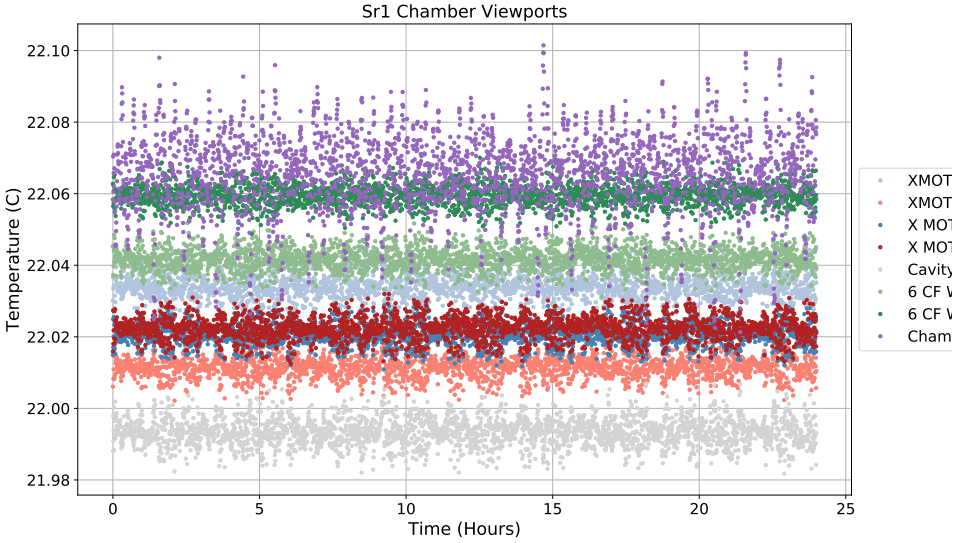

Figure 4.11: Viewport temperature from 8/14/21. Each sensor is attached to a copper control piece mounted to the respective viewport.

4.1.4 Expansion Port

Figure 4.1 shows the expansion port present on the Sr1 system. An MDC gate valve was installed for use in the next accuracy evaluation (10^{-19} level). The plan is to add a custom chamber for installation of an in-situ thermometer for probing the temperature (BBR) at the atoms. A 30 cm linear push-pull device will be used to insert/retract the probe. The expansion chamber will include additional pumping (25 L/s ion pump and 50 L/s NEG) as well as a residual gas analyzer to document the composition of the vacuum chamber gas load for the background gas systematic.

4.2 Experimental Operation

The Sr1 system largely follows the operation described in [21, 88, 95, 25].

Standard blue MOT operation proceeds for $\sim$ 100 ms, though at a lower gradient ($\sim$ 20 G/cm) compared to the old machine (50 G/cm). At the end of the blue MOT sequence the MOT gradient is ramped to $\sim$ 6 G/cm over 10 ms and the blue intensity is reduced, leading to a colder, less compressed blue MOT. The magnetic gradient is then set to $\sim$ 3 G/cm for the broadband (BB) and single frequency (SF) red MOT operation. With atoms $< 10\ \mu K$ loaded into the 300 E_r optical lattice an additional cooling stage is performed. Atoms are simultaneously nuclear spin polarized, doppler cooled ($< 1\mu K$, Figure 4.12), and axially cooled ($n_z \approx 0$, Figure 4.13). This is enabled by reducing the intensity of the cooling light provided by the 9/2 to 11/2 cooling laser by $> 10,000$.

After cooling, the lattice is adiabatically ramped to the operational trap depth. Depending on the experiment, a series of rapid clock laser pulses is used to change the nuclear spin state of the polarized sample. Standard clock spectroscopy [21, 88] proceeds, after which the lattice is ramped back to 300 E_r and the excitation fraction is readout by fluorescence spectroscopy. Imaging photons are collected on both a standard PMT for center of mass clock locking as well as an Andor iXon camera for in-situ imaging [93].

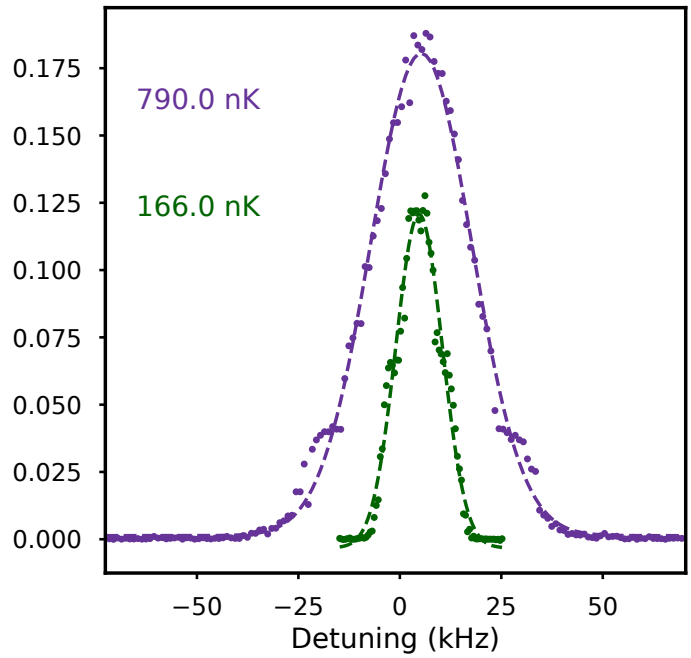

Figure 4.12: Doppler scans after initial loading and cooling at 300 E_r (purple curve) and after ramping to an operational trap depth (15 E_r shown in green).

4.3 Imaging

Standard fluorescence imaging is used in the system. The calibrated camera pixel size (including imaging system) is evaluated to be 6 micron based on free-fall time of flight measurements [25].

Important for in-situ imaging is the consistent scattering rate of imaging photons across the atomic sample. In the Sr1 system, the density shift systematic leads to inconsistent scattering rates creating erroneous frequency shift corrections. To avoid this, we shape the probe beam to have an aspect ratio of nearly 3 to 1, with the long axis matched to the millimeter atomic sample (Chapter 6). The scattering rate throughout the atomic sample is consistent at the 1% level (Figure 4.14).

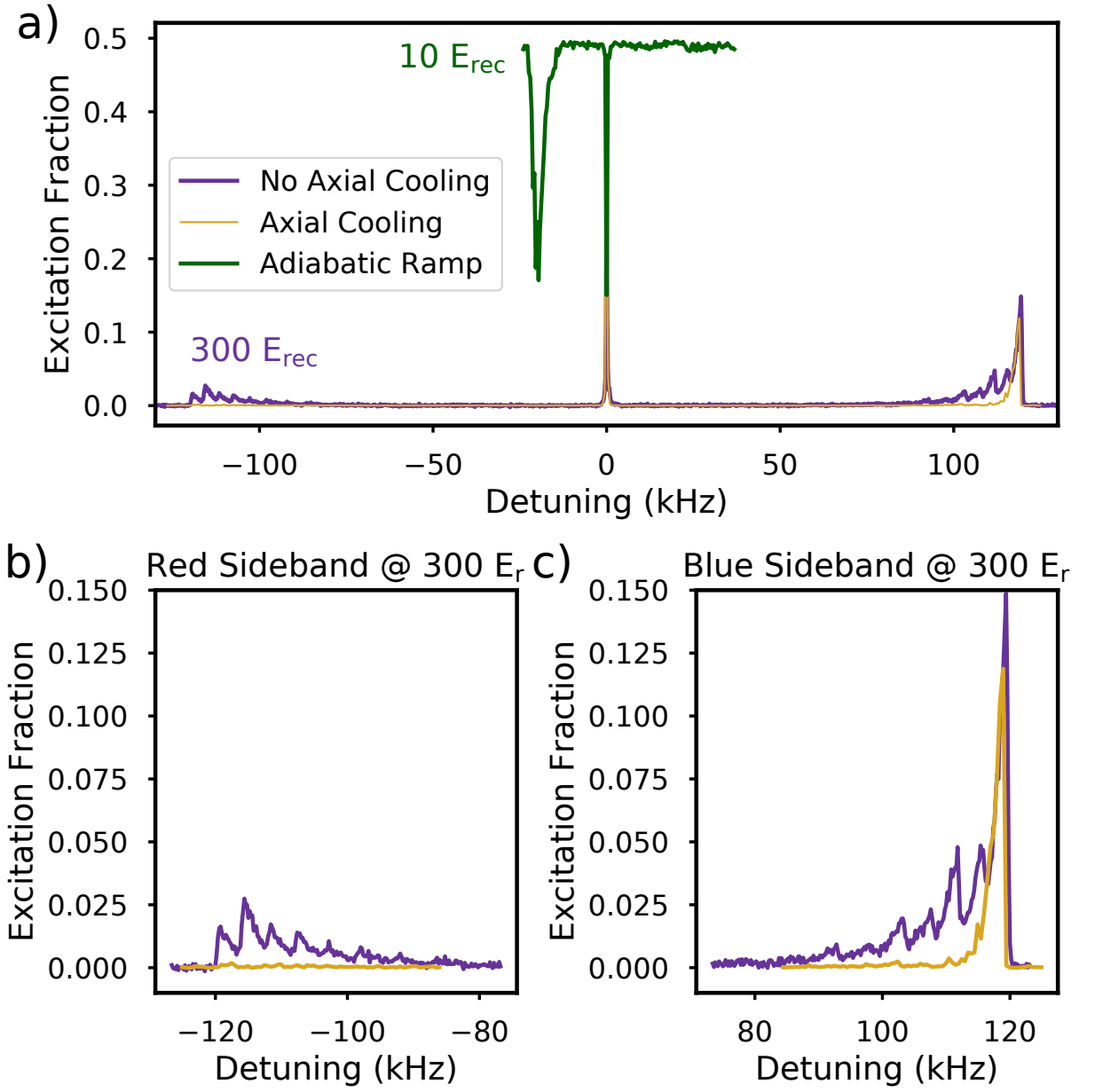

Figure 4.13: Axial clock scans. **a)** Axial scans at 300 E_r and after adiabatically ramping to 10 E_r with atoms prepared in the excited clock state. The green line has been offset by 0.5 from an excitation fraction of 1.0 for plotting. Note the near absence of red sideband indicating $n_z \approx 0$. Additionally note the spiky structure within the sideband structure - these correspond to spectroscopy of varying n_z states in the purple curve, now resolved thanks to the < 1 μK radial temperatures at 300 E_r. **b)** Enhanced view of the red sideband. **c)** Enhanced view of the blue sideband.

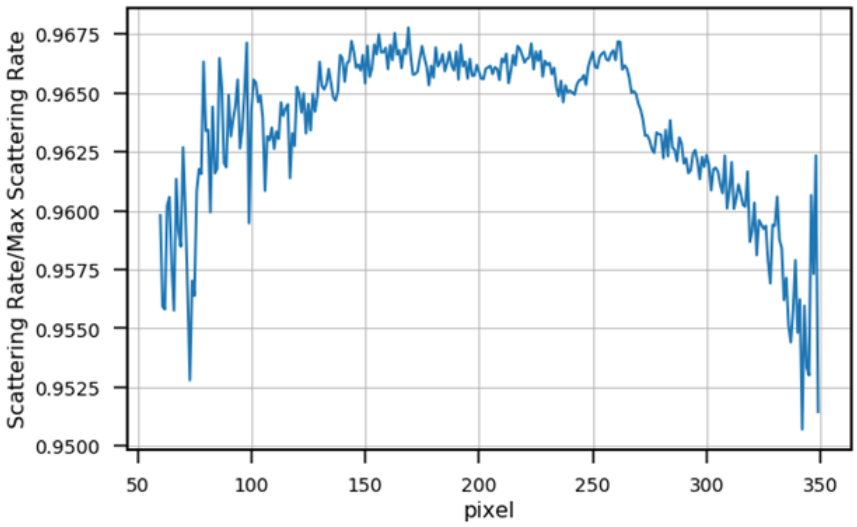

Figure 4.14: Calibration of fluorescence probe scattering rate throughout the atomic sample. To evaluate the scattering rate per pixel, a series of atom pictures is taking with varying probe power, allowing calculation of the saturation parameter (ratio of intensity to saturation intensity), and therefore maximum scattering rate.

4.4 Vacuum Lifetime

The vacuum lifetime leads to an atom loss mechanism, potentially increasing QPN at long interrogation times through reduction of maximum atom number. Background gas collisions also lead to a systematic shift of the clock frequency.

Evaluation of the vacuum lifetime is readily performed by lifetime measurements of $^3P_2$ atoms trapped in the AH magnetic field. Loading a blue MOT without repumps over the course of several seconds loads a significant population into magnetically trapped $^3P_2$ states. With a magnetically trapped population, the lasers may be extinguished for a varied period of time. After holding, the atoms are repumped and the population is measured via fluorescence. The atomic population (N) as a function of hold time is then fit to the following equation

$$N(t) = N_0 \exp(-t \times (1/\tau + 1/\tau_{BBR})) + C, \tag{4.7}$$

where N_0 is the initial population, t is the varied hold time, τ the vacuum lifetime, and C an

offset. $\tau_{BBR} = 104$ s is the lifetime of the $^3P_2$ state at room temperature [152]. Figure 4.15 shows the vacuum lifetime as evaluated at a variety of oven temperatures of the AOSense oven. It was found that as the oven pressure was increased the vacuum pressured degraded. We find for an oven temperature of 375° $\tau = 27$ s, just shy of a factor of four improvement compared to the previous system despite the addition of significant in-vacuum hardware.

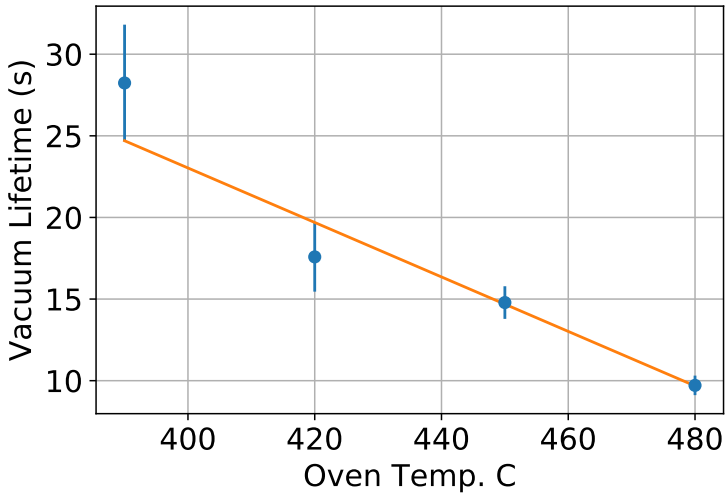

Figure 4.15: Vacuum lifetime versus oven temperature. The trend is well reproduced by a linear fit of slope -0.167 s/°C and offset of 89.8 s at 0°C.

Chapter 5

Wannier-Stark States, a Spin Model, and the 'Magic Depth'

The study of atomic interactions within optical lattice clocks has a rich history, with dedicated experimental and theory collaboration critical for developing the spin model characterizing the interactions [94, 95, 118]. The ability to understand the atomic interactions in our system using the spin model has not only benefited clock evaluations, but enabled studies of SU(N) symmetry [155] and synthetic gauge fields [76, 26].

In this chapter we explore atomic interactions in a Wannier-Stark (WS) ladder [143]. We begin by reviewing the calculation of the WS wavefunctions, illuminating the origin of a new s-wave interaction in the clock. We briefly connect this work with our earlier spin-orbit coupling (SOC) studies, emphasizing the power of analyzing our system utilizing the tools of solid state physics [81, 67]. With then turn our attention to the spin model, qualitatively discussing the effect of atomic interactions on Rabi spectroscopy. With this understanding we finally discuss the 'magic depth' operation in the Sr1 system [1], demonstrating an operational regime where precision and accuracy are combined as demonstrated by Chapter 6.

5.1 Bloch, Wannier, and Wannier-Stark Wavefunctions

The physics of independent electrons moving in a lattice is well known [3, 49], providing an excellent basis for the study of atoms in an optical lattice. We begin with the Hamiltonian for a

single particle in a periodic potential, given by

$$H = \frac{\vec{p}^{\,2}}{2m} + V(\vec{r}) \tag{5.1}$$

where $\vec{p}$ is the momentum operator, m the particle's mass, V the potential, and $\vec{r}$ the position operator. Consider the case of a constant potential. In this situation H is invariant under any translation. As $\vec{p}$ is the generator of translation, this means

$$[H, \vec{p}\,] = 0, \tag{5.2}$$

and thus eigenstates of $\vec{p}$ (plane waves) are eigenstates of H. Now instead consider a periodic potential

$$V(\vec{r} + \vec{a}\,) = V(\vec{r}), \tag{5.3}$$

where $\vec{a}$ corresponds to a primitive lattice vector (in the 1D Sr clock, $\lambda/2$). The Hamiltonian is now only invariant under translation by a primitive lattice vector ($T_{\vec{a}_j}$). Bloch's theorem [49] tells us that the general solution to Equation 5.1 with a potential of the form of Equation 5.3 is given by

$$\psi_{\vec{q}}\,(\vec{r}) = e^{i\vec{q}\cdot\vec{r}/\hbar} u_{\vec{q}}(\vec{r}) \tag{5.4}$$

where $\vec{q}$ is crystal (lattice) quasimomentum, being a good quantum number for the Hamiltonian under study. Note the solid state literature typically uses crystal momentum $\vec{k} = \vec{q}/\hbar$, but here we use $\vec{q}$ to both be consistent with the ultracold community and avoid additional use of the letter 'k'. The translational symmetry of the potential is carried by $u_{\vec{q}}(\vec{r})$:

$$u_{\vec{q}}(\vec{r} + \vec{a}_j) = u_{\vec{q}}(\vec{r}). \tag{5.5}$$

To proceed, consider the result of the momentum operator applied to Equation 5.4:

$$\vec{p}\psi_{\vec{q}}(\vec{r}) = e^{i\vec{q}\cdot\vec{r}/\hbar}(\vec{q}+\vec{p})u_{\vec{q}}(\vec{r}). \tag{5.6}$$

We may then find the modified Schrodinger equation to be

$$\begin{aligned} H_{\vec{q}}u_{n\vec{q}} &= \left[\frac{1}{2m}(\vec{p}+\vec{q})^2 + V(\vec{r})\right]u_{n\vec{q}} \\ &= E_{n\vec{q}}\; u_{n\vec{q}} \end{aligned} \tag{5.7}$$

where $E_{n\vec{q}}$ is the eigen-energy and n is the so called 'band index' arising from restricting our solutions to the first Brillouin zone [49].

Let us now consider the 1D problem, denoting 1D position z, anticipating connection to our 1D optical lattice. Thanks to the Bloch theorem both our optical potential and functions $u_{n\vec{q}}$ have the same periodicity, allowing us to write both as a discrete Fourier sum [54]:

$$V(z) = \sum_b V_b e^{i2bkz} \quad \text{and} \quad u_{n,\vec{q}} = \sum_l c_l^{(n,q)} e^{i2lkz}. \tag{5.8}$$

It follows that

$$\begin{aligned} V(z)u_{n\vec{q}} &= \sum_b \sum_l V_b e^{i2(b+l)kz} c_l^{n,q} \\ &= -V_0 \sum_l c_l^{n,q}\left(e^{i2(l+1)kz} + e^{i2(l-1)kz}\right) \end{aligned} \tag{5.9}$$

where we exploit the expansion of the potential,

$$\begin{aligned} V(z) &= -V_0\cos(kz)^2 \\ &= -\frac{1}{4}V_0\left(e^{2ikz} + e^{-2ikz} + 2\right). \end{aligned} \tag{5.10}$$

Similarly, we expand the kinetic energy term,

$$\begin{aligned}\frac{1}{2m}(p+q)^2 u_{n\vec{q}} &= \frac{1}{2m}\sum_l (p+q)^2 e^{2ilkz} c_l^{(n,q)} \\ &= \frac{1}{2m}\sum_l (2\hbar kl+q)^2 e^{2ilkz} c_l^{(n,q)}.\end{aligned} \tag{5.11}$$

With these in hand, we may finally rewrite Equation 5.7 as

$$\sum_l \left[\frac{(\hbar k)^2}{2m}\left(2l+\frac{q}{\hbar k}\right)^2 c_l^{(n,q)} - \frac{V_0}{4}[c_{l-1}^{(n,q)} + c_{l+1}^{(n,q)}] - E_n c_l^{(n+q)}\right] e^{2iklz} = 0. \tag{5.12}$$

Equation 5.12 may be written as an infinite square matrix of dimension $l \times l$, though for calculations l is typically truncated to around 20 lattice sites. The truncated, tridiagonal matrix is of the form [54]:

$$\sum_l H_{l,l'} \cdot c_l^{(n,q)} = E_q^n c_l^{(n,q)} \quad \text{and} \quad H_{l,l'} = \begin{cases} (2l+q/\hbar k)^2 E_{rec} & \text{if } l = l' \\ -V_0/4 & \text{if } |l-l'| = 1 \\ 0 & \text{else.} \end{cases} \tag{5.13}$$

For 5 lattice sites the Hamiltonian matrix takes the form

$$\begin{pmatrix} (-4+q/\hbar k)^2 & \frac{-V_0}{4} & 0 & 0 & 0 \\ \frac{-V_0}{4} & (-2+q/\hbar k)^2 & \frac{-V_0}{4} & 0 & 0 \\ 0 & \frac{-V_0}{4} & (q/\hbar k)^2 & \frac{-V_0}{4} & 0 \\ 0 & 0 & \frac{-V_0}{4} & (2+q/\hbar k)^2 & \frac{-V_0}{4} \\ 0 & 0 & 0 & \frac{-V_0}{4} & (4+q/\hbar k)^2 \end{pmatrix}.$$

which when diagonalized gives the eigenergies and Fourier coefficients $c_l^{(n,q)}$. The corresponding Bloch states can then be readily found using the evaluated coefficients and Equation 5.8. Solving for the eigenergies of different bands allows calculation of the tunneling rate (J) as the width of each band corresponds to $4J$. Energy solutions and Bloch wavefunctions are shown in Figures 5.1 and 5.2, respectively.

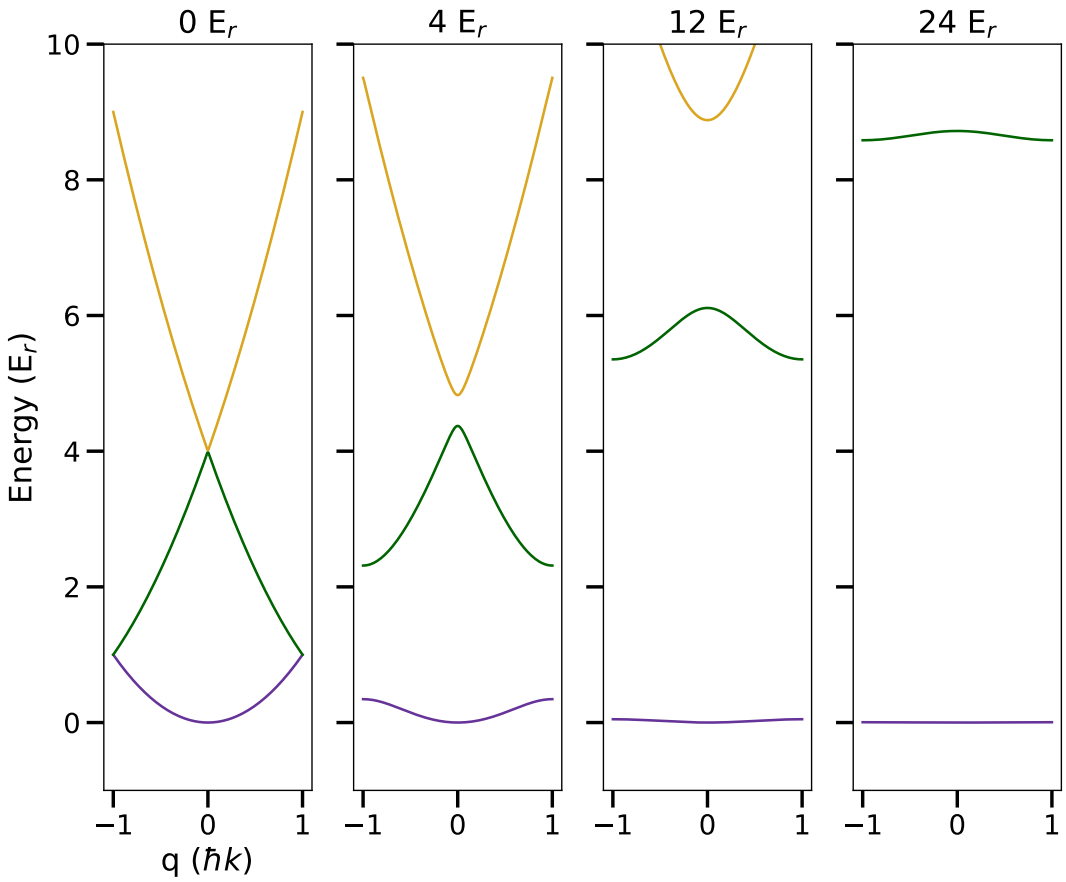

Figure 5.1: Bloch band structures of optical lattices for varying trap depths. Each plot shows energy versus quasimomentum for the first Brillouin zone. Purple, green, and yellow correspond to the ground, first, and second bands respectively. Note the decreasing bandwidth as trap depth increases, corresponding to decreased tunneling energy.

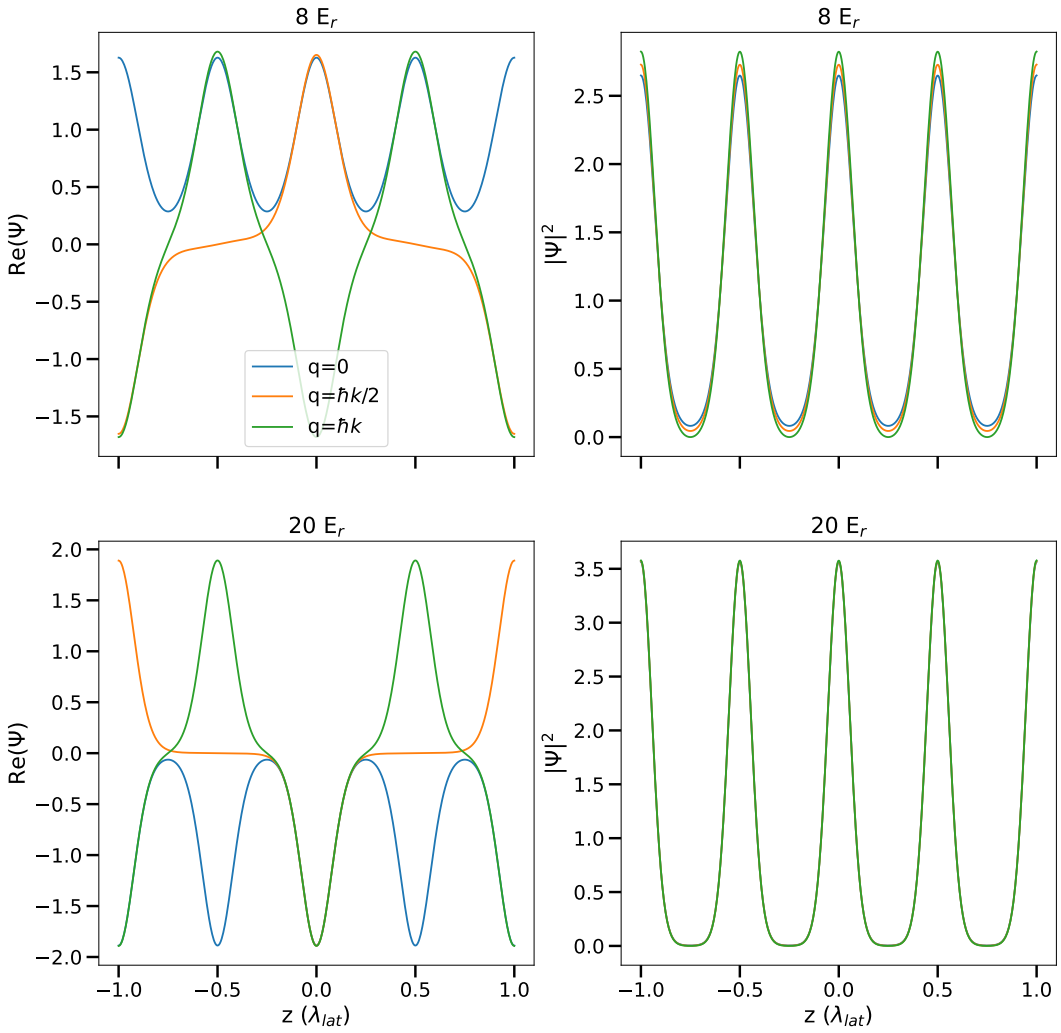

Figure 5.2: Wavefunctions (ψ) and probability densities ($|\psi|^2$) for Bloch wavefunctions of trap depths 8 and 20 E_r. The real part of the wavefunction is plotted.

As shown in Figure 5.1, the bandwidth decreases with increasing trap depth, analogous to the Lamb-Dicke regime in the spectroscopy community [80, 89]. As trap depth increases, eventually $J << \Omega$ where Ω is the Rabi frequency. In the language of atoms trapped in an optical lattice, this corresponds to the atomic wavefunctions becoming increasingly localized. Wavefunctions in this regime may be treated at harmonic oscillators, or building on the Bloch states, Wannier states. The Wannier function for band n on site i in the 1D lattice is given by [49, 54]

$$w(z - z_i) = N^{-1/2} \sum_q e^{-iqz_i/\hbar} \psi_q^n(z). \tag{5.14}$$

See Figure 5.3 for examples.

In clocks, tunneling broadens lineshapes and leads to detrimental systematics. This may be avoided by operation at deep trap depths, or better yet, by providing an energetic offset between lattice sites to suppress tunneling. This is a well known problem in solid state physics with the following Hamiltonian:

$$H = \frac{\vec{p}^{\,2}}{2m} + V(\vec{r}) + F\vec{r}, \tag{5.15}$$

the solutions of which are the well known Wannier-Stark (WS) states [51]. The Hamiltonian is readily realized in a lattice clock by orienting the lattice along gravity [81]. In the Tight-Binding approximation, the WS state for lattice site l may be found to be [50]

$$\begin{aligned} |\Psi_{n,l}\rangle &= \sum_m \mathcal{J}_{m-l}\left(\frac{\Delta_n}{2dF}\right)|m\rangle\,, \\ &= \sum_m \mathcal{J}_{m-l}\left(\frac{4J_0}{Mg\lambda_{lat}}\right)|m\rangle\,. \end{aligned} \tag{5.16}$$

Note the second line is valid for the ground band of the lattice. Here the WS state of lattice site m is given by $|m\rangle$, J_i is the Bessel function of the first kind for order i, Δ_n is the bandwidth of the band n, d the distance of the lattice spacing, and F the applied force as given in Equation 5.15. This simplifies to the second line for the Sr1 system where M is the mass of the Sr atom, g gravity,

$\lambda_{lat} = 813$ nm, and $J_0 \approx (4/\sqrt{\pi}) E_r^{1/4} V_0^{3/4} \exp\left[-2\sqrt{V_0/E_r}\right]$ (valid for the ground band)[34, 1]. Numerical results are plotted in Figure 5.4.

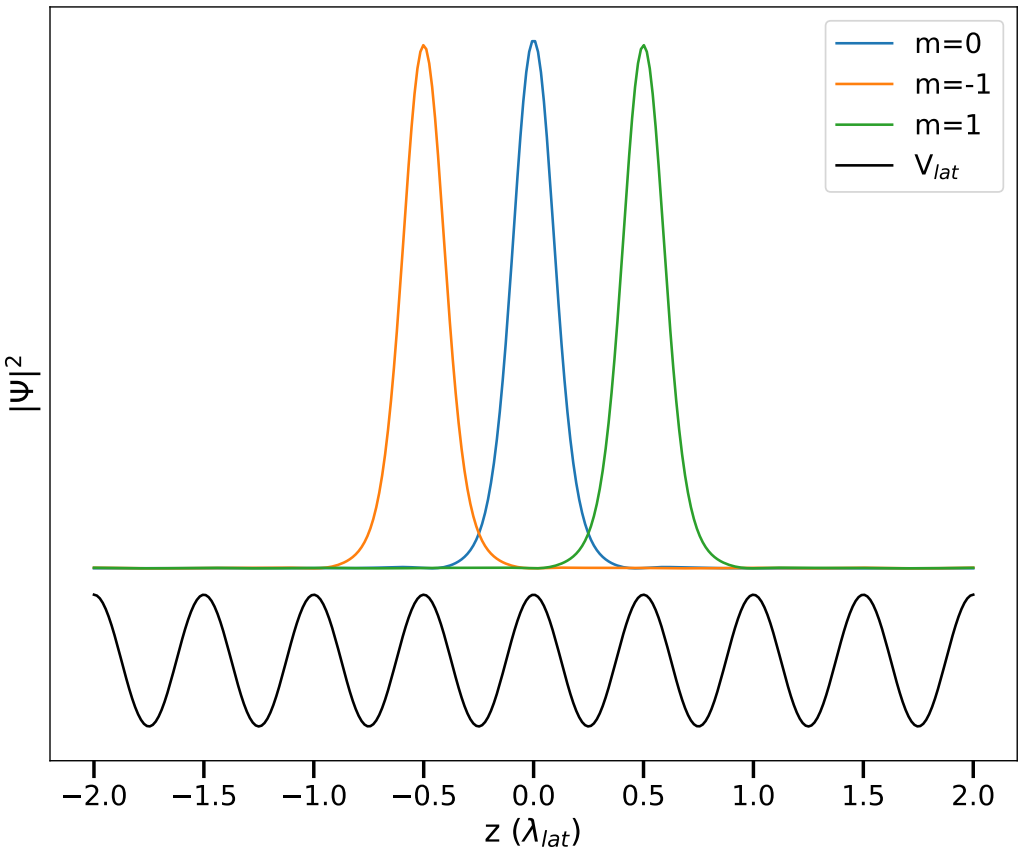

Figure 5.3: Example Wannier state probability distributions as a function of lattice position at a trap depth of 3 E_r. m gives the lattice index for each plotted Wannier function. The optical lattice potential is plotted in black for reference.

5.2 Spin-orbit Coupling

The solid state tools used in the previous section for calculating wavefunctions provide a powerful analytical tool for the study of atomic clocks. Historically, the mature field of ion clocks enabled rapid progress in optical lattice clocks using the framework of ions in harmonic traps

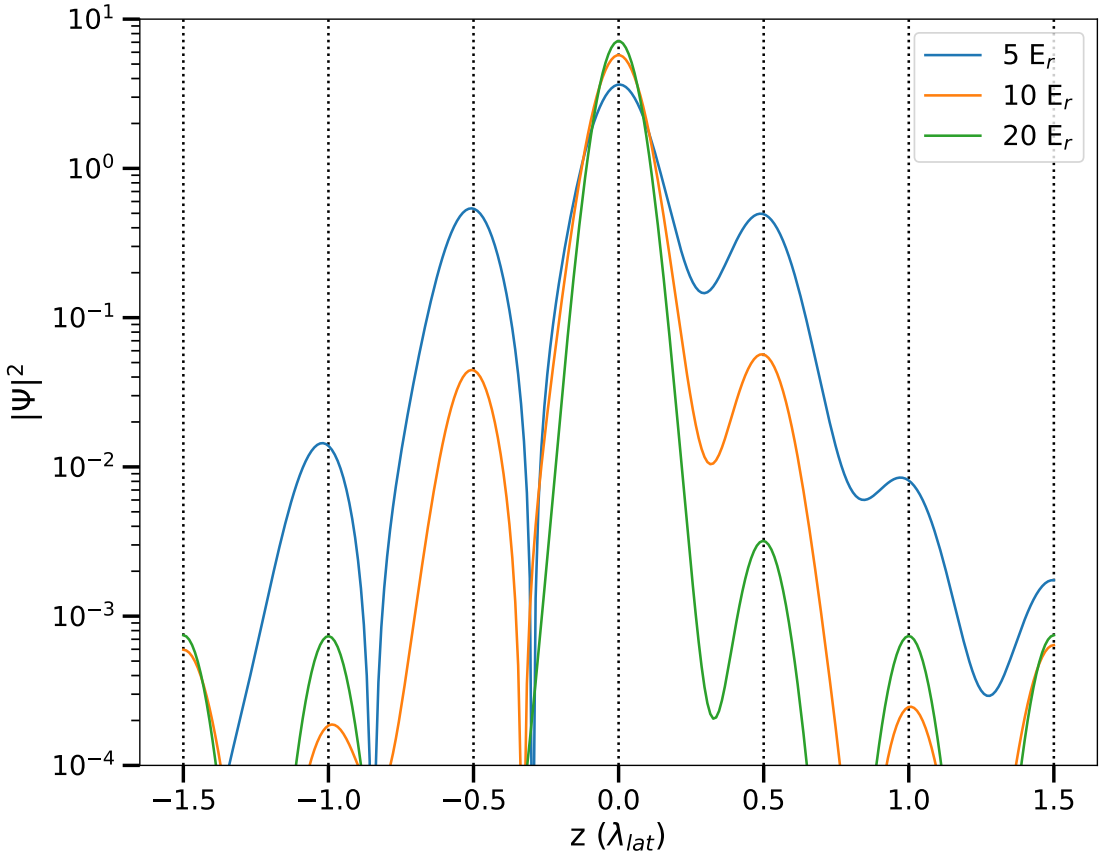

Figure 5.4: Wannier-Stark state probability distributions for a variety of trap depths. All states are centered at $m = 0$, making clear the increasing off-site contributions as trap depth is decreased. This delocalization of the wavefunction provides the ability to tune the overlap of wavefunctions between lattice sites, creating a tunable channel for s-wave interactions.

[80, 89]. In contrast, studies of many-body physics in the 1D lattice clock [95, 155, 25] and the development and study of the 3D lattice clock [33, 52] exemplify the importance of the solid state approach. A great example of this is the Sr2 proposal paper discussing increased lattice constants for operation of shallow trap depths without motional dephasing [67].

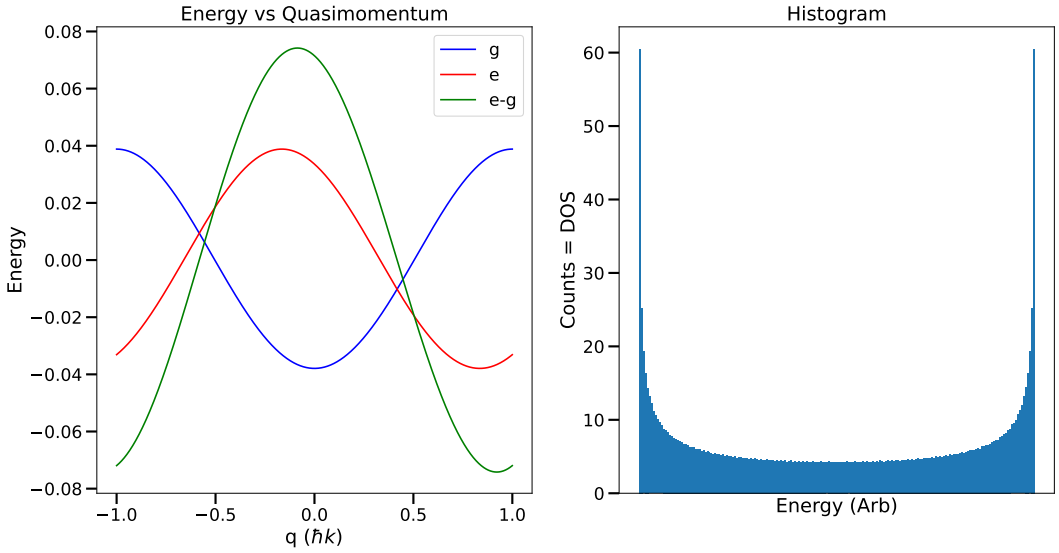

Figure 5.5: Spin-orbit coupling in a horizontal 1D lattice. **Left:** Ground Bloch bands for 10 E_r for both ground (g) and excited (e) clock states with the energy of the clock photon subtracted. The excited band has been shifted by the momentum of the clock photon. Due to this, the energy difference between e and g depends on quasimomentum, coupling spin to momentum (SOC). **Right:** A histogram of energy difference with evenly sampled quasimomentum. The turning points of the energy difference in the left plot correspond to an increased number of quasimomentum points at large detunings - the Van Hove Singularities.

To exemplify this point further we briefly review the origins of spin-orbit coupling (SOC) in the Sr1 system with a horizontal (perpendicular to gravity) lattice [76, 25]. We return to the Bloch bands of Figure 5.1. Immediately we note that the energy associated with a particle is dependent on its quasimomentum. In a magic trap (the same potential for ground and excited clock state) the bands are the same, but we must account for the change in quasimomentum from absorption of a clock photon (Figure 5.5). We find that this intricately links the energy for the $|g\rangle$ to $|e\rangle$ transition to the particles quasimomentum - giving rise to SOC in a neutral atom system (and connecting to

the field of synthetic gauge fields [84]).

Clock spectroscopy of such a system serves as a probe of the density of states (DOS). This is readily understood by connecting clock detuning to quasimomentum and excitation fraction to the DOS at that quasimomentum. Clock spectroscopy of the SOC Sr1 system revealed sharp features in the lineshape (Figures 5.5 and 5.6), an observation of Van Hove singularities [142, 49].

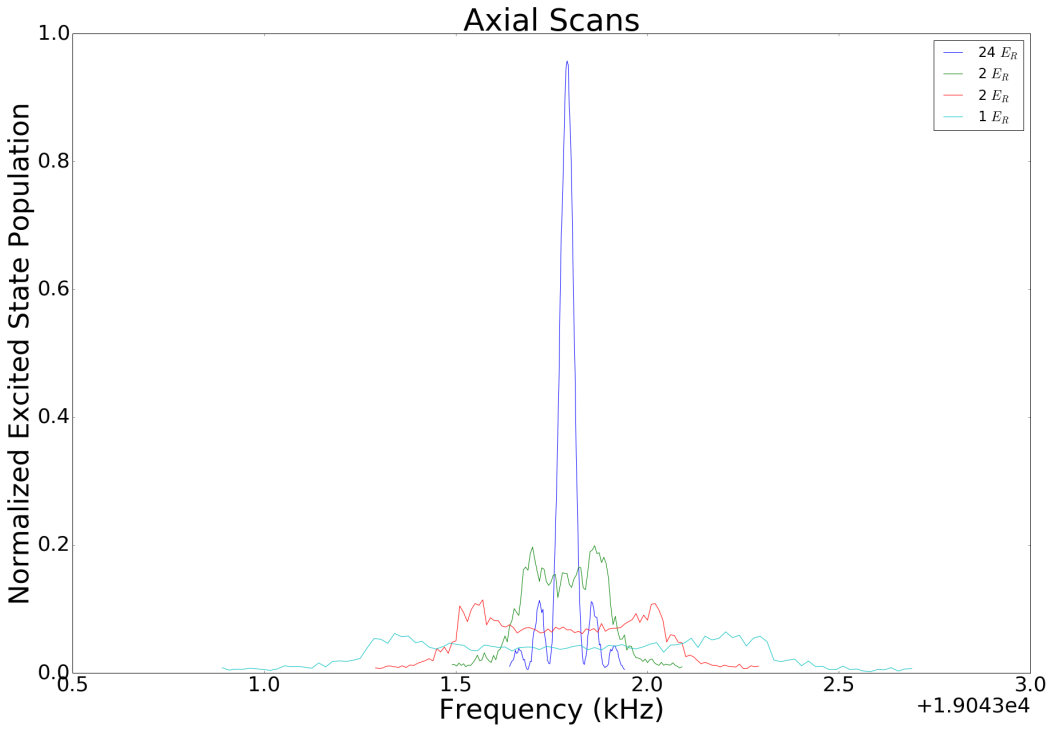

Figure 5.6: Fractional excitation versus detuning for varying depths in the horizontal lattice [76]. As the trap depth decreases, the carrier clearly broadens and shows the emergence of Van Hove singularities.

5.3 The Spin-Model

We now turn our attention for the remainder of the chapter to a qualitative discussion of the spin model using the Bloch sphere. The reader is referred to the extensive literature for a full treatment [94, 95, 118]. We begin by reviewing the effect of monochromatic radiation on a two-level

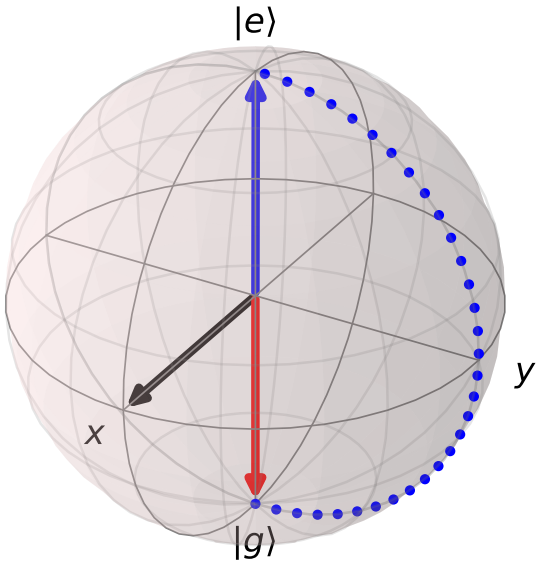

Figure 5.7: A π-pulse on the Bloch sphere. A resonant monochromatic field (laser) applies a field along $\hat{x}$ (black arrow). A spin initially at $|g\rangle$ (red arrow) then begins to precess around the bloch sphere (blue dots), ending at $|e\rangle$ (blue arrow) for a π pulse.

atom using the Bloch sphere picture. The Bloch vector $\hat{U}$ on the Bloch sphere evolves as

$$\frac{d\vec{U}}{dt} = \vec{\Omega} \times \vec{U} \tag{5.17}$$

where $\vec{\Omega} = (\Omega_1, 0, 0)$ for monochromatic radiation (our laser) with no detuning. Recall that this is analagous to a spin in a magnetic field, which we will connect to the spin model. An example of a π pulse is given in Figure 5.7, illustrating the single particle physics of resonantly addressing a ground state atom with a π pulse.

We now want to understand how this picture changes with atomic interactions. We begin by taking advantage of the fact that the Hamiltonian describing the spin model (atomic interactions) in our system has been mapped to the XXZ Heisenberg spin model (we will call this the XXZ model to avoid confusion) given by [48]:

$$\begin{aligned} H_{XXZ} &= -J\sum_{n=1}^{N}[S_n^x S_{n+1}^x + S_n^y S_{n+1}^y + \Delta S_n^z S_{n+1}^z] - 2h\sum_{n=1}^{N} S_n^z, \\ &= -J\sum_{n=1}^{N} S_n \cdot S_{n+1} - J(\Delta - 1)\sum_{n=1}^{N} S_n^z S_{n+1}^z - 2h\sum_{n=1}^{N} S_n^z. \end{aligned} \tag{5.18}$$

Here n denotes the index of a spin, h is a magnetic field, J the strength of spin-spin interactions, and $S_n^\alpha = \frac{1}{2}\sigma_n^\alpha$ with σ^α being the Pauli matrices. In the Sr system this will be a large, collective spin with $S = N_L/2$ (N_L being the number of atoms on site L). Δ sets the strength of the anisotropy of the spin-spin interaction. This is a 1D spin system with a longitudinal field that can exhibit ferromagnetic, paramagnetic, and anti-ferromagnetic order depending on Δ and h [48]. The magnitude of Δ relative to J sets whether the spin-spin interactions are dominated by radial or longitudinal interactions ($\hat{x}$ and $\hat{y}$ versus $\hat{z}$ on the Boch sphere).

Notice that in Equation 5.18 the second line is written such that the first summation corresponds to an isotropic spin-spin term. This is a critical for our understanding of atomic interactions with clock spectroscopy. We wish to understand the effect of Equation 5.18 on the evolution of a collection of atoms exposed to a π pulse (Figure 5.7). Assuming conservation of total spin S and

a mean-field picture, the isotropic spin-spin interaction does not affect the evolution of the system meaning we are concerned only with the second and third summations in Equation 5.18 with contributions along $\hat{z}$. In our Bloch sphere picture this may be understood as a fictitious longitudinal magnetic field. In the spin model for the clock, it has been shown that in the mean field treatment of our system that we have a fictitious magnetic field [95, 94, 34, 1]

$$B_z(N) = NC + 2\chi\langle S_z\rangle \tag{5.19}$$

where N is the number of atoms on a lattice site and $\langle S_z\rangle$ the expectation value of $S_z = \sum_{j=1}^{N} S_z^j$. For a pulse area of θ, $\langle S_z\rangle = -N/2\cos(\theta)$ [95]. C and χ are non-trivial interaction parameters. In the presence of spin-orbit coupling χ is defined by a mixture of s- and p-wave two-body interactions (only p-wave in the absence of SOC) while C is dominated by p-wave interactions. The addition of this effective magnetic field serves to perturb the axis the spin of our clock precesses about. Also note the dependence of Equation 5.19 on N - each lattice site with a different atom number will experience a different B_z and therefore different detuning, a lineshape broadening mechanism limiting coherence times.

To qualitatively understand this we can modify $\vec{\Omega}$ from Equation 5.17 to be $\vec{\Omega} \propto (\Omega_1, 0, B_z(N))$. We may then numerically model a π pulse as before, but with the addition of the effective magnetic field arising from interactions. For a resonant pulse, the addition of atomic interactions serves to tip the axis preccessed about, leading to reduced rotations in $\hat{z}$, as shown in Figure 5.8.

Figure 5.8 motivates the traditional approach to solving the density shift - make B_z smaller! This can be done by 1) operating with less atoms and/or 2) reducing density through larger trapping volumes or lower trap depths, reducing χ and C.

5.4 The 'Magic Depth'

The rebuilt Sr1 system immediately allowed shallow trap depth operation below 10 E_r. As we began to explore frequency gradients throughout our system using imaging techniques we also began

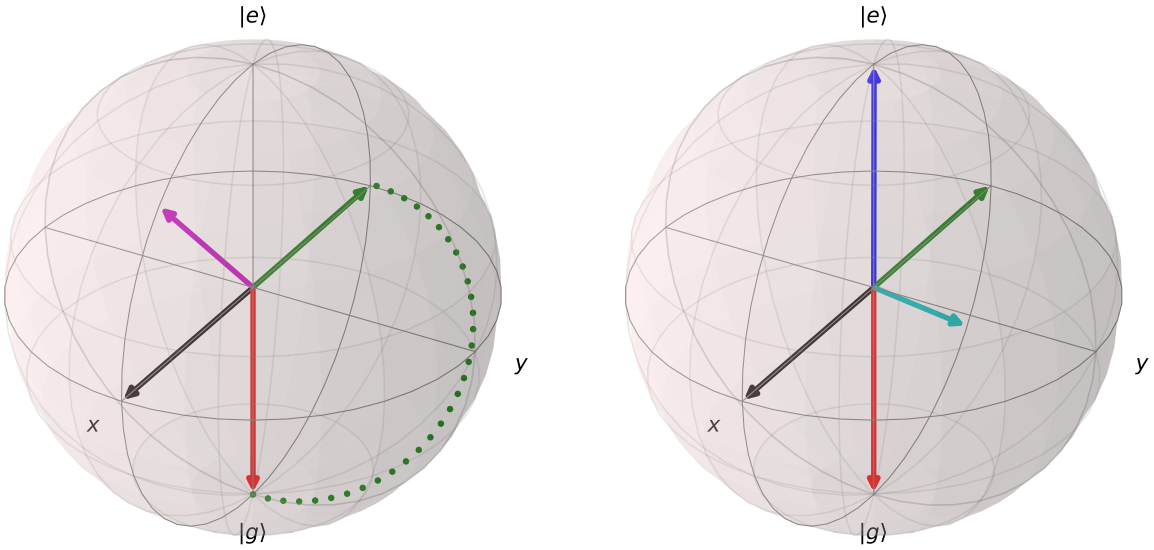

Figure 5.8: π pulses with atomic interactions, with the spin starting in $|g\rangle$ (red arrow). $\Omega_x = 1$ (black arrow), χ=0, and C=0.1. **Left:** π-pulse evolution for $N = 10$. The magenta arrow shows Ω while the green dots and arrow show the evolution of the spin for a resonant π-pulse. **Right:** Same as **left**, but for N =0,10, and 20 corresponding to blue, green, and cyan arrows. For a system of traps with differing atom number each site's collective spin will evolve differently.

to track the density shift per atom per lattice site $\Delta\nu_{atom}$. Originally operating from $|e\rangle \rightarrow |g\rangle$ we continued to explore shallower depths, maintaining high pulse fidelity even for multi-second pulses. Naturally we continued to go shallower, reducing Raman scattering, lattice light shifts, and the density shift.

Measurements of $\Delta\nu_{atom}$ versus trap depth are shown in Figure 5.9. To our disappointment (both for $|e\rangle \rightarrow |g\rangle$ and $|g\rangle \rightarrow |e\rangle$) $\Delta\nu_{atom}$ diverged at shallow depths. Initially we took just the $|e\rangle \rightarrow |g\rangle$ curve, choosing to operate at the minima of $|\Delta\nu_{atom}|$.

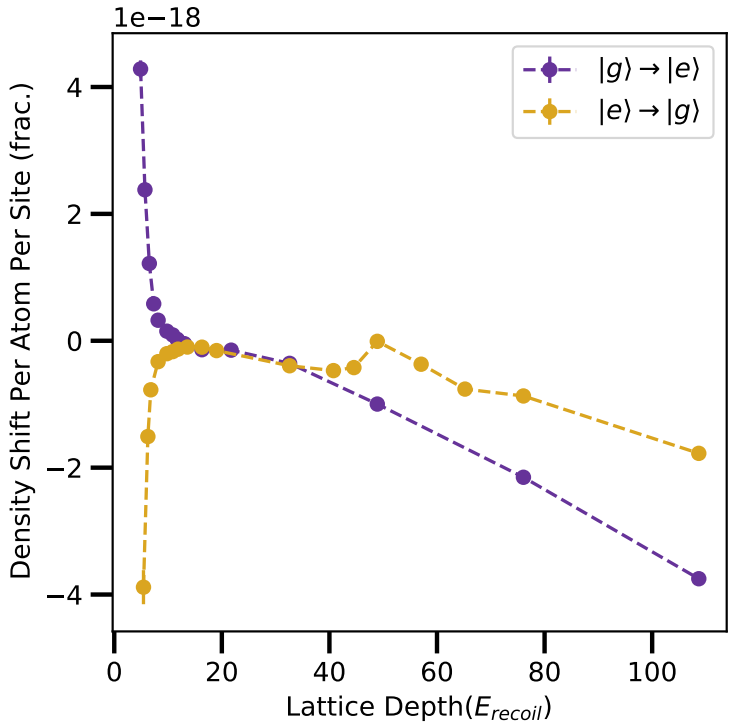

Figure 5.9: Density shift per atom per site in fractional frequency units versus trap depth. At large depths both curves follow the $U^{5/4}$ scaling of Chapter 2, but deviate rapidly at shallow depths.

Fortunately we have the information we need in this chapter to understand Figure 5.9. As we have established lowering trap depth is a good way to reduce p-wave interactions between atoms (and residual s-wave interactions from nuclear spin impurities). However, as we continue decreasing the trap depth the atomic wavefunctions delocalize (Figure 5.4), enabling WS states centered on different lattice sites to appreciably overlap. This introduces a s-wave component that actually

increases relative to the p-wave contribution as trap depth continues to decrease.

Why do the curves in Figure 5.9 diverge different ways? The qualitative argument comes from Equation 5.19. The expectation value $\langle S_z \rangle$ goes from -1 to 1, so starting in $|g\rangle$ versus $|e\rangle$ and performing a π pulse changes the sign. Thus when $\chi >> C$ the density shift diverges with opposite signs.

Most importantly, Figure 5.9 informs us of a different approach to reducing Equation 5.19. Tuning the trap depth to where $\Delta\nu_{atom} = 0$ for the $|g\rangle \rightarrow |e\rangle$ curve of Figure 5.9 corresponds to zero fictitious magnetic field

$$\begin{aligned} 0 &= NC + 2\chi\langle S_z \rangle, \\ &= N[C - \chi\cos(\theta)]. \end{aligned} \tag{5.20}$$

We see that we can cancel the interaction parameters by tuning a combination of pulse depth to adjust the cosine contribution or trap depth to adjust C and χ. In our case, rather than tune the pulse area we adjust the trap depth to find this zero crossing. We call this the 'magic depth' as the density shift vanishes regardless of atom number - it is an experiment specific condition. An example evaluation is shown in Figure 5.10. With the 'magic depth' we now have the ability to combine the accuracy of the 1D system with previously unheard of precision.

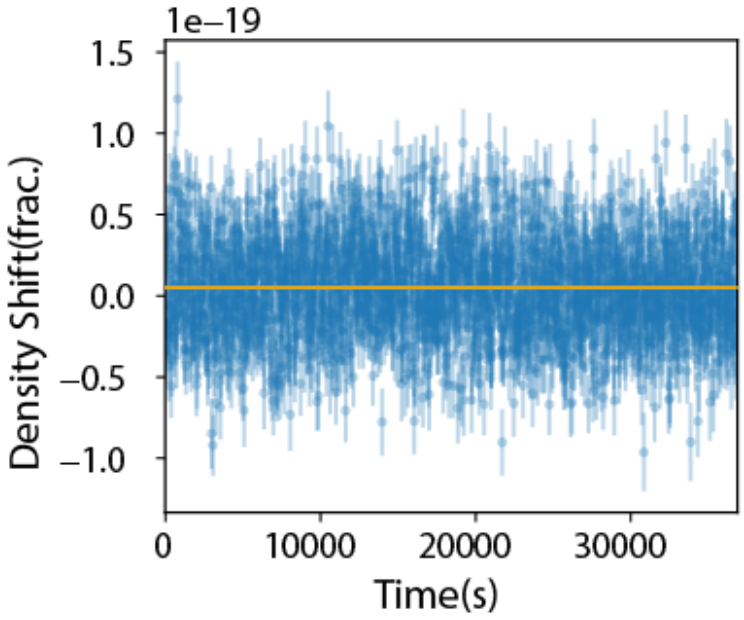

Figure 5.10: 'Magic depth' operation at 12 E_r. Over a 10 hour measurement the fractional density shift was found to be 5.0 $(2.8)\times10^{-21}$ per atom per lattice site.

Chapter 6

Resolving the gravitational redshift within a millimeter atomic sample

The research in this chapter is reported in the publication: Bothwell et al., 'Resolving the gravitational redshift within a millimeter atomic sample,' arXiv (2021) [20].

Modern atomic clocks embody Arthur Schawlow's motto to 'never measure anything but frequency.' This deceptively simple principle, fueled by the innovative development of laser science and quantum technologies based on ultracold matter, has led to dramatic progress in clock performance. Recently, clock measurement precision reached the mid-19^{th} digit in one hour [33, 112], and three atomic species achieved systematic uncertainties corresponding to an error equivalent to less than 1 s over the lifetime of the Universe [109, 98, 24, 19]. Central to this success in neutral atom clocks is the ability to maintain extended quantum coherence times while using large ensembles of atoms [33, 112, 93]. The pace of progress has yet to slow. Continued improvement in measurement precision and accuracy arising from the confluence of metrology and quantum information science [116, 73, 78, 154] promises discoveries in fundamental physics [123, 74, 38, 77].

Clocks fundamentally connect space and time, providing exquisite tests of the theory of general relativity. Hafele and Keating took cesium-beam atomic clocks aboard commercial airliners in 1971, observing differences between flight-based and ground-based clocks consistent with special and general relativity [58]. More recently, RIKEN researchers compared two strontium optical lattice clocks (OLCs) separated by 450 m in the Tokyo Skytree, resulting in the most precise terrestrial redshift measurement to date [133]. Proposed satellite-based measurements [79, 137] will provide orders of magnitude improvement to current bounds on gravitational redshifts [**?**]. Concurrently,

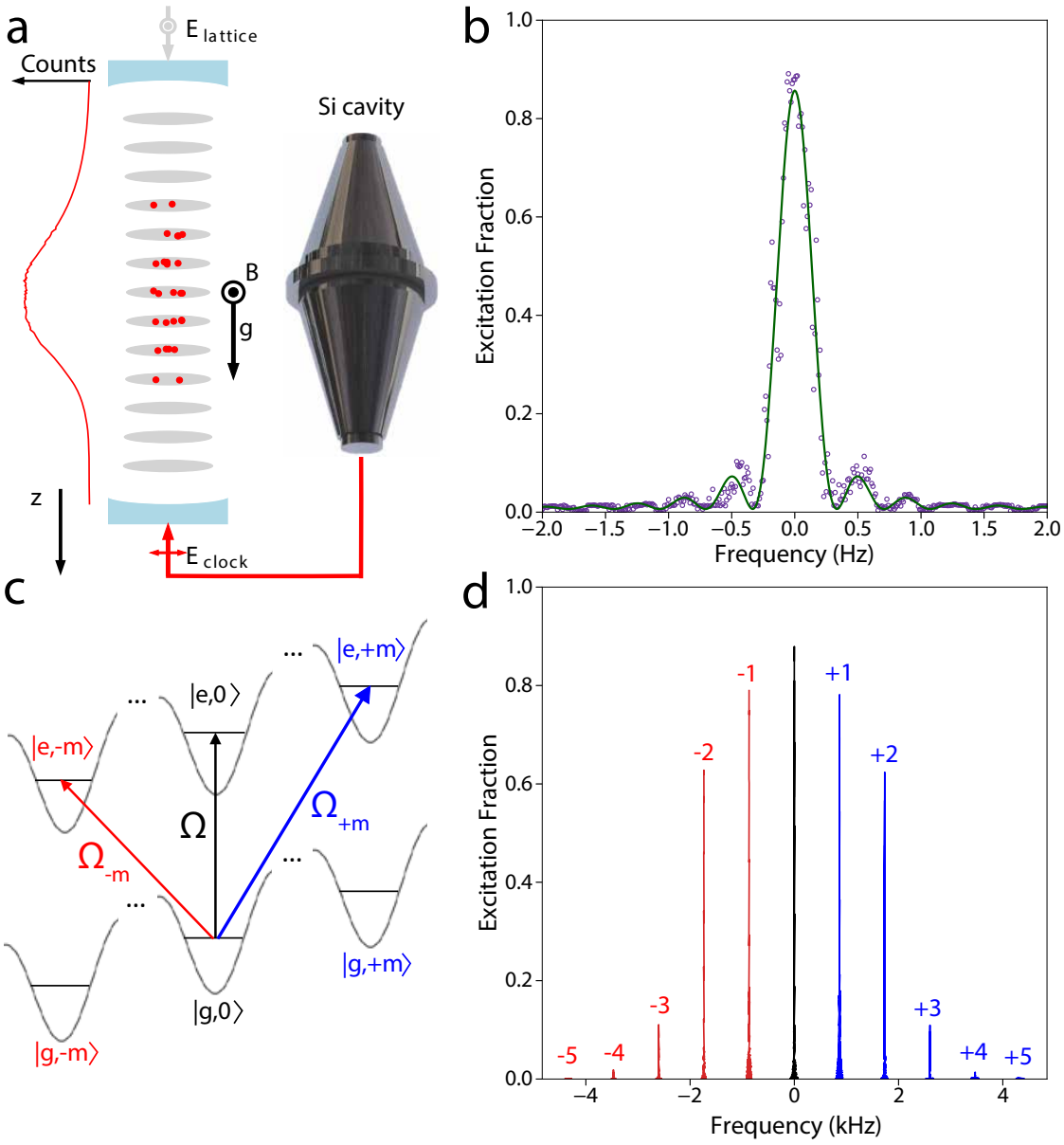

Figure 6.1: Experimental system and quantum state control. **a**, A millimeter length sample of 100,000 ^{87}Sr atoms are trapped in a 1D optical lattice formed within an in-vacuum cavity. The longitudinal axis of the cavity, z, is oriented along gravity. We probe atoms along the $^1S_0 \rightarrow {}^3P_0$ transition using a clock laser locked to an ultrastable crystalline silicon cavity [112, 97]. **b**, Rabi spectroscopy with a 3.1 s pulse time. Open purple circles indicate data with a corresponding Rabi fit in green. **c**, Neighboring lattice sites are detuned by gravity, creating a Wannier-Stark ladder. Clock spectroscopy probes the overlap of Wannier-Stark states between lattice sites that are m sites away with Rabi frequency Ω_m. **d**, Rabi spectroscopy probes Wannier-Stark state transitions, revealing wavefunction delocalization of up to 5 lattice sites. The number of lattice sites is indicated above each transition, with blue(red) denoting Wannier-Stark transitions to higher(lower) lattice sites.

clocks are anticipated to begin playing important roles for relativistic geodesy [56]. In 2010 Chou et al. [35] demonstrated the precision of their Al+ clocks by measuring the gravitational redshift resulting from lifting one clock vertically by 30 cm in 40 hours. With a decade of advancements, today's leading clocks are poised to enable geodetic surveys of elevation at the sub-centimeter level on Earth, a result unobtainable with other current techniques [138].

Atomic clocks strive to simultaneously optimize measurement precision and systematic uncertainty. For traditional OLCs operated with one-dimensional (1D) optical lattices, achieving low instability has involved the use of high atom numbers at trap depths sufficiently large to suppress tunneling between neighboring lattice sites. While impressive performance has been achieved,¬ effects arising from atomic interactions and AC Stark shifts associated with the trapping light challenge advancements in OLCs. Here we report a new operational regime for 1D OLCs, both resolving the gravitational redshift across our atomic sample and synchronously measuring a fractional frequency uncertainty of 7.6×10^{-21} between two uncorrelated regions. Our system employs 100,000 ^{87}Sr atoms at 100 nK loaded into a shallow, large waist optical lattice, reducing both AC Stark and density shifts. Motivated by our earlier work on spin-orbit coupled lattice clocks [76, 26], we engineer atomic interactions by operating at a 'magic' trap depth, effectively removing collisional frequency shifts. These advances enable record optical atomic coherence (37 s) and expected single clock stability (3.1×10^{-18} at 1 s) using macroscopic samples, paving the way toward lifetime limited OLC operation.

Central to our experiment is an in-vacuum optical cavity (Fig. 1a and Methods) for power enhancement of the optical lattice. The cavity (finesse 1100) ensures wavefront homogeneity of our 1D lattice while the large beam waist (260 μm) reduces the atomic density by an order of magnitude compared to our previous system [19]. We begin each experiment by trapping fermionic ^{87}Sr atoms into the 1D lattice at a trap depth of 300 lattice photon recoil energies (E_r), loading a millimeter scale atomic sample (Fig. 1a). Atoms are simultaneously cooled and polarized into a single nuclear spin before the lattice is adiabatically ramped to an operational depth operational depth of 12 E_r and prepare atoms into a single nuclear spin. Clock interrogation proceeds by probing the ultra-

narrow $^1S_0$ (g) $\rightarrow$ $^3P_0$ (e) transition with the resulting excitation fraction measured by fluorescence spectroscopy. Scattered photons are collected on a camera, enabling in-situ measurement with 6 μm resolution, corresponding to $\sim$15 lattice sites (Fig. 1a).

Quantum state control has been vital to recent advances in atom-atom and atom-light coherence times in 3D OLCs and tweezer clocks [33, 93, 154]. Improved quantum state control is demonstrated through precision spectroscopy of the Wannier-Stark states of the OLC [149, 81]. The 1D lattice oriented along gravity has the degeneracy of neighboring lattice sites lifted by the gravitational potential energy. In the limit of shallow lattice depths, this creates a set of delocalized states. By ramping the lattice depth to 6 E_r, much lower than in traditional 1D lattice operations [109, 98, 19], clock spectroscopy probes this delocalization (Fig. 1d). The ability to engineer the extent of atomic wavefunctions through the adjustment of trap depth creates an opportunity to control the balance of on-site p-wave versus neighboring-site s-wave atomic interactions. We utilize this tunability by operating at a 'magic' trap depth [1], where the frequency shifts arising from on-site and off-site atomic interactions cancel, enabling a reduction of the collisional frequency shifts by more than three orders of magnitude compared our previous work [19].

Extended atomic coherence times are critical for both accuracy and precision. An aspirational milestone for clock measurement precision is the ability to coherently interrogate atomic samples up to the excited state's natural lifetime. To evaluate the limits of our clock's atomic coherence, we perform Ramsey spectroscopy to measure the decay of fringe contrast as a function of the free-evolution time. By comparing two uncorrelated regions within our atomic sample, we determine the contrast and relative phase difference between the two sub-ensembles (Fig. 2). The contrast decays exponentially with a time constant of 37 s (quality factor of 3.6×10^{16}), corresponding to an additional decoherence time of 53 s relative to the $^3P_0$ natural lifetime (118 s [104]). This represents the longest optical atomic coherence time measured in any spectroscopy system to date.

We utilize Rabi spectroscopy in conjunction with in-situ imaging to microscopically probe clock transition frequencies along the entire vertically oriented atomic ensemble. With a standard interleaved probing sequence using the $|g, m_F = \pm 5/2\rangle$ to $|e, m_F = \pm 3/2\rangle$ transitions for minimal

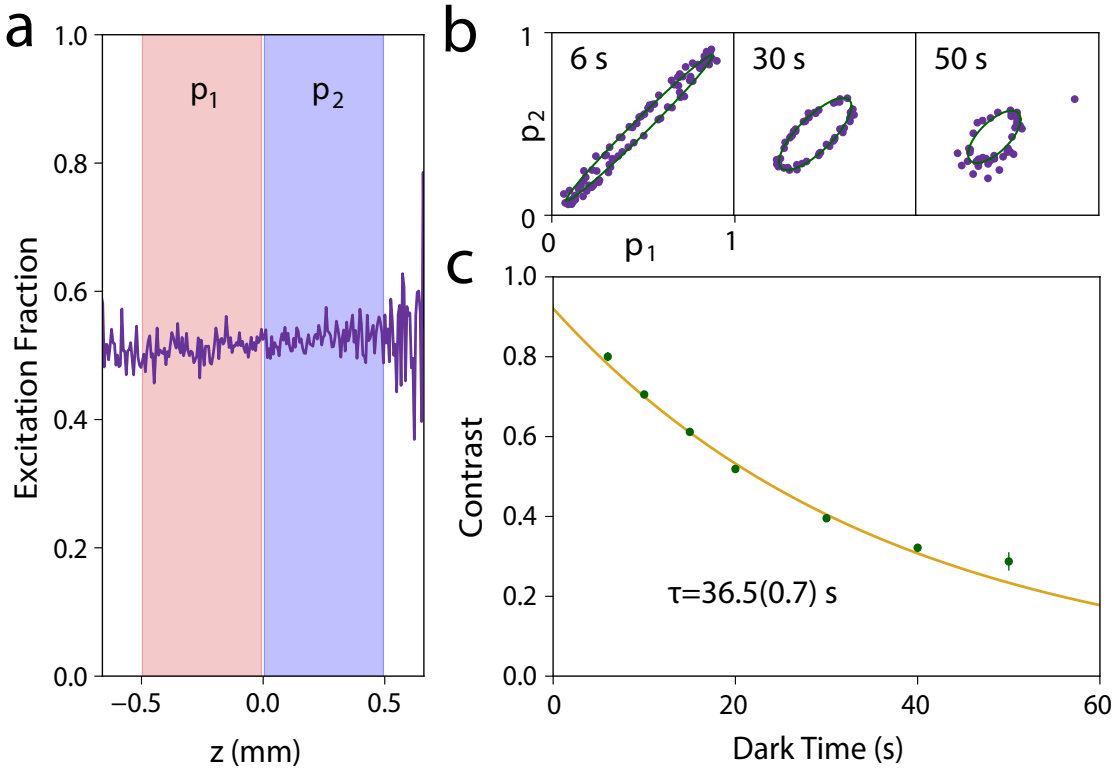

Figure 6.2: Atomic coherence. We use Ramsey spectroscopy with a randomly sampled phase for the second pulse to determine the coherence time of our system [93]. **a**, We measure the excitation fraction across the cloud, shown in purple for a single measurement, and calculate the average excitation fractions in regions p_1 and p_2, separated by 2 pixels. **b**, Parametric plots of the excitation fraction of p_1 versus p_2 in purple for 6 s, 30 s and 50 s dark time demonstrate a phase shift between the two regions and contrast decay. Using a maximum likelihood estimator, we extract the phase and contrast for each dark time with the fit, shown in green. **c**, Contrast decay as a function of time in green is fit with an exponential decay in gold, giving an atomic coherence decay time of 36.5(0.7) s and a corresponding quality factor of 3.6×10^{16}. After accounting for the finite radiative decay contribution, we infer an additional decoherence time constant of 52.8(1.5) s.

magnetic sensitivity, we reject the first order Zeeman shifts and vector AC Stark shifts. The in-situ imaging of atoms in the lattice allows measurement of unprocessed frequencies across the entire atomic sample (Fig. 1a and Methods). The dominant differential perturbations arise from atom-atom interactions (residual density shift contributions after we operate at the 'magic' trap depth) and magnetic field gradients giving rise to pixel-specific second order Zeeman shifts. Using the total camera counts and m_F-dependent frequency splitting, we correct the density and second order Zeeman shift at each pixel. These corrections result in the processed frequencies per pixel shown in Fig. 3a, with error bars representing the quadrature sum of statistical uncertainties from the center frequency, the density shift correction, and the second order Zeeman shift correction. Additional systematics are described in the Methods. This approach demonstrates an efficient method for rapid and accurate evaluation of various systematic effects throughout a single atomic ensemble. Unlike traditional 1D OLCs where systematic uncertainties are quoted as global parameters, we now microscopically characterize these effects.

This new microscopic in-situ imaging allows determination of the gravitational redshift within a single atomic sample, probing an uncharacterized fundamental clock systematic. Two identical clocks on the surface of a planet separated by a vertical distance h will differ in frequency (δf) as given by

$$\frac{\delta f}{f} = \frac{ah}{c^2}, \tag{6.1}$$

with f the clock frequency, c the speed of light, and a the gravitational acceleration. The gravitational redshift at Earth's surface corresponds to a fractional frequency gradient of -1.09×10^{-19}/mm in the coordinate system of Fig. 1a. Measurement of a vertical gradient across the atomic sample consistent with the gravitational redshift provides an exquisite verification of an individual atomic clock's frequency control.

Our intra-cloud frequency map (Fig. 3a) allows us to evaluate gradients across the atomic sample. Over 10 days we performed 14 measurements (ranging in duration from 1-17 hours) to

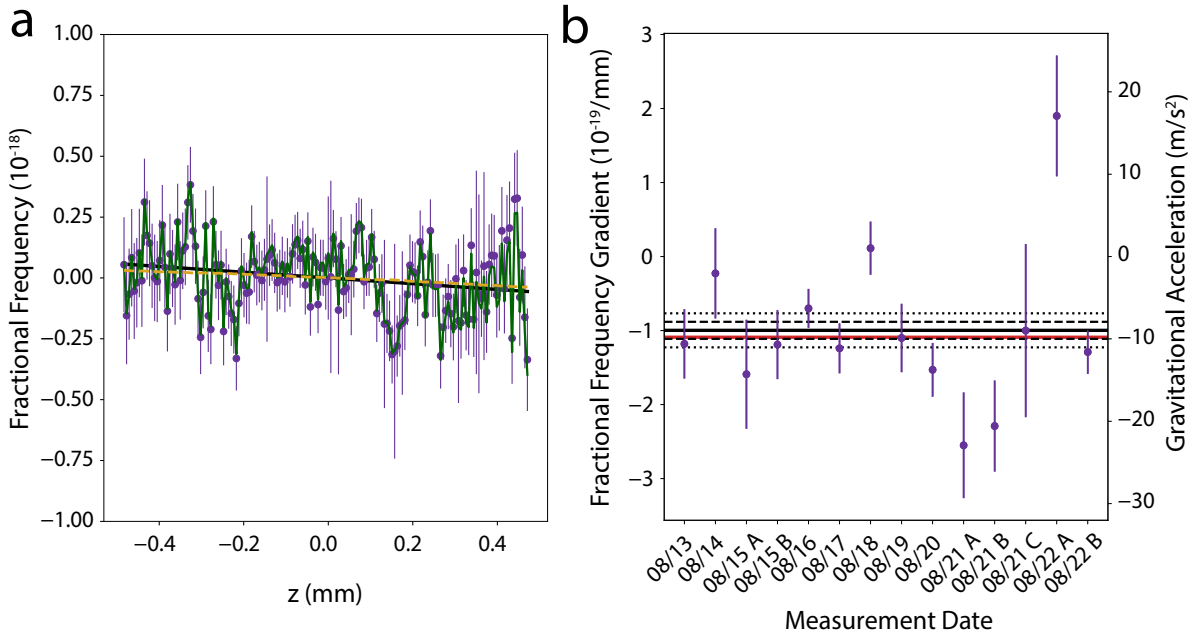

Figure 6.3: Evaluating frequency gradients. **a**, For each measurement we construct a microscopic frequency map across the sample, with raw frequencies shown in green. The second order Zeeman correction is shown as a dashed gold line. Processed frequencies shown in purple include both density shift corrections and second order Zeeman corrections, with uncertainties arising from the quadrature sum of statistical, density shift correction, and second order Zeeman correction uncertainties. To this we fit a linear function, shown in black. **b**, Over the course of 10 days, we completed 14 measurements. For each measurement, we create a corrected frequency map and fit a linear slope as in a. This slope is plotted for each measurement, as well as a weighted mean (black) with associated statistical uncertainty (dashed black) and total uncertainty as reported in this chapter's table (dotted black). The expected gravitational gradient is shown in red. All data is taken with Rabi spectroscopy using a 3.1 s π-pulse time except for 08/13 which used a 3.0 s pulse time. The reduced chi-square statistic is 3.0, indicating a small underestimation of error variances entirely consistent with the additional systematic uncertainties in Table 1.

search for the gravitational redshift across our sample. For each dataset we fit a linear slope and offset, reporting the slope in Fig. 3b. From this measurement campaign we find the weighted mean (standard error of the weighted mean) of the frequency gradient in our system to be $-1.00(12) \times 10^{-19}$/mm. We evaluate additional differential systematics (see Methods) and find a final frequency gradient of $-9.8(2.3) \times 10^{-20}$/mm, consistent with the predicted redshift.

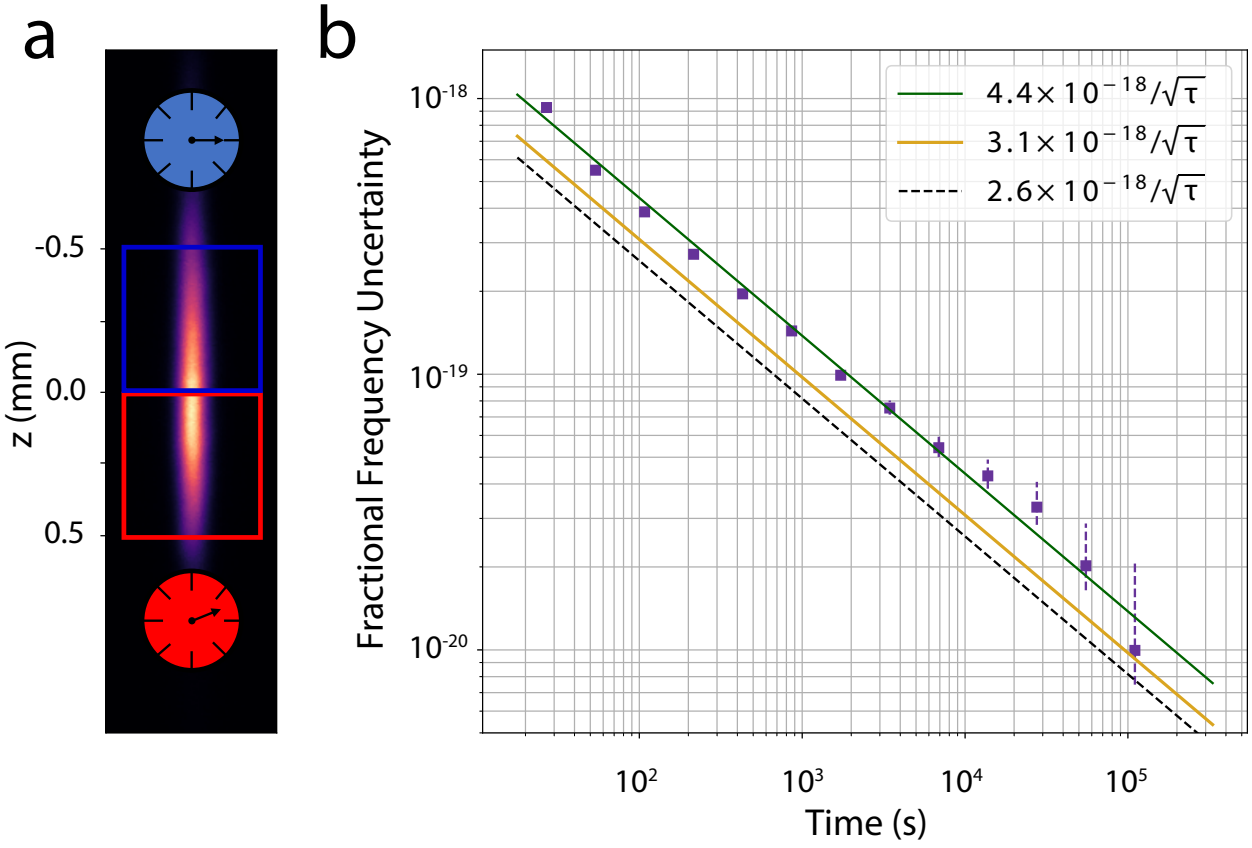

Figure 6.4: In-situ synchronous clock comparison. **a**, The cloud is separated as in Fig. 2a. The gravitational redshift leads to the higher clock(blue) ticking faster than the lower one(red). The length scale is in millimeters. **b**, Allan deviation of the frequency difference between the two regions in a over 92 hours. Purple points show fractional frequency instability fit by the solid green line, with the quantum projection noise limit indicated by the dashed black line. We attribute the excess instability of the measurement relative to QPN to detection noise. The expected single atomic region instability is shown in gold.

The ability to resolve the gravitational redshift within our system suggests a level of frequency control beyond previous clock demonstrations, vital for the continued advancement of clock

accuracy and precision. Previous fractional frequency comparisons [154] have reached uncertainties as low as 4.2×10^{-19}. Similarly, we perform a synchronous comparison between two uncorrelated regions of our atomic cloud (Fig. 4a). By binning ∼100 pixels per region, we substantially reduce instability caused by quantum projection noise [89]. Analyzing the frequency difference between regions from 92 hours of data, we find a fractional frequency instability of $4.4 \times 10^{-18}/\sqrt{\tau}$ (τ is the averaging time in seconds), resulting in a fractional frequency uncertainty of 7.6×10^{-21} for full measurement time, nearly two orders of magnitude lower than the previous record. From this measurement we infer a single region instability of $3.1 \times 10^{-18}/\sqrt{\tau}$. Dividing the fractional frequency difference by the spatial separation between each region's center of mass gives a frequency gradient of $-1.30(18) \times 10^{-19}$/mm. Correcting for additional systematics as before results in a gradient of $-1.28(27) \times 10^{-19}$/mm, again fully consistent with the predicted redshift.

In conclusion, we have established a new paradigm for atomic clocks. The vastly improved atomic coherence and frequency homogeneity throughout our sample allow us to resolve the gravitational redshift at the submillimeter scale, observing for the first time the frequency gradient from gravity within a single sample. We demonstrate a synchronous clock comparison between two uncorrelated regions with a fractional frequency uncertainty of 7.6×10^{-21}, advancing precision by nearly two orders of magnitude. These results suggest that there are no fundamental limitations to inter-clock comparisons reaching frequency uncertainties at the 10^{-21} level, offering new opportunities for tests of fundamental physics.

6.1 Methods

6.1.1 In-Vacuum Cavity

Central to our system is an in-vacuum lattice buildup cavity oriented along gravity (Fig. 1a). Two mirrors with radius of curvature of 1 m are separated by ∼17 cm, achieving a mode waist of 260 μm. Our over-coupled cavity has a finesse at the lattice wavelength (813 nm) of 1100 and a power buildup factor of 700 (ratio of circulating to input intensity). This enables lattice

depths in excess of 500 E_r (lattice photon recoil energy) using a diode-based laser system. The dimensional stability of the cavity combined with the simplified diode laser system enables robust operation compared with our previous Ti:Sapphire retro-reflected design [19]. The cavity mirrors are anti-reflection coated at the clock wavelength of 698 nm.

One cavity mirror is mounted to a piezo for length stabilization while the other mirror is rigidly mounted for phase reference for the clock laser. Grounded copper shields between atoms and mirrors prevent DC Stark induced shifts due to charge buildup on the mirrors and piezo [29, 85]. Each shield (5 mm thick) has a centered hole of 6 mm diameter to accommodate the optical lattice beam, with shielding performance verified through evaluation of the DC Stark shift systematic.

6.1.2 Atomic Sample Preparation

^{87}Sr atoms are cooled and loaded into a 300 E_r optical lattice using standard two stage magneto-optical trapping techniques [19]. Once trapped, atoms are simultaneously nuclear spin polarized, axially sideband cooled, and radially doppler cooled into a single nuclear spin state at temperatures of 800 nK. The lattice is then adiabatically ramped to the operational trap depth of 12 E_r, where a series of pulses addressing the clock transition prepares atoms into $|g, m_F = \pm 5/2\rangle$. Clock spectroscopy is performed by interrogating the $|g, m_F = \pm 5/2\rangle$ to $|e, m_F = \pm 3/2\rangle$ transition, the most magnetically insensitive ^{87}Sr clock transition [112].

6.1.3 Imaging

The clock excitation fraction is read out using standard fluorescence spectroscopy techniques [33, 93, 80]. Photons are collected on both a photo-multiplier tube for global readout and electron multiplying charge coupled device camera for an in-situ readout of clock frequency. Camera readout is performed in full vertical binning mode, averaging the radial dimension of the lattice. This provides 1D in-situ imaging for all synchronous evaluations.

We use a 25 μs fluorescence probe with an intensity of $I/I_{sat} \sim 20$ (I_{sat} being the saturation intensity), ensuring uniform scattering across the atomic sample. Before imaging, the optical

lattice is ramped back to 300 E_r to decrease imaging aberration resulting from the extended radial dimension at 12 E_r.

6.1.4 Analysis

Standard clock lock techniques and analysis are used [112, 93, 89], with differences in excitation fraction converted to frequency differences using Rabi lineshapes. Each dataset is composed of a series of clock locks, tracking the center of mass frequency of the atomic sample. A clock lock is four measurements probing alternating sides of the Rabi lineshape for opposite nuclear spin transitions. Frequency corrections based on excitation fraction become ambiguous when the excitation fraction measured is consistent with the Rabi lineshape at multiple detunings. To avoid erroneous frequency corrections, we remove clock locks with excitation fractions above (below) .903×C (.116×C), where C is the Rabi contrast. From each clock lock, a pixel specific center frequency f_i and frequency splitting between opposite m_F states Δ_i are calculated, creating an in-situ frequency map of the 1D atomic sample. This allows rejection of vector shifts on a pixel-by-pixel basis and probes the magnetic field induced splitting of mF transitions. The atom weighted mean frequency is subtracted from every lock cycle to reject common mode laser noise.

For each dataset we approximate the atomic profile with a Gaussian fit, identifying a center pixel and associated Gaussian width (σ). All analysis is performed within the central region of $\pm 1.5\sigma$ which demonstrates the lowest frequency instability. Identifying a center pixel for data processing ensures rejection of any day-to-day drift in the position of the cloud due to varying magnetic fields modifying MOT operation on the narrow line transition. The density shift coefficient (see Density Shift section) is derived from the average center frequency per pixel. Using this coefficient, we correct fi and Δ_i for the density shift. second order Zeeman corrections using these updated frequencies are then applied.

Gradient analysis is based on the processed center frequencies per pixel. A linear fit to the frequencies as a function of pixel is performed using least squares, with uncertainty per pixel arising from the quadrature sum of statistical frequency uncertainty, statistical second order Zeeman

uncertainty, and density shift correction uncertainty.

For the two-clock comparison (Fig. 4b), all data from 8/14-8/22 was taken with the same duty cycle and π-pulse time (3.1 s). Data was processed relative to a fit center pixel as discussed and concatenated. Two equal regions extend from the center of the sample to a width of $\pm 1.5\sigma$, with two empty pixels between regions to ensure uncorrelated samples. Each region is processed for the atom weighted mean frequency, enabling a synchronous frequency comparison between two independent clocks.

6.1.5 Atomic Coherence

We use a Ramsey sequence to measure the atomic coherence. We prepare a sample in the $|g, m_F = +5/2\rangle$ state and apply a $\pi/2$ pulse along the $|g, m_F = +5/2\rangle$ to $|e, m_F = +3/2\rangle$ transition. After waiting for a variable dark time, we apply a second $\pi/2$ pulse with a random phase relative to the first. We then measure the excitation fraction.

Two regions, p_1 and p_2, are identified using the same technique as in the synchronous instability measurement. For each experimental sequence, we find the average excitation fraction in p_1 and p_2. A mean frequency shift across the sample primarily due to a magnetic field gradient creates a differential phase as a function of time between p_1 and p_2. We create a parametric plot of the average excitation in p_1 and p_2 for each dark time and use a maximum likelihood estimator to fit an ellipse to each dataset, calculating phase and contrast [154, 93]. To estimate uncertainty in the contrast for each dark time a bootstrapping technique is used [93]. Fitting the contrast as a function of dark time with a single exponential returns an effective atomic coherence time.

6.1.6 Systematics

6.1.6.1 Imaging

We calibrate our pixel size using standard time of flight methods: we observe an atomic sample in freefall for varying times to determine an effective pixel size along the direction of gravity. Immediately after our 10-day data campaign we measured our effective pixel size to be 6.04 μm.

Due to thermal drift of our system, the pixel size can vary by up to 0.5 μm/pixel over months which we take as the calibration uncertainty.

Spatial correlations may limit imaging resolution. We measure these correlations by placing atoms into a superposition of clock states. Any measured spatial correlation is due to the imaging procedure. In our system we find no correlations between neighboring pixels [93]. The optical resolution of our imaging lens is specified at 2 μm.

Lattice tilt from gravity will modify the measured gradient. We find the lattice tilt in the imaging plane to be 0.11(0.06) degrees, providing an uncertainty orders of magnitude smaller than the pixel size uncertainty. We are insensitive to lattice tilt out of the imaging plane.

6.1.6.2 Zeeman Shifts

First order Zeeman shifts are rejected by probing opposite nuclear spin states [112]. The second order Zeeman shift is given by

$$\Delta\nu_{B,22} = \xi(\Delta\nu_{B,1})^2, \tag{6.2}$$

where $\Delta\nu_{B,1}$ is the splitting between opposite spin states and ξ the corresponding second order Zeeman shift coefficient. For stretched spin state operation ($m_F = \pm 9/2$), $\xi = -2.456(3) \times 10^{-7}$ Hz^{-1}. Using known atomic coefficients [22] we find the second order Zeeman coefficient for the $|g, m_F = +5/2\rangle$ to $|e, m_F = +3/2\rangle$ transition to be $\xi_{op} = -1.23(8)\times 10^{-4}$ Hz^{-1}, with the uncertainty arising from limited knowledge of atomic coefficients.

The second Order Zeeman corrections are made for every clock lock (analogous to the in-situ density shift corrections). For a typical day (8/13) the average second order Zeeman gradient is -7.0×10^{-20}/mm, corresponding to a splitting between opposite nuclear spin states of 12.7 mHz/mm (0.291 mG/mm). We include an error of 4×10^{-21}/mm in the below table to account for the atomic uncertainty in the shift coefficient.

6.1.6.3 DC Stark

Electric fields perturb the clock frequency via the DC Stark effect. We evaluate gradients arising from this shift by using in-vacuum quadrant electrodes to apply bias electric fields in all three dimensions. We find a DC Stark gradient of $3(2) \times 10^{-21}$/mm.

6.1.6.4 Black Body Radiation Shift

The dominant frequency perturbation to room temperature neutral atom clocks is black body radiation (BBR). Similar to our previous work [19], we homogenize this shift by carefully controlling the thermal surroundings of our vacuum chamber. Attached to the vacuum chamber are additional temperature control loops, with each vacuum viewport having a dedicated temperature control system. This ensures our dominant BBR contribution – high emissivity glass viewports – are all the same temperature to within 100 mK.

To bound possible BBR gradients, we introduce a 1 K gradient between the top and bottom of the chamber along the cavity axis by raising either the top or bottom viewports by 1 K. We compare these two cases and find no statistically significant changes in the frequency gradient across the entire sample. Accounting for uncertainty in linear frequency fits for each case, we estimate an uncertainty of 3×10^{-21}/mm. This finding is supported with a basic thermal model of the vacuum chamber.

6.1.6.5 Density Shift

Atomic interactions during Rabi spectroscopy lead to clock frequency shifts as a function of atomic density [95]. For each gradient measurement, we evaluate the density shift coefficient χ_{dens} by fitting the average frequency f per pixel versus average camera counts per pixel N to an equation of the form

$$f(N) = \chi_{dens} N + B. \tag{6.3}$$

Here B is an arbitrary offset. Once χ_{dens} is known, we remove the density shift at each pixel.

Residual density shift corrections may lead to error in our linear gradient. To bound this effect, we compare the density shift coefficient and gradient from our data run with a separate dataset at 8 E_r. With the trap depth at 8 E_r we found a linear gradient of s= -1.08×10^{-18}/mm and a density shift coefficient of $\chi_8 = -1.39 \times 10^{-6}$ Hz/count. During our data run we had an average density shift coefficient of $\chi_{op} = -2.43 \times 10^{-8}$ Hz/count. We bound the uncertainty in our gradient from density shift as $\sigma_{den,unc} = |s \times \chi_{op}/\chi_8| = 1.7 \times 10^{-20}$/mm.

6.1.6.6 Lattice Light Shifts

Lattice light shifts arise from differential AC Stark shifts between the ground and excited clock states. An approximate microscopic model of the lattice light shift (ν_{LS}) in our system is given by [140]

$$h\nu_{LS}(u, \delta_L) \approx \left(\frac{\Delta\alpha^{E1}}{\delta\nu} - \Delta\alpha_{QM}\right)\frac{u^{1/2}}{2} - \left[\frac{\delta\alpha^{E1}}{\delta\nu}\delta_L\right]u, \tag{6.4}$$

where u is the trap depth in units of Erec, $\Delta\alpha^{E1}$ the differential electric dipole polarizability, $\Delta\alpha^{QM}$ the differential multi-polarizability, and $\delta_L = (\nu_L - \nu^{E1})$ the detuning between lattice frequency ν_L and effective magic frequency ν^{E1}. Our model has no dependence on the longitudinal vibrational quanta since we are in the ground vibrational band. We neglect higher order corrections from hyperpolarizability due to our operation at depths <60 E_r. At our temperatures thermal averaging of the trap depth is a higher order correction ($< 5\%$) that is also neglected.

We model the linear differential lattice light shift across the atomic cloud as

$$\frac{\delta h\nu_{LS}(u, \delta_L)}{\delta z} \approx \left[\frac{(\frac{\delta\alpha^{E1}}{\delta\nu})}{4u^{1/2}} - \frac{\delta\alpha^{E1}}{\delta\nu}\delta_L\right]\frac{\delta u}{\delta z} \tag{6.5}$$

where z is the coordinate corresponding to the axis of the cavity along gravity. To evaluate our differential lattice light shift at our operational depth we need δ_L and $\frac{\delta u}{\delta z}$. We modulate our lattice between two trap depths ($u_1 = 14$ E_r, $u_2 = 56$ E_r) and find our detuning from scalar magic

frequency to be δ_L=7.4(0.6) MHz. To evaluate $\frac{\delta u}{\delta z}$ at our operational depth (u_{op}) we measure the linear gradient across the atomic cloud at $\delta_L + 250$ MHz and $\delta_L - 250$ MHz, the difference given by

$$\frac{\delta h\nu_{LS}(u_{op}, \delta_{L+250MHz})}{\delta_z} - \frac{\delta h\nu_{LS}(u_{op}, \delta_{L-250MHz})}{\delta_z} \approx \left[\frac{1}{4u_{op}^{1/2}} - 1\right] \frac{\delta\alpha^{E1}}{\delta\nu} \delta_{500} \frac{\delta u_{op}}{\delta z}, \qquad (6.6)$$

where $\delta_{500} = 500$ MHz. We find $(\delta u_{op}/\delta z)$=0.0383/mm, which when combined with $\delta_L = 7.4$ MHz, gives us a fractional frequency gradient of -5×10^{-21}/mm. Accounting for error in our lattice detuning and linear gradient gives us an uncertainty of 1×10^{-21}/mm.

6.1.6.7 Other Systematics

For a 3.1 s π-pulse the probe AC Stark shift7 is -3(2)$\times 10^{-21}$. A frequency scan of the $|g, m_F = -5/2\rangle$ to $|e, m_F = -3/2\rangle$ transition limits the variation of excitation fraction across the atomic sample to 1% or below, bounding any possible probe AC Stark gradient across the sample to $< 1 \times 10^{-22}$.

6.1.6.8 Known Redshift

The gravitational acceleration (rounding to 4 digits) within our lab was evaluated by a USGS survey to be a=-9.796 m/s^2.

Systematic	Slope (10^{-20}/mm)	Uncertainty (10^{-20}/mm)
Gradient	-10.0	1.2
BBR	0	0.3
Density	-	1.7
Lattice light shift	-0.5	0.1
DC Stark	0.3	0.2
Pixel Calibration	0	0.8
Second Order Zeeman	-	0.4
Other	0	< 0.1
Corrected Gradient	-9.8	2.3
Known Redshift	-10.9	<0.1

Table 6.1: Gradient Systematic Budget. Fractional frequency gradients and corresponding uncertainties. Fractional frequencies denoted with '-' are corrected on a pixel-by-pixel basis during initial data processing (Fig. 3a). The corrected gradient has known systematics removed with uncertainty given by the quadrature sum of all correction uncertainties.

Chapter 7

Lattice Light Shifts

While the proposal of trapped ion clocks came as early as 1982 [41], the development of the neutral atom frequency standards came significantly later. In the late 1990's, the quantum optics community was beginning to wrestle with the issue of far off resonant traps (FORTs) providing deleterious AC Stark shifts for different electronic states [153]. In tandem, interest was growing in the use of forbidden transitions (specifically $^1S_0 \rightarrow ^3P_1$ transitions) for frequency references. Out of these ideas came the proposal to trap strontium atoms in a 1D lattice at the 'magic wavelength', where the perturbation to ground and excited clock states (now $^1S_0 \rightarrow ^3P_0$) were equal. This allowed Doppler-free confinement of neutral atoms without differential lattice induced AC Stark shifts (lattice light shifts). The idea would be expanded to other Alkaline-Earth and Alkaline-Earth like atoms, with an initial flurry and race amongst national labs to establish new atoms.

Ultimately the idea of a 'magic wavelength', as with all physics, is an imperfect approximation to the world around us. While the magic wavelength condition may be satisfied in the dipole approximation, higher order perturbations lead to an over-confined problem - for a thermal sample, insufficient degrees of freedom exist to ensure each atom experiences no differential AC Stark shift from the lattice. Magnetic dipole and electric quadrapole terms, as well as higher order intensity terms (hyperpolarizability) lead to challenging trapping requirements in order to achieve inaccuracy at the 10^{-18} level. In the 1D clock, evaluation of atomic wavefunctions is necessary to properly account for the average potential experienced by the atoms and corresponding light shifts. Unfortunately, this is far more complicated than previous linear light shift models [109].

The newest version of Sr1 has been built with the goal of studying lattice light shifts. From the beginning, the Sr1 system was designed to utilize shallow trap depths ($\sim$ 10 E_r), effectively eliminating hyperpolarizability contributions. This places Sr1 in the position to carefully study lattice light shifts scaling as $\sqrt{u}$ and u (u being trap depth in units of E_r). Towards this we will first review the origins of the lattice light shift, referencing the work of [28, 107]. We will then discuss possible approaches towards lattice light shift evaluations in the Sr1 system.

7.1 AC Stark Shift From Electric Dipole Interaction - π Transitions

We begin our discussion of the lattice light shift by first focusing on the AC Stark effect arising from the differential electric dipole (E1) polarizability between the ground and excited state. The corresponding clock shift in frequency for $\Delta m_F = 0$ transitions is given by [147]

$$\Delta\nu^{E1} = (\Delta\kappa^s + \Delta\kappa^v m_F \xi \vec{e_k} \cdot \vec{e_B} + \Delta\kappa^t \beta) U_0. \tag{7.1}$$

Here we have used irreducible tensors to explicitly give the scalar, vector, and tensor shift contributions as $\Delta\kappa^s$, $\Delta\kappa^v$, and $\Delta\kappa^t$ respectively. $\vec{e_k}$ and $\vec{e_B}$ are the unit vectors along the lattice propagation wavevector and quantization axis (as defined by an external bias field) respectively. ξ is the degree of circularity and is given by $\xi\vec{e_k} = i\vec{\epsilon} \times \vec{\epsilon^*}$ where $\vec{\epsilon}$ is the complex polarization unit vector. Finally $\beta = (3|\vec{\epsilon} \cdot \vec{e_B}|^2 - 1)[3m_F^2 - F(F+1)]$.

From Equation 7.1 we connect with the traditional approach of operating the 1D optical lattice clock. Consider the vector shift contribution. We ensure excellent rejection of this perturbation three ways. First, during clock operation we probe opposite m_F states, where the average frequency of the two rejects the vector shift. Second, we use linearly polarized light ($\xi \approx 0$). Third, we operate with the bias field as close to perpendicular to the lattice wavevector as possible ($\vec{e_k} \cdot \vec{e_B} \approx 0$).

Note that Equation 7.1 must be modified for σ transitions owing to different m_F values between ground and excited clock states [127].

7.2 Atom-Light Hamiltonian

A goal of this chapter is to elucidate the origins of the various lattice light shift terms. We first consider a single electron in an atom, with the atom's center of mass at the origin. We begin with the standard Hamiltonian for an electron interacting with radiation [64, 37, 23, 141],

$$\hat{H} = \frac{1}{2m_e}\big(\hat{\boldsymbol{p}} + e\boldsymbol{A}\big)^2 + V. \tag{7.2}$$

Here m_e is the reduced electron mass, $\hat{\boldsymbol{p}} = -i\hbar\nabla$ is the momentum operator, $\boldsymbol{A}$ the vector potential, and V the Coloumb potential experienced by the electron due to the the atomic nucleus and other electrons. Expanding the square we can rewrite this as

$$\hat{H} = \hat{H}_0 + \hat{W}_1 + \hat{W}_2 \tag{7.3}$$

where

$$\begin{aligned} \hat{H}_0 &= \frac{\hat{\boldsymbol{p}}^2}{2m_e} + V, \\ \hat{W}_1 &= \frac{e}{m}\boldsymbol{A}\cdot\hat{\boldsymbol{p}} \\ \hat{W}_2 &= \frac{q^2}{2m}\boldsymbol{A}^2. \end{aligned} \tag{7.4}$$

$\hat{H}_0$ is the field-free portion of the Hamiltonian (and basis used for calculating the perturbations of the $\hat{W}$ terms). $\hat{W}_1$ is the perturbation that corresponds to first order in $\boldsymbol{A}$. The $\boldsymbol{A}^2$ term is incredibly weak (and a two photon term) - we will discuss this later and instead focus our attention on $\hat{W}_1$. Using the Coloumb gauge ($\nabla\cdot\boldsymbol{A} = 0$), we then have

$$\nabla\cdot\big(\boldsymbol{A}\Psi\big) = \boldsymbol{A}\cdot\big(\nabla\Psi\big) + \big(\nabla\cdot\boldsymbol{A}\big)\Psi \tag{7.5}$$

$$= \boldsymbol{A}\cdot\big(\nabla\Psi\big). \tag{7.6}$$

To proceed we will consider a plane wave interacting with the electron, with vector potential, electric field, and magnetic field given by

$$\begin{aligned}
\boldsymbol{A}(\boldsymbol{r},t) &= \frac{A_0}{2}\left(\boldsymbol{\epsilon}e^{i(\boldsymbol{k}\cdot\boldsymbol{r}-\omega t)} + \boldsymbol{\epsilon}^* e^{-i(\boldsymbol{k}\cdot\boldsymbol{r}-\omega t)}\right) \\
\boldsymbol{E}(\boldsymbol{r},t) &= \frac{iE_0}{2}\left(\boldsymbol{\epsilon}e^{i(\boldsymbol{k}\cdot\boldsymbol{r}-\omega t)} - \boldsymbol{\epsilon}^* e^{-i(\boldsymbol{k}\cdot\boldsymbol{r}-\omega t)}\right) \\
\boldsymbol{B}(\boldsymbol{r},t) &= \frac{iB_0}{2}\frac{\boldsymbol{k}}{k} \times \left(\boldsymbol{\epsilon}e^{i(\boldsymbol{k}\cdot\boldsymbol{r}-\omega t)} - \boldsymbol{\epsilon}^* e^{-i(\boldsymbol{k}\cdot\boldsymbol{r}-\omega t)}\right)
\end{aligned} \tag{7.7}$$

where we recall $\boldsymbol{E}(\boldsymbol{r},t) = -\frac{\partial}{\partial t}\boldsymbol{A}(\boldsymbol{r},t)$ and $\boldsymbol{B}(\boldsymbol{r},\boldsymbol{t}) = \nabla \times \boldsymbol{A}(\boldsymbol{r},t)$. $\boldsymbol{\epsilon}$ specifies the polarization of the plane wave. Following the notation of [64] we can write $\hat{W}_1$ in terms of the transition operator $\hat{D}$.

$$\hat{W}_1 = \frac{eE_0}{2}\left(\hat{D}e^{-i\omega t} - \hat{D}^* e^{+i\omega t}\right) \tag{7.8}$$

where

$$\begin{aligned}
\hat{D} &= \frac{e^{i\boldsymbol{k}\cdot\boldsymbol{r}}}{\omega m_e}\hat{\boldsymbol{p}}\cdot\boldsymbol{\epsilon} \\
&= \frac{1}{\omega m_e}\big(1 + i\boldsymbol{k}\cdot\boldsymbol{r} + ...\big)\hat{\boldsymbol{p}}\cdot\boldsymbol{\epsilon} \\
&= \frac{\hat{\boldsymbol{p}}\cdot\boldsymbol{\epsilon}}{\omega m_e} + \frac{i}{\omega m_e}\big(\boldsymbol{k}\cdot\boldsymbol{r}\big)\big(\hat{\boldsymbol{p}}\cdot\boldsymbol{\epsilon}\big) \\
&= \hat{D}_{E1} + \hat{D}_{QM}.
\end{aligned} \tag{7.9}$$

The electron orbit is much smaller than the wavelength of the optical light we are considering, meaning $\boldsymbol{k}\cdot\boldsymbol{r} << 1$. To this end we break $\hat{D}$ into $\hat{D}_{E1}$ and $\hat{D}_{QM}$ which correspond to dipole (E1) and electric quadrupole (E2)/magnetic dipole (M1) transitions respectively.

Our goal is to now explore the matrix elements corresponding to transitions between states. These will in turn be used to give us our oscillator strength and polarizability for use in AC Stark calculations.

7.2.1 Matrix Elements of $\hat{D}_{E1}$

We define the dipole transition matrix element between two states $|i\rangle$ and $|j\rangle$ as $D_{E1,ij}$.

$$\begin{aligned} D_{E1,ij} &= \langle j| \frac{\hat{\boldsymbol{p}} \cdot \boldsymbol{\epsilon}}{\omega_{ij} m_e} |i\rangle \\ &= \langle j| \hat{\boldsymbol{p}} |i\rangle \cdot \frac{\boldsymbol{\epsilon}}{\omega_{ij} m_e} \\ &= \langle j| \frac{m_e}{i\hbar} \left[\boldsymbol{r}, \hat{H}_0\right] |i\rangle \cdot \frac{\boldsymbol{\epsilon}}{\omega_{ij} m_e} \\ &= -i \langle j| \boldsymbol{r} |i\rangle \cdot \boldsymbol{\epsilon} \end{aligned} \tag{7.10}$$

We have used the Heisenberg equations of motion to handle $\hat{\boldsymbol{p}}$. Also note since we are calculating the dipole transition matrix elements we are interested in the case of resonance radiation currently, setting $\omega = \omega_{ij}$. This is the usual dipole transition, with a dipole moment coupling to the electric field.

7.2.2 Matrix Elements of $\hat{D}_{QM}$

Just like for E1, we define the multipolar (QM) transition matrix element between two states $|i\rangle$ and $|j\rangle$ as $D_{QM,ij}$.

$$D_{QM,ij} = i \langle j| \frac{\left(\boldsymbol{k} \cdot \boldsymbol{r}\right)\left(\hat{\boldsymbol{p}} \cdot \boldsymbol{\epsilon}\right)}{m\omega_{ij}} |i\rangle \tag{7.11}$$

Note this is not a perfect notation since as we will see the QM term is composed of two different transition types, each with their own selection rules: the M1 transition and E2 transition.

A scalar quadruple product has the following relation in 3D Euclidean space:

$$(\boldsymbol{a} \times \boldsymbol{b}) \cdot (\boldsymbol{c} \times \boldsymbol{d}) = (\boldsymbol{a} \cdot \boldsymbol{c})(\boldsymbol{b} \cdot \boldsymbol{d}) - (\boldsymbol{a} \cdot \boldsymbol{d})(\boldsymbol{b} \cdot \boldsymbol{c}). \tag{7.12}$$

allowing us to rearrange (using the commutativity of $\hat{\boldsymbol{p}}$ and $\boldsymbol{\epsilon}$).

$$(\boldsymbol{k} \cdot \boldsymbol{r})(\hat{\boldsymbol{p}} \cdot \boldsymbol{\epsilon}) = (\boldsymbol{k} \times \boldsymbol{\epsilon}) \cdot (\boldsymbol{r} \times \hat{\boldsymbol{p}}) + (\boldsymbol{k} \cdot \hat{\boldsymbol{p}})(\boldsymbol{\epsilon} \cdot \boldsymbol{r}). \tag{7.13}$$

We now focus on each part separately.

7.2.2.1 M1 Transition Elements

We define the transition matrix element for M1 transitions as

$$D_{M1,ij} = i \langle j | \frac{(\boldsymbol{k} \times \boldsymbol{\epsilon}) \cdot (\boldsymbol{r} \times \hat{\boldsymbol{p}})}{m\omega_{ij}} | i \rangle . \tag{7.14}$$

We immediately note that $\hat{\boldsymbol{L}} = (\boldsymbol{r} \times \hat{\boldsymbol{p}})$. Since we have neglected spin to this point in the calculation, we substitute $\hat{\boldsymbol{L}} \rightarrow \hat{\boldsymbol{L}} + 2\hat{\boldsymbol{S}}$ [23]. Additionally, for a plane wave note that $(\boldsymbol{k} \times \boldsymbol{\epsilon}) = k\frac{\boldsymbol{B_0}}{B_0}$ ($\boldsymbol{B_0}$ being the magnetic field of the plane wave). We can then rewrite Equation 7.14 as

$$D_{M1,ij} = \frac{ik}{m_e\omega_{ij}} \langle j | \frac{\boldsymbol{B_0}}{B_0} \cdot \left(\hat{\boldsymbol{L}} + 2\hat{\boldsymbol{S}}\right) | i \rangle . \tag{7.15}$$

This makes it clear that the M1 transition matrix elements couple to the magnetic field.

7.2.2.2 E2 Transition Elements

We define the transition matrix element for E2 transitions as

$$D_{E2,ij} = i \langle j | \frac{(\boldsymbol{k} \cdot \hat{\boldsymbol{p}})(\boldsymbol{\epsilon} \cdot \boldsymbol{r})}{m\omega_{ij}} | i \rangle \tag{7.16}$$

Accounting for all possible options in cartesian coordinates this can be rewritten as

$$D_{E2,ij} = \frac{i}{m\omega_{ij}} \sum_{mn} k_m \epsilon_n \langle j | \hat{p}_m r_n | i \rangle . \tag{7.17}$$

We stop here and note that for a situation like our lattice with a plane wave propagating along $\hat{z}$ and polarization parallel to $\hat{x}$, we get

$$D_{E2,ij} = \frac{i}{m\omega_{ij}} k \langle j | \hat{p}_z x | i \rangle . \tag{7.18}$$

For our 1D lattice setup, this then corresponds to taking the gradient of the electric dipole operator. We then see that while the $E2$ transition couples to the electric field, it does so to the gradient.

For completion, we can rearrange the Equation 7.17 to bring it in line with the form often quoted in the literature. Recalling operator algebra, we note that $\hat{p}_m r_n \psi = (p_n r_n)\psi + r_n(p_m \psi)$. Using this to rewrite Equation 7.17 and recalling $\frac{im_e}{\hbar}[H_0, r] = p$, we find

$$D_{E2,ij} = \sum_{mn} k_m \epsilon_n \langle j | r_m r_n | i \rangle . \tag{7.19}$$

7.2.3 Quick Notes on Order of Magnitudes

7.2.3.1 Order of Magnitude: E1 vs QM

In our derivation we found the QM transitions by including the next order expansion term $\boldsymbol{k} \cdot \boldsymbol{r}$. We can estimate the ratio $R_{QM/E1}$ of the QM to E1 transition matrix elements as

$$\begin{aligned} R_{QM/E1} &= kr \\ &\approx \frac{2\pi}{\lambda} a_0 \\ &\approx 10^{-3} \end{aligned} \tag{7.20}$$

where $\lambda = 813$ nm. Since the AC Stark shift corresponds to these transition matrix elements squared, that means the QM terms are nearly order $\approx 10^{-6}$ relative to the E1 terms. This is a pedagogical argument that is consistent with the 10^{-6} value found in the literature [7].

Importantly, this tells us we are safe to ignore the next order expansion term corresponding to $(\boldsymbol{k} \cdot \boldsymbol{r})^2$, since for depths of ~ 10 E_r the lattice light shift from the QM term is around 1×10^{-18} meaning the next term is a shift at the 1×10^{-24} level or below.

7.2.3.2 Dropping the $\boldsymbol{A}^2$ Term

It is standard to drop the $\boldsymbol{A}^2$ term in the atom-light Hamiltonian. To see why we can ignore $\boldsymbol{A}^2$, we can estimate the ratio R_{A^2} of $e\boldsymbol{A}$ to $\hat{\boldsymbol{p}}$.

$$\begin{aligned} R_{A^2} &= \frac{e\boldsymbol{A}}{\boldsymbol{p}} \\ &\approx \frac{eE_0/\omega}{\hbar} \\ &\approx \frac{\hbar\Omega}{\hbar\omega} \\ &\approx 10^{-8} \end{aligned} \tag{7.21}$$

We find this estimate assuming a Rabi frequency of 10 MHz and optical frequency of 1×10^{15}. Even compared to the M1/E2 term coming from $\boldsymbol{k} \cdot \boldsymbol{r}$, R_{A^2} is negligible and safe to ignore.

Finally, note that $\boldsymbol{A}^2$ has no atomic part and thus cannot lead to transitions [141].

7.3 AC Stark Shift From E1, M1, and E2

In the previous section we explored the origin of the E1, M1, and E2 transitions matrix elements, essential for calculating oscillator strengths between atomic transitions. Now we are interested in the question of the perturbation on the atomic energy levels arising from off-resonant radiation - the AC Stark effect. Recall that this is a second order perturbation in field, corresponding to intensity.

The AC Stark shift is given by [64]

$$\begin{aligned} \Delta E_{AC} &= -\frac{\alpha(\omega)}{4} E_0^2 \\ &= -\frac{\alpha(\omega)}{2} \frac{I}{\epsilon_0 c} \\ &= -\frac{e^2 I}{2\epsilon_0 c m_e} \sum_{j \neq i} \frac{f_{ji}^{opt}}{\omega_{ji}^2 - \omega^2} \end{aligned} \tag{7.22}$$

where I in the intensity of the radiation, given by $E_0^2 = \frac{2I}{\epsilon_0 c}$. α is the polarizability. f_{ji}^{opt} is given by [64]

$$f_{ji}^{opt} = \frac{2W_{ji}}{E_h} \left| \frac{D_{ji}}{a_0} \right|^2, \tag{7.23}$$

where E_h is the Hartree energy and $W_{ji} = E_j - E_i$. Finally combining all the relevant D_{ji} contributions we arrive at the AC Stark shift using the matrix elements we have calculated.

$$\begin{aligned}\Delta E_{AC} &= \frac{e^2 I}{E_h \epsilon_0 c m_e} \sum_{j \neq i} \frac{W_{ji}}{\omega_{ji}^2 - \omega^2} \left| \frac{D_{ji}}{a_0} \right|^2 \\ &= \frac{e^2 I}{E_h \epsilon_0 c m_e} \sum_{j \neq i} \frac{W_{ji}}{\omega_{ji}^2 - \omega^2} \left(\left| \frac{D_{E1,ji}}{a_0} \right|^2 + \left| \frac{D_{M1,ji}}{a_0} \right|^2 + \left| \frac{D_{E2,ji}}{a_0} \right|^2 \right)\end{aligned} \tag{7.24}$$

Typically for the dipole approximation one only considers $D_{E1,ji}$, but it is clear that we have M1 and E2 contributions as well.

Recall the electric field for a standing wave along z (we'll discuss the transverse confinement in the following sections):

$$\boldsymbol{E}(z,t) = 2E_0 \boldsymbol{\epsilon} \cos(kz) \cos(\omega t). \tag{7.25}$$

We now need to account for the spatial position of our atoms along z, carefully considering how each polarizablity term couples. Considering the strength of $E1$ relative to the other terms, the atoms are trapped at the potential maxima to excellent approximation. Thus, our spatial distribution is defined by the E1 polarizability which couples to the potential corresponding to electric field ($\propto \cos^2(kz)$). The M1 polarizability, dependent on the magnetic field, and E2 polarizability, dependent on the gradient of the electric field, are both $\propto \sin^2(kz)$. Since the M1 and E2 have the same spatial dependence in our lattice, we combine them into one QM polarizability term. Finally, we consider the next order perturbation corresponding to 4 photon transitions. Since this is dominated by the $E1$ terms (and fourth order in field), the hyperpolarizability is then $\propto \cos^4 kz$. Combining all of this we arrive at the functional form for the lattice light shift in our 1D system for either the ground $|g\rangle$ or excited $|e\rangle$ clock state.

$$U_{g(e)}^{AC}(I) = -\alpha_{g(e)}^{E1} I \cos^2 kz - \alpha_{g(e)}^{qm} I \sin^2 kz - \beta_{g(e)} I^2 \cos^4 kz \tag{7.26}$$

where $\alpha_{g(e)}^{E1}$ is the dipole polarizability, $\alpha_{g(e)}^{QM}$ is the multipolarizability corresponding to $M1$ and $E2$, and $\beta_{g(e)}$ is the hyperpolarizability. Note that additional corrections for radial dimensions are

discussed next. In the 1D clock system, this corresponds to modifying the intensity terms by a a Gaussian.

With Equation 7.26 we now have the general form of the lattice light induced AC Stark shift essential for deriving lattice light shift models [107, 7].

7.4 Harmonic Model

It is important to have a model for our lattice light shift study that is readily understood by physicists using standard analysis techniques. As such we will first approximate our optical lattice as a harmonic trap. Such an approach is not new and has undergone theoretical development in [114, 71, 28]. For the reader who wishes to jump ahead, we will be deriving Equation 2 in [28], which is what we will call the **harmonic model**. This section will detail exactly how to arrive at this equation used in the aforementioned references, ensuring we can connect upcoming experimental analysis with the results of Chapter 2 as well as the work of the NIST and Riken clock groups.

We first write the 1D optical potential $U_{lat}(\rho, z)$ as

$$U_{lat}(\rho, z) \approx -U_0 e^{-\kappa^2 \rho^2} \cos^2(kz), \tag{7.27}$$

where $\kappa = \frac{\sqrt{2}}{\omega_0}$. We use cylindrical coordinates, with z the axial direction and ρ describing the radial direction. We assume radial symmetry and a lattice waist ω_0. We rewrite Equation 7.26 using the spatial form of the potential given in Equation 7.27. Recall that we are using $g(e)$ to denote the ground(excited) clock state. Also recall that we are still only describing the potential - we haven't included atomic wavefunctions or spatial expectation values.

$$\begin{aligned} U^{AC}_{g(e)}(I) &= -\alpha^{E1}_{g(e)} I(\rho, z) \cos^2 kz - \alpha^{qm}_{g(e)} I(\rho, z) \sin^2 kz - \beta_{g(e)} I(\rho, z)^2 \cos^4 kz \\ &= -\alpha^{E1}_{g(e)} I_0 e^{-\kappa^2 \rho^2} \cos^2 kz - \alpha^{qm}_{g(e)} I_0 e^{-\kappa^2 \rho^2} \sin^2 kz - \beta_{g(e)} I_0^2 e^{-2\kappa^2 \rho^2} \cos^4 kz \end{aligned} \tag{7.28}$$

Here I_0 is the peak intensity. We then expand in powers of z and ρ (see Appendix A.2), collecting terms of equal powers.

$$
\begin{aligned}
U^{AC}_{g(e)}(I) = &-\alpha^{E1}_{g(e)} I_0 - \beta_{g(e)} I_0^2 \\
&+ k^2 z^2 (\alpha_{g(e)} I_0 + 2\beta_{g(e)} I_0^2) \\
&- \frac{k^4 z^4}{3} (\alpha_{g(e)} I_0 + 5\beta_{g(e)} I_0^2) \\
&+ \kappa^2 \rho^2 (\alpha^{E1}_{g(e)} I_0 + 2\beta_{g(e)} I_0^2) \\
&- \frac{\kappa^4 \rho^4}{2} (\alpha^{E1}_{g(e)} I_0 + 4\beta_{g(e)} I_0^2) \\
&- \kappa^2 k^2 \rho^2 z^2 (\alpha_{g(e)} I_0 + 4\beta_{g(e)} I_0^2)
\end{aligned}
\tag{7.29}
$$

Note that $\alpha_{g(e)} = \alpha^{E1}_{g(e)} - \alpha^{QM}_{g(e)}$. For a discussion of the coupling of radial/axial terms (z and ρ) see [14, 15, 7].

From Equation 7.29 we first perform standard normal mode analysis to find the radial and axial trapping frequencies. We first find the axial trapping frequency ω_z.

$$
\begin{aligned}
m\omega_z^2 &= \left. \frac{\partial^2 U_{lat}(\rho = 0, z)}{\partial z^2} \right|_{z=0} \\
&= 2k^2 (\alpha I_0 + 2\beta I_0^2)
\end{aligned}
\tag{7.30}
$$

Similarly, we find the radial trapping frequency ω_ρ.

$$
\begin{aligned}
m\omega_\rho^2 &= \left. \frac{\partial^2 U_{lat}(\rho, z = 0)}{\partial \rho^2} \right|_{\rho=0} \\
&= 2\kappa^2 (\alpha^{E1} I_0 + 2\beta I_0^2)
\end{aligned}
\tag{7.31}
$$

Notice that the two are quite similar but with the switch of κ for k and α^{E1} for α. The normal mode analysis for the radial direction is performed at $z = 0$, the node of the α^{qm} term. Hence for purely radial terms α^{qm} contributions are not present.

Now we wish to perform first order perturbation theory and find the motional energies associated with this potential. To make this clear, we write the Hamiltonian for this system.

$$
\begin{aligned}
\hat{H}_{g(e)} &= \hat{H}^{harm}_{g(e)} + \hat{H}'_{g(e)} \\
\hat{H}^{harm}_{g(e)} &= \frac{\hat{p}^2}{2m} + \frac{1}{2}m\left(\omega^2_{z,g(e)}z^2 + \omega^2_{r,g(e)}\rho^2\right) \\
\hat{H}'_{g(e)} &= -\alpha^{E1}_{g(e)}I_0 - \beta_{g(e)}I_0^2 \\
&\quad - \frac{k^4z^4}{3}\left(\frac{m\omega^2_{z,g(e)}}{2k^2} + 3\beta_{g(e)}I_0^2\right) \\
&\quad - \frac{\kappa^4\rho^4}{2}\left(\frac{m\omega^2_{\rho,g(e)}}{2\kappa^2} + 2\beta_{g(e)}I_0^2\right) \\
&\quad - \kappa^2k^2\rho^2z^2(\frac{m\omega^2_{z,g(e)}}{2k^2} + 2\beta_{g(e)}I_0^2\Big)
\end{aligned}
\tag{7.32}
$$

For the harmonic oscillator we know the energies. For $\hat{H}'$ we use first order perturbation theory operating on the harmonic basis.

$$
\begin{aligned}
E_{g(e)} &= E^{harm}_{g(e)} + E'_{g(e)} \\
E_{g(e)} &= \hbar\omega_{z,g(e)}(n_z + \frac{1}{2}) + \hbar\omega_{\rho,g(e)}(n_\rho + 1) \\
E'_{g(e)} &= -\alpha^{E1}_{g(e)}I_0 - \beta_{g(e)}I_0^2 \\
&\quad - \frac{3\hbar^2k^4}{2m^2\omega^2_{\rho,g(e)}}\left(n_z^2 + n_z + \frac{1}{2}\right)\left(\frac{m\omega^2_{z,g(e)}}{2k^2} + 3\beta_{g(e)}I_0^2\right) \\
&\quad - \frac{\hbar^2\kappa^4}{m^2\omega^2_{\rho,g(e)}}\left(\frac{4}{3}n_\rho^2 + \frac{8}{3}n_\rho + 2\right)\left(\frac{m\omega^2_{\rho,g(e)}}{2\kappa^2} + 2\beta_{g(e)}I_0^2\right) \\
&\quad - \frac{\hbar^2\kappa^2k^2}{m^2\omega_{\rho,g(e)}\omega_{z,g(e)}}\left(n_\rho + 1\right)\left(n_z + \frac{1}{2}\right)(\frac{m\omega^2_{z,g(e)}}{2k^2} + 2\beta_{g(e)}I_0^2\Big)
\end{aligned}
\tag{7.33}
$$

In the interest of being pedagogical, we ever so slightly rewrite the perturbed energy to make clear the clock state dependent terms.

$$
\begin{aligned}
E'_{g(e)} = & -\alpha^{E1}_{g(e)} I_0 - \beta_{g(e)} I_0^2 \\
& - \frac{k^2 E_{rec}}{m}\left(n_z^2 + n_z + \frac{1}{2}\right)\left(\frac{m}{2k^2} + 3\frac{\beta_{g(e)}}{\omega^2_{\rho,g(e)}} I_0^2\right) \\
& - \frac{\hbar^2\kappa^4}{2m^2}\left(\frac{4}{3}n_\rho^2 + \frac{8}{3}n_\rho + 2\right)\left(\frac{m}{2\kappa^2} + 2\frac{\beta_{g(e)}}{\omega^2_{\rho,g(e)}} I_0^2\right) \\
& - \frac{2\kappa^2 E_{rec}}{m}\left(n_\rho + 1\right)\left(n_z + \frac{1}{2}\right)\left(\frac{m\omega_{z,g(e)}}{2k^2\omega_{\rho,g(e)}} + 2\frac{\beta_{g(e)}}{\omega_{\rho,g(e)}\omega_{z,g(e)}} I_0^2\right)
\end{aligned}
\tag{7.34}
$$

We have now written the energies associated with motional quanta in our trap, using first order perturbation theory, for the ground(excited) clock state. We will assume in our analysis that the harmonic quantum numbers (n_z and n_ρ) do not change. This is true assuming single particle physics and no radial/axial coupling. We now wish to find the lattice light shift in our system coming from the difference in trapping conditions between the excited and ground clock state. We will use $\Delta\alpha^{E1} = \alpha_e^{E1} - \alpha_g^{E1}$, $\Delta\beta = \beta_e - \beta_g$, $\Delta\alpha^{QM} = \alpha_e^{QM} - \alpha_g^{QM}$, $\Delta\omega_z = \omega_{z,e} - \omega_{z,g}$, and $\Delta\omega_\rho = \omega_{\rho,e} - \omega_{\rho,g}$.

$$
\begin{aligned}
\Delta E &= E_e - E_g \\
\Delta E &= \hbar\Delta\omega_z(n_z + \frac{1}{2}) + \hbar\Delta\omega_\rho(n_\rho + 1) \\
& - \Delta\alpha^{E1} I_0 - \Delta\beta I_0^2 \\
& - \frac{3I_0^2 k^2 E_{rec}}{m}\left(n_z^2 + n_z + \frac{1}{2}\right)\left(\frac{\beta_e}{\omega^2_{z,e}} - \frac{\beta_g}{\omega^2_{z,g}}\right) \\
& - \frac{2I_0^2\kappa^4 E_{rec}}{mk^2}\left(\frac{4}{3}n_\rho^2 + \frac{8}{3}n_\rho + 2\right)\left(\frac{\beta_e}{\omega^2_{\rho,e}} - \frac{\beta_g}{\omega^2_{\rho,g}}\right) \\
& - \frac{\kappa^2 E_{rec}}{k^2}\left(n_\rho + 1\right)\left(n_z + \frac{1}{2}\right)\left(\frac{\omega_{z,e}}{\omega_{\rho,e}} - \frac{\omega_{z,g}}{\omega_{\rho,g}}\right) \\
& - \frac{4I_0^2\kappa^2 E_{rec}}{m}\left(n_\rho + 1\right)\left(n_z + \frac{1}{2}\right)\left(\frac{\beta_e}{\omega_{\rho,e}\omega_{z,e}} - \frac{\beta_g}{\omega_{\rho,g}\omega_{z,g}}\right)
\end{aligned}
\tag{7.35}
$$

According to [71], near the magic wavelength the dipole polarizablity α^{E1} is about 10^6 times larger than the higher order polarizabilities as well as $\Delta\alpha^{E1}$. Additionally, $\alpha_e^{E1} = \Delta\alpha^{E1} + \alpha_g^{E1}$. We thus expand and keep terms to first order in differential polarizablity parameters. From here on out I will use $\alpha^{E1} \approx \alpha_g^{E1}$. We first find $\Delta\omega_z$ and $\Delta\omega_\rho$.

$$\begin{aligned}\hbar\Delta\omega_z(n_z+\frac{1}{2}) &= \sqrt{\frac{E_{rec}I_0}{\alpha^{E1}}}\left(n_z+\frac{1}{2}\right)(\Delta\alpha^{E1}-\Delta\alpha^{QM}+2\Delta\beta I_0)\\ \hbar\Delta\omega_\rho(n_\rho+1) &= \frac{\kappa}{k}\sqrt{\frac{E_{rec}I_0}{\alpha^{E1}}}\left(n_\rho+1\right)(\Delta\alpha^{E1}+2\Delta\beta I_0)\end{aligned} \tag{7.36}$$

We similarly solve for the two lines containing n_z^2 and n_ρ^2.

$$\begin{aligned}\frac{3I_0^2k^2E_{rec}}{m}\left(n_z^2+n_z+\frac{1}{2}\right)\left(\frac{\beta_e}{\omega_{z,e}^2}-\frac{\beta_g}{\omega_{z,g}^2}\right) &= \frac{3}{2}(n_z^2+n_z+\frac{1}{2})\Delta\beta\frac{I_0E_{rec}}{\alpha^{E1}}\\ \frac{2I_0^2\kappa^4E_{rec}}{mk^2}\left(\frac{4}{3}n_\rho^2+\frac{8}{3}n_\rho+2\right)\left(\frac{\beta_e}{\omega_{\rho,e}^2}-\frac{\beta_g}{\omega_{\rho,g}^2}\right) &= \frac{8}{3k^2\omega_0^2}(n_\rho^2+2n_\rho+\frac{3}{2})\Delta\beta\frac{I_0E_{rec}}{\alpha^{E1}}\end{aligned} \tag{7.37}$$

We finish by finding the mixed n_z and n_ρ terms.

$$\begin{aligned}\frac{\kappa^2E_{rec}}{k^2}\left(n_\rho+1\right)\left(n_z+\frac{1}{2}\right)\left(\frac{\omega_{z,e}}{\omega_{\rho,e}}-\frac{\omega_{z,g}}{\omega_{\rho,g}}\right) &= \frac{E_{rec}}{\alpha^{E1}}\frac{\Delta\alpha^{qm}}{\sqrt{2}k\omega_0}\\ \frac{4I_0^2\kappa^2E_{rec}}{m}\left(n_\rho+1\right)\left(n_z+\frac{1}{2}\right)\left(\frac{\beta_e}{\omega_{\rho,e}\omega_{z,e}}-\frac{\beta_g}{\omega_{\rho,g}\omega_{z,g}}\right) &= 4\frac{\Delta\beta}{\sqrt{2}k\omega_0}\frac{I_0E_{rec}}{\alpha^{E1}}\end{aligned} \tag{7.38}$$

Finally, we redefine our polarizabilities to simplify our formula [140].

$$\begin{aligned}\tilde{\alpha}^{E1} &= \Delta\alpha^{E1}E_{rec}/\alpha^{E1}\\ \tilde{\alpha}^{qm} &= \Delta\alpha^{qm}E_{rec}/\alpha^{E1}\\ \tilde{\beta} &= \Delta\beta(E_{rec}/\alpha^{E1})^2\\ u &= I_0\alpha^{E1}/E_{rec}\end{aligned} \tag{7.39}$$

Combining all of the above, we arrive at the harmonic model [28], with each line expressing a different power dependency on u, the trap depth in units of E_{rec}.

$$\begin{aligned}\Delta E = {} & n_5\tilde{\alpha}^{qm}u^0\\ & + [(n_1+n_2)\tilde{\alpha}^{E1}-n_1\tilde{\alpha}^{QM}]u^{1/2}\\ & - [\tilde{\alpha}^{E1}+(n_3+n_4+4n_5)\tilde{\beta}]u\\ & + [2\tilde{\beta}(n_1+n_2)]u^{3/2}\\ & - \tilde{\beta}u^2\end{aligned} \tag{7.40}$$

As in [28] $n_1 = (n_z + 1/2)$, $n_2 = [\sqrt{2}/(k\omega_0)](n_\rho + 1)$, $n_3 = 3/2(n_z^2 + n_z + 1/2)$, $n_4 = [8/(3k^2\omega_0^2)](n_\rho^2 + 2n_\rho + 3/2)$, and $n_5 = 1/(\sqrt{2}k\omega_0)(n_z + 1/2)(n_\rho + 1)$.

7.4.0.1 Radial Treatment of the Riken Model

If a Taylor expansion for ρ in Equation 7.28 is not performed one arrives at the **Riken model** [140, 107]. To account for the radial distribution in the optical trap Ushijima et al. utilize an *effective trap depth*. For a harmonic trap the radial spatial distribution can be described by a temperature dependent Gaussian. They calculate the average trap depth experienced by the thermal distribution and use this in place of an expansion in ρ. Unfortunately, this means they treat the radial dimension as a purely harmonic trap, excluding a quartic correction. As kz and $\kappa\rho$ are a similar magnitude this may be a poor approximation.

In Nemitz et al. [107] they recognize the shortcoming of this approach for samples that aren't sufficiently cold. They instead note that the axial trapping frequency is a probe of the trap depth experienced by an atom at a particular radial position. They perform axial sideband spectroscopy and numerically fit the sidebands for a range of axial trapping frequencies, giving them a numerical estimate of trap depths. This is a clever idea, but worryingly they only query the sidebands for ms timescales to avoid fitting issues that they associate with dephasing effects. Their fitting of the axial sidebands relies on the work done by Blatt [14] which we know does not fully capture the broadening of the sidebands. It is unclear at what level the approach employed by Nemitz et al. is accurate.

Recent theory work has sought to evaluate the error associated with these techniques [7]. It is important to emphasize as well that lattice light shift evaluations are still routinely performed at significantly deeper depths than actual clock operation. While useful for evaluation of atomic coefficients, it is worrying that no depths near clock operation are used, raising question about model extrapolation to operational depth. This is a driving motivation behind the previous and future Sr1 evaluations where we evaluate over a range of trap depths including the operational trap depth. An additional benefit of the new Sr1 system is significantly colder radial temperatures in

comparison with the original Sr1 system as well as other 1D OLCs.

7.5 BO+WKB Model

A challenge in the analysis of the atomic spatial wavefunctions of the 1D OLC system is the treatment of radial and axial modes. Beyond the harmonic approximation the longitudinal and radial degrees of freedom become coupled. Here we give a brief overview of the **BO+WKB model**, described extensively in [7], expanding as necessary. The first premise of the BO+WKB model is to invoke a Born-Oppenheimer approximation in our system. Consider our new Sr1 system, with a waist of $\omega_0 \approx 260$ microns. In this system, the ratio of the radial trapping frequency ν_r to axial trapping frequency ν_z is $\frac{\nu_r}{\nu_z} < \frac{1}{1000}$. We thus first model the atom to be at a fixed radial position ρ and solve the corresponding eigenvalue equation,

$$\left[-\frac{\hbar^2}{2m}\frac{\partial^2}{\partial z^2} + U_{lat}(\rho, z) \right] Z_{n_z}(\rho, z) = U_{n_z}(\rho) Z_{n_z}(\rho, z), \tag{7.41}$$

where U_{n_z} reprsents the n_z eigenvalue and Z_{n_z} the n_z eigenfunction. As mentioned, we wish to solve for Z_{n_z} as a function of ρ owing to the vastly different timescales of axial versus radial motion. To proceed we rewrite Equation 7.27.

$$\begin{aligned} U_{lat}(r, z) &\approx -U_0 e^{-\kappa^2\rho^2} \cos^2(kz) \\ &\approx -U_0 e^{-\kappa^2\rho^2} \left(\frac{1 + \cos(2kz)}{2} \right) \end{aligned} \tag{7.42}$$

The second line of Equation 7.42, upon inserting into Equation 7.41, can be rearranged to match the form of Mathieu's differential equation,

$$\frac{d^2y}{dx^2} + (a - 2q\cos 2x)y = 0, \tag{7.43}$$

with known solutions. From Mathieu's functions, we can impose the additional physical constraint that tunneling is forbidden on the timescales considered, and are then motivated to normalize the Mathieu functions to a single lattice site ($|z| \leq \frac{\pi}{2k}$ where k is the lattice wavenumber).

Renormalizing the Mathieu functions and utilizing a few of their properties, we arrive at the eigenfunctions and eigenvalues

$$\begin{aligned} Z_{n_z}(\rho, z) &= \sqrt{\frac{2k}{\pi}} se_{n_z+1}\left(kz + \frac{\pi}{2}, \frac{D(\rho)}{4}\right), \\ U_{n_z}(\rho) &= E_R\left[b_{n_z+1}\left(\frac{D(\rho)}{4}\right) - \frac{D(\rho)}{2}\right], \end{aligned} \tag{7.44}$$

where se_{n_z+1} and b_{n_z+1} are the even Mathieu functions and their characteristic values. $D(\rho) = (U_0/E_R)e^{-\kappa^2\rho^2}$ where U_0 is the trap depth and E_R is the recoil energy. The eigenvalues $U_{n_z}(\rho)$ are then inserted into the radial eigenvalue equation,

$$\left[-\frac{\hbar^2}{2m}\frac{d^2}{d\rho^2} + U_{n_z}(\rho) + \frac{\hbar^2}{2m}\frac{l^2 - 1/4}{\rho^2}\right] R_{n_\rho l n_z}(\rho) = E_{n_\rho l n_z} R_{n_\rho l n_z}(\rho), \tag{7.45}$$

where l specifies the z component of angular momentum (units of $\hbar$). The eigenvalues are given by $E_{n_\rho l n_z}$ and the eigenfunctions by $R_{n_\rho l n_z}(\rho)$. n_ρ is the radial quantum number.

As Equation 7.45 has no known general solution, Beloy et al. utilize a WKB approximation [7]. They introduce the WKB phase for energy $E < 0$ (corresponding to trapped states) as

$$\phi_{l n_z}(E) = \sqrt{\frac{2m}{\hbar^2}} \int_{\mathbb{R}} \sqrt{E - U_{n_z}(\rho) - \frac{\hbar^2}{2m}\frac{l^2}{\rho^2}}\, d\rho \tag{7.46}$$

where $\mathbb{R}$ denotes taking the integral over real values. Associated with the WKB phase is the condition

$$\phi_{l n_z}(E_{n_\rho l n_z}) = \pi\left(n_\rho + \frac{1}{2}\right). \tag{7.47}$$

Our goal is not to numerically solve for the eigenergies, but rather the density of states (DOS) associated with the radial modes. We identify the density of states of n_ρ for a given n_z and l as equal to $\frac{\phi'_{l n_z}(E)}{\pi}$, with the prime denoting the derivative. Integrating over all l we arrive at the

density of states for a single value of n_z:

$$G_{n_z}(E) = \frac{1}{2}\sqrt{\frac{2m}{\hbar^2}} \int\int_{\mathbb{R}} \frac{1}{\sqrt{E - U_{n_z}(\rho) - \frac{\hbar^2}{2m}\frac{l^2}{\rho^2}}} d\rho dl. \tag{7.48}$$

Following the integration procedures outlined in [7] we find that

$$G_{n_z}(E) = \frac{1}{4}\frac{2m}{\hbar^2}\big[R_{n_z}(E)\big]^2. \tag{7.49}$$

$R_{n_z}(E)$ is the inverse function of $U_{n_z}(\rho)$. Hence $R_{n_z}(U_{n_z}(\rho)) = \rho$. This relates the DOS to the known eigenvalues $U_{n_z}(\rho)$ that we found earlier, leading a numerically tractable method for finding the DOS.

7.6 Evaluating the Atomic Motional Distribution in the Harmonic Model

Earlier we derived the lattice light shift harmonic model. We now outline a method for evaluating the three input parameters u, n_z, and n_ρ in the harmonic model but now accounting for the coupling of ρ and z. This amounts to refining the work done in [14].

To extract information about our trap we will focus on sideband spectroscopy in our optical lattice. Recalling that to excellent approximation our trapping conditions are given by the dipole polarizablity α^{E1}, we rewrite Equation 7.29.

$$U^{AC}(I) \approx -U_0 + k^2 z^2 U_0 - \frac{k^4 z^4}{3} U_0 + \kappa^2 \rho^2 U_0 - \frac{\kappa^4 \rho^4}{2} U_0 - \kappa^2 k^2 \rho^2 z^2 U_0 \tag{7.50}$$

Here $U_0 \approx \alpha^{E1} I_0$. Following our approach in deriving the harmonic model and using Appendices A.1 and A.2, we find the energies E^{E1} for our optical trap,

$$\begin{aligned} E^{E1}(U_0, n_z, n_\rho) \approx -U_0 + \hbar\omega_z(n_z + \frac{1}{2}) + \hbar\omega_\rho(n_\rho + 1) - \frac{E_{rec}}{2}(n_z^2 + n_z + \frac{1}{2}) \\ - \frac{E_{rec}}{2}\frac{\omega_\rho^2}{\omega_z^2}(\frac{4}{3}n_\rho^2 + \frac{8}{3}n_\rho + 2) - E_{rec}\frac{\omega_\rho}{\omega_z}(n_\rho + 1)(n_z + \frac{1}{2}). \end{aligned} \tag{7.51}$$

Seeking to be consistent with Equation G1 of [7], we note that only accounting for the dipole polarizability (Appendix A.1) $\omega_z = 2/\hbar\sqrt{U_0 E_{rec}}$, $\omega_\rho = 2\kappa/\hbar k\sqrt{U_0 E_{rec}}$, and $\omega_z/\omega_\rho = \kappa/k$. We find

$$\begin{aligned} E^{E1}(U_0, n_z, n_\rho) \approx -U_0 + 2\sqrt{U_0 E_{rec}}(n_z + \frac{1}{2}) + 2\sqrt{U_0 E_{rec}}(\kappa/k)(n_\rho + 1) - \frac{E_{rec}}{2}(n_z^2 + n_z + \frac{1}{2}) \\ - E_{rec}\frac{2\kappa^2}{3k^2}(n_\rho^2 + 2n_\rho + 3/2) - E_{rec}\frac{\kappa}{k}(n_\rho + 1)(n_z + \frac{1}{2}) \end{aligned} \tag{7.52}$$

This is consistent with Equation G1 of [7], except they exclude the radial/axial coupling term. This is done to maintain our usual notion of axial/radial temperature in the calculation of expectation values.

We identify the radial and axial energies which we will need for calculating thermal expectations.

$$\begin{aligned} E_z(U_0, n_z) &\approx \hbar\omega_z(n_z + \frac{1}{2}) - \frac{E_{rec}}{2}(n_z^2 + n_z + \frac{1}{2}) \\ E_\rho(U_0, n_\rho) &= \hbar\omega_\rho(n_\rho + 1) - \frac{E_{rec}}{2}\frac{\omega_\rho^2}{\omega_z^2}(\frac{4}{3}n_\rho^2 + \frac{8}{3}n_\rho + 2) \end{aligned} \tag{7.53}$$

Full modeling of sideband spectra in our system remains an open question, with this section serving to highlight one approach. The probing Rabi frequency, probe time, variation in Rabi frequencies owing to varying Lamb-Dicke parameters with varying trap depth, and more all serve to complicate the single particle physics we are discussing. Early attempts at modeling this system were met with modest at best modeling/experiment agreement in the new system. The low temperatures that enabled resolution of individual n_z states precludes the more readily modeled blurred sidebands of [14]. With the improvement of axial cooling demonstrated in the new system ($\langle n_z = 0 \rangle$), a degree of freedom is removed from modeling which should allow better modeling/experiment agreement. The realization of 100 nK radial temperatures at ~ 10 E_r trap depths (as directly measured via transverse Doppler spectroscopy with the clock laser) will further enhance model agreement. Such work will be critical for the upcoming lattice light shift evaluation.

7.7 Lattice Light Shift Evaluation in the Wannier-Stark Optical Lattice clock

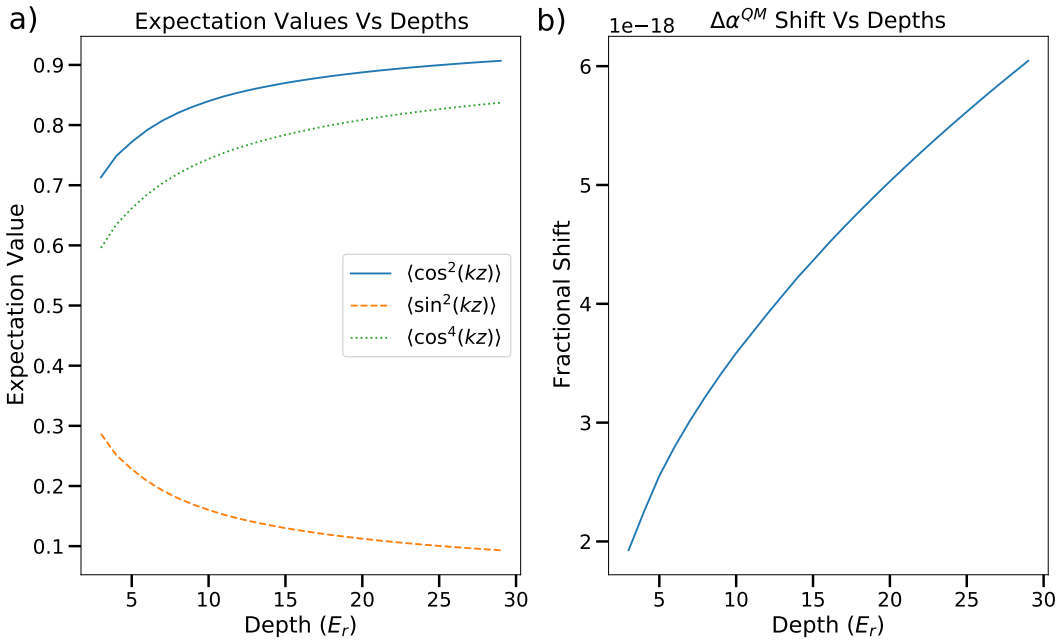

Figure 7.1: Wannier-Stark ground band calculations. **a)** Expectation values calculated for numerically evaluated WS states in 1D. Notice the rapid increase in $\langle\sin^2(kz)\rangle$ at decreasing trap depths - this is the origin of the nonlinear $\Delta\alpha^{QM}$ behavior. **b** Lattice light shift contribution from $\Delta\alpha^{QM}$ versus trap depth. Combined with **a)** we notice both the nonlinear behavior and small magnitude of the shift. For self-comparison stabilities and systematic control resolution of the $\Delta\alpha^{QM}$ shifts presents a formidable challenge.

Shallow trap depth provides a range of benefits for clock operation, reducing lattice light shifts, Raman scattering, density shift systematics, heating, and more. Naturally, a consequence of shallow trap operation is less tightly confined particles in the axial direction, leading to particles deviating further and further from the anti-node of the lattice light. This results in significant non-linear behavior in the M1/E2 perturbations at shallow depths, readily describable using the Wannier-Stark basis discussed in Chapter 5.

In Chapter 5 we derived the Wannier-Stark (WS) states for the 1D optical lattice. Let us

now use those to discuss lattice light shift evaluations in the WS OLC. For our discussion we will explicitly focus on an operational trap depth of $u_{op} = 12\ \mathrm{E}_r$, corresponding to the magic depth introduced in Chapter 5 where the density shift is ≈ 0.

Ignoring radial degrees of freedom we may write the lattice light shift term in the 1D lattice as

$$\Delta h\nu_{LS} = -\Delta\alpha^{E1}\cos^2(kz)u - \Delta\alpha^{QM}\sin^2(kz)u - \cos^4(kz)\Delta\beta u^2. \tag{7.54}$$

Let's consider the Wannnier-Stark states in the position basis z corresponding to the lattice position: $|\psi_{WS}(u)\rangle$. Following Chapter 5, we calculate the wavefunctions at various depths for the ground band. With the wavefunctions in hand we readily calculate the expectation values $\langle\cos^2(kz)\rangle$, $\langle\sin^2(kz)\rangle$, and $\langle\cos^4(kz)\rangle$ with the results shown in Figure 7.1. We see the increasing expectation value of $\langle\sin^2(kz)\rangle$ at shallower depths. Figure 7.1 additionally shows the $\Delta\alpha^{QM}$ fractional shift versus trap depth, clearly showing the $\sqrt{u}$ scaling discussed in the harmonic model.

When OLCs operated with fractional inaccuracies just below 10^{-17}, linear models were used for lattice light evaluations. Operating between two trap depths, $\Delta\alpha^{E1}$ was tuned (via the lattice frequency) to eliminate any differential shift - the so called 'magic wavelength' regime. However, the higher order light shift terms discussed in this chapter have forced experimentalists to move beyond the linear model for accuracy at the 10^{-18} level.

Considering $\Delta\alpha^{QM}$, there are two operational regimes worth discussing at the magic depth. For accuracy, it is preferable to operate at an inflection point of the light shift ($\delta\nu_{LS}/\delta u \approx 0$). Making the lattice light shift first order insensitive to changes in trap depth ensures robustness against fluctuations in experimental conditions. Alternatively, the experimentalist may wish for the most homogeneous trapping conditions possible (for instance for quantum information purposes). In this case one would tune $\Delta\alpha^{E1}$ such that $\nu_{LS} \approx 0$. Both situations may be modeled as discussed earlier, numerically finding the correct $\Delta\alpha^{E1}$ for each. The results are shown in Figure 7.2. Note even in the second case, a 10% variation in trap depth still manifests itself at the 10^{-19} level.

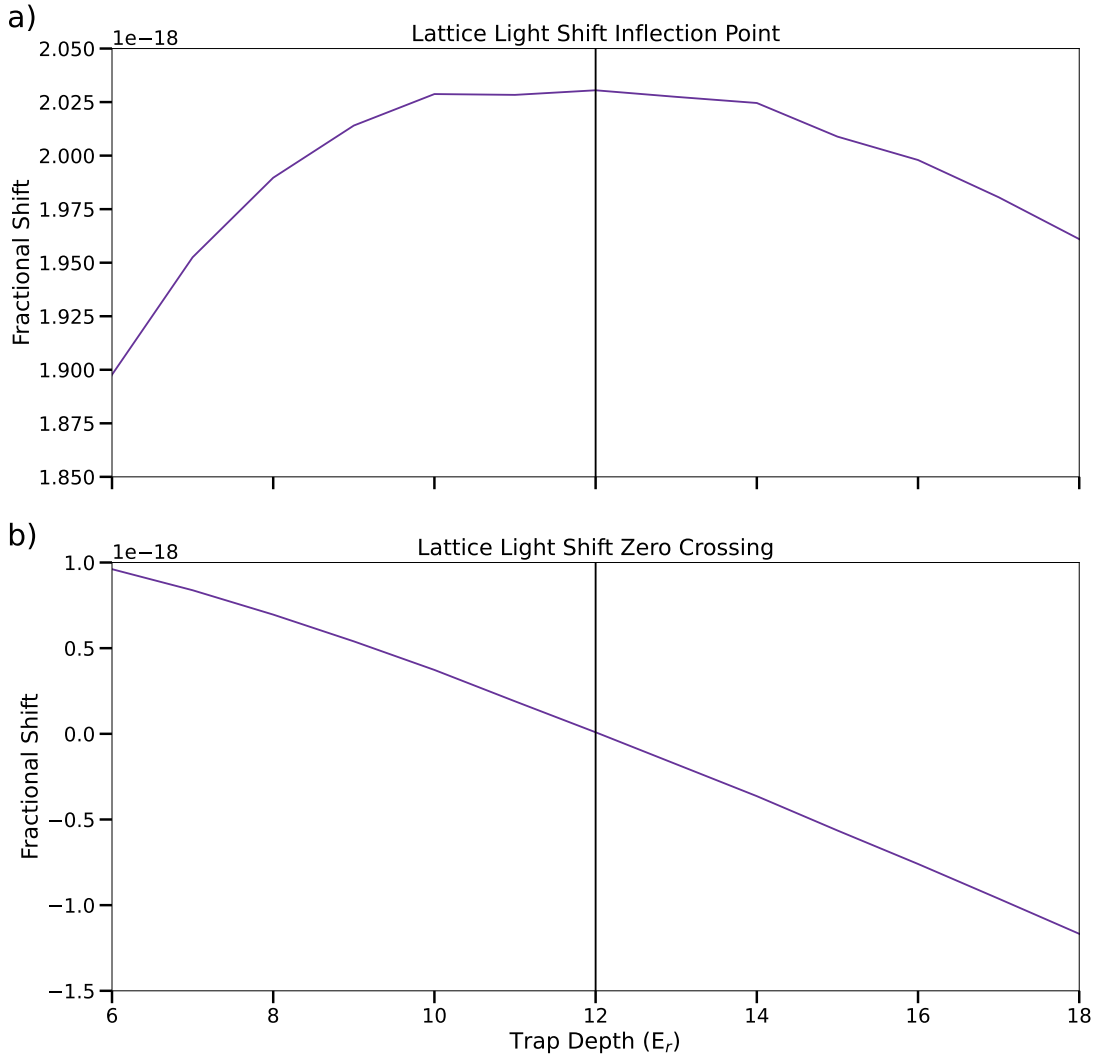

Figure 7.2: Operational regimes at the magic depth ($u = 12$ E$_r$). **a)** For accuracy, operation at the inflection point provides a robust lattice light shift against imperfect experimental conditions. Varying temperatures and atomic wavefunctions modify effective trap depths. Operating in this regime provides the prospect of lattice light shift stability of $\approx 1 \times 10^{-19}$ over a wide range of trap depths. For this simulation the inflection point was found for $\Delta\alpha^{E1} \approx -0.09\Delta\alpha^{QM}$. **b)** For atomic coherence and quantum information uses, operating with the minimal lattice light shift can be ideal. For $\Delta\alpha^{E1} \approx -0.18\Delta\alpha^{QM}$ the lattice light shift goes to zero at the operational depth. Notice the increased slope compared to **a)**. Both regimes are impacted by a mistake in $\Delta\alpha^{QM}$ equally. Both simulations include hyperpolarizability contributions at the level of 1.5×10^{-19}.

Figure 7.2 demonstrates the power of the inflection point. At trap depths of $u = 12 \pm 6$ E_r the lattice light shift varies at the 1×10^{-19} level, suggesting stability of the lattice light shift at the operational depth of Sr1 supports accuracy evaluations well into the 19th decade. **While the inflection point location is robust to small mistakes in $\Delta\alpha^{QM}$, the value of the light shift at the trap depth is not and needs to be evaluated.**

Evaluation of the atomic parameter $\Delta\alpha^{QM}$ is challenging. Consider a traditional lattice shift evaluation as done in Chapter 2, where the trap depth is modulated. Such an evaluation performed at even shallow depths where the radio of M1/E2 to E1 shifts is best is incredibly challenging owning to the minuscule magnitude of light shifts (Figure 7.1). Evaluating to uncertainties below 1×10^{-18} per comparison lacks the sensitivity for resolving $\Delta\alpha^{QM}$ for trap depths between 6 and 30 E_r.

One way to gain sensitivity to $\Delta\alpha^{QM}$ is to operate in a regime where comparison between two different depths results in different contributions from $\Delta\alpha^{QM}$ while the $\Delta\alpha^{E1}$ contribution remain the same - in effect orthogonalizing the two. Considering the $\Delta\alpha^{E1}$ contributions are nearly linear in trap depth, this evaluation method corresponds to changing both high (u_H) and low trap depth (u_L) but maintaining nearly the same difference in trap depth ($\Delta u = u_H - u_L$). The results of such an evaluation are shown in Figure 7.3.

7.7.0.1 Transparency Beam

Even with a careful attempt to decouple $\Delta\alpha^{QM}$ and $\Delta\alpha^{E1}$, the evaluation technique of Figure 7.3 resulted in a poor evaluation of $\Delta\alpha^{QM}$. Considering the complications of the density shift at these depths, this raises serious concerns for the viability of such a study. Nonetheless, the inflection point of Figure 7.2 shows us that given knowledge of $\Delta\alpha^{QM}$ we are well on the way to the next accuracy goal of 5×10^{-19}. In Chapter 6 we showed a level of precision and intra-cloud frequency control sufficient to resolve the gravitational redshift across the atomic sample. How can we use this to aid our evaluation?

One technique would be to use a transparency beam [131]. Application of a laser at 688 nm

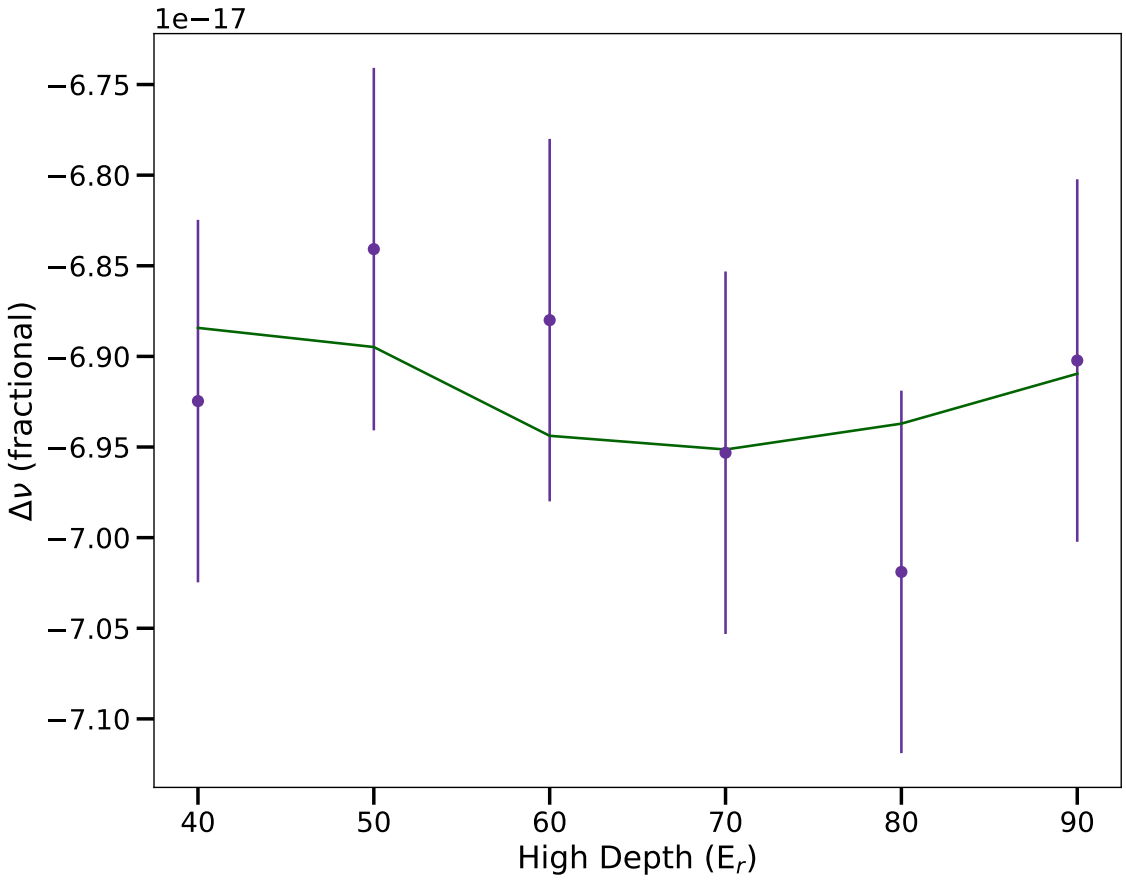

Figure 7.3: $\Delta\alpha^{QM}$ lattice light shift evaluation. To gain greater sensitivity to $\Delta\alpha^{QM}$, varying both high and low trap depths enables nearly constant $\Delta\alpha^{E1}$ lattice light shift contributions with varying $\Delta\alpha^{QM}$ contributions. We explore this by simulating data for $\Delta\alpha^{E1} = -\Delta\alpha^{QM}$. For a high depth of 40 E_r we compare to a low depth of 4 E_r for a $\Delta u = 36$ E_r. As the high depth is increased, the low depth is also increased nearly equally (maintaining Δu), allowing the $\Delta\alpha^{E1}$ contribution to remain nearly constant in each differential evaluation while the $\Delta\alpha^{QM}$ contribution varies, providing a degree of organizational between the two. For the shown data, with uncertainties of 1×10^{-18}, a modest uncertainty of $\delta\Delta\alpha^{QM} = \Delta\alpha^{QM}/2$ is achieved.

slightly detuned from the $^3P_1$ to $^3S_1$ transition shifts the $^3P_1$ state sufficiently far that laser cooling light at 689 nm is no longer resonant. Applying such a beam to a region of the 1D lattice could be used to to allow one region of the trap to remain at the single frequency MOT temperature while a second region can be cooled much further as discussed in Chapter 4. Such a technique

allows 1) modulation of temperature in a thermal manner and 2) the ability to compare the two synchronously. This would move the self comparison stability from $1\times10^{-16}/\sqrt{\tau}$ to $< 1\times10^{-17}/\sqrt{\tau}$, allowing high precision evaluation of shifts at shallow depths where density shifts are tamable.

Chapter 8

Conclusions and Outlook

The work presented in this thesis details an extended exploration of the frontiers of atomic clocks. To summarize, we discussed:

(1) Record low fractional frequency inaccuracy of 2.0×10^{-18} for a Sr OLC and third lowest inaccuracy to date.

(2) First clock ratios between different species with 18 digits of accuracy.

(3) Record low instability comparisons between two independent clocks ($3.5 \times 10^{-17}/\sqrt{\tau}$).

(4) Record low intra-clock instability ($4.4 \times 10^{-18}/\sqrt{\tau}$).

(5) Evaluation of a differential frequency uncertainty to 21 digits (previous record was 19 digits).

(6) First ever observation of the gravitational redshift within a single atomic clock.

(7) Demonstration of 1D OLC operation free of atomic-interaction induced frequency shifts.

Paving the way for these results was work performed by numerous colleagues, from clock evaluations [109, 98] to breakthroughs in atomic coherence times [33, 93] to collaboration with theorists [76, 26, 1, 34]. Perhaps most vital is the work towards making ultrastable lasers ever more stable [112].

The breakthroughs in precision described in Chapter 6 are only the beginning. Camera noise, not QPN, dominates the readout noise at the current number of atoms (100,000). Improved laser coherence times will immediately enable longer clock interrogation times, further decreasing QPN. Finally, improvements to lattice lifetime will ensure high atom number operation as pulse times move to 10 s and beyond.

Atomic coherence times as reported in Chapter 6 are likely under reported, warranting careful study. Reducing or eliminating the atomic interaction induced dephasing present in the current Ramsey coherence measurements may allow for a deeper understanding of the limits of atomic coherence in the new Sr1 system. A steered Si3 combined with Sr1 may already be an exciting platform for pushing the limits of light-matter interactions.

8.1 Towards Accuracy

A major goal of this thesis thesis is advancing the Sr1 system towards the 19^{th} decade of accuracy. Let's discuss ideal projected systematics (Table 8.1) compared to Chapter 2.

The environmental BBR uncertainty was limited by thermometer calibration and will not be a source of improvement in the reevaluation. As discussed in Chapter 4, an expansion port is ready for installation of a calibrated in-situ temperature sensor, enabling the opportunity reevaluate the calibration over time. The atomic BBR uncertainty has in principle a factor of ~ 5 improvement available by further evaluation of the $^3\text{D}_1$ lifetime [111]. The use of the 6" viewport will readily aid in photon collection, greatly increasing the signal to noise ratio of the measurement as compared to the previous Sr2 evaluations [109, 111].

Many systematics are already sufficient for the next evaluation. As discussed in Chapters 5 and 6 the density shift systematic is removed at the level of Table 8.1. DC Stark is statistically consistent with zero and electrodes enable removal of any residual field. Operation of the system with multi-second pulses further reduces the probe AC Stark effect as well as enables operation with smaller bias fields while still reducing line pulling. This serves to further reduce the 2nd order Zeeman coefficient. Servo error can in principle be reduced but for now we will assume

Table 8.1: Sr1 systematic uncertainty from 2019 and new Sr1 projected uncertainty. ?s denote optimal evaluations that are not guaranteed.

Systematic	Shift (10^{-18})	Uncertainty (10^{-18})	Projected Uncertainty (10^{-18})
BBR (environment)	-4974.1	0.2	0.2
BBR (atomic)	0	1.5	0.3?
Density	-12.3	0.4	<0.1
Lattice AC Stark	-21.3	1.2	0.2?
DC Stark	0	0.3	<0.1
Probe AC Stark	0	<0.1	<0.1
1st order Zeeman	0	<0.1	<0.1
2nd order Zeeman	-176.9	0.2	<0.1
2nd order Doppler	0	<0.1	<0.1
Servo error	0	0.2	0.2
Line pulling	0	<0.1	<0.1
Background gas	-3.7	0.4	0.1
AOM phase chirp	0	<0.1	<0.1
Total	**-5188.3**	**2.0**	0.5?

no improvement. The upgraded vacuum enables 27 second lifetimes for 375°C oven temperature operation, reducing the background gas systematic.

Finally, the lattice AC Stark shift (lattice light shift) will be the other major limiting factor. Uncertainty will be dominated by the $\Delta\alpha^{QM}$ contribution. Assuming we match the Riken measurement uncertainty of 5% (currently in contention with theory), this will lead to an uncertainty of $\sim 2 \times 10^{-19}$ at the magic depth. As a result, the new Sr1 system should fundamentally be able to approach a fractional frequency inaccuracy of 5×10^{-19} (Table 8.1). Cheers!

Bibliography

[1] Alexander Aeppli, Anjun Chu, Tobias Bothwell, Colin J Kennedy, Dhruv Kedar, Peiru He, Ana Maria Rey, and Jun Ye. Hamiltonian engineering of spin-orbit coupled fermions in a wannier-stark optical lattice clock. arXiv preprint arXiv:2201.05909, 2022.

[2] B. X. R. Alves, Y. Foucault, G. Vallet, R. Le Targat, and J. Lodewyck. Background collisional shift on lattice-trapped strontium atoms. EFTF Conference Proceedings, 2019.

[3] Neil W Ashcroft, N David Mermin, et al. Solid state physics, 1976.

[4] Marcis Auzinsh, Dmitry Budker, and Simon Rochester. Optically polarized atoms: understanding light-atom interactions. Oxford University Press, 2010.

[5] BT Barnes, WE Forsythe, and EQ Adams. The total emissivity of various materials at $100 - 500°$C. JOSA, 37(10):804–807, 1947.

[6] K Beloy, N Hinkley, Nate B Phillips, Jeffrey A Sherman, Marco Schioppo, J Lehman, A Feldman, Leonard M Hanssen, Christopher W Oates, and Andrew D Ludlow. Atomic clock with $1{\times}10^{-18}$ room-temperature blackbody stark uncertainty. Phys. Rev. Lett., 113(26):260801, 2014.

[7] K Beloy, WF McGrew, X Zhang, D Nicolodi, RJ Fasano, YS Hassan, RC Brown, and AD Ludlow. Modeling motional energy spectra and lattice light shifts in optical lattice clocks. arXiv preprint arXiv:2004.06224, 2020.

[8] K. Beloy, X. Zhang, W. F. McGrew, N. Hinkley, T. H. Yoon, D. Nicolodi, R. J. Fasano, S. A. Schäffer, R. C. Brown, and A. D. Ludlow. Faraday-shielded dc stark-shift-free optical lattice clock. Phys. Rev. Lett., 120:183201, 2018.

[9] Kyle Beloy, Xiaogang Zhang, William F McGrew, Nathan Hinkley, Tai Hyun Yoon, Daniele Nicolodi, Robert J Fasano, Stefan A Schaeffer, Roger C Brown, and Andrew D Ludlow. Faraday-shielded dc stark-shift-free optical lattice clock. Physical review letters, 120(18):183201, 2018.

[10] Philip R Bevington and D Keith Robinson. Data reduction and error analysis. McGrawâ€“Hill, New York, 2003.

[11] RC Birkebak, E Ma Sparrow, ERG Eckert, and JW Ramsey. Effect of surface roughness on the total hemispherical and specular reflectance of metallic surfaces. Journal of Heat Transfer, 86(2):193–199, 1964.

[12] Michael N Bishof. Understanding atomic interactions in an optical lattice clock and using them to study many-body physics. PhD thesis, University of Colorado at Boulder, 2014.

[13] S. Blatt, A. D. Ludlow, G. K. Campbell, J. W. Thomsen, T. Zelevinsky, M. M. Boyd, J. Ye, X. Baillard, M. Fouché, R. Le Targat, A. Brusch, P. Lemonde, M. Takamoto, F.-L. Hong, H. Katori, and V. V. Flambaum. New limits on coupling of fundamental constants to gravity using ^{87}Sr optical lattice clocks. Phys. Rev. Lett., 100:140801, 2008.

[14] S Blatt, Jan Westenkær Thomsen, GK Campbell, AD Ludlow, MD Swallows, MJ Martin, MM Boyd, and Jun Ye. Rabi spectroscopy and excitation inhomogeneity in a one-dimensional optical lattice clock. Physical Review A, 80(5):052703, 2009.

[15] Sebastian Blatt. Ultracold Collisions and Fundamental Physics with Strontium. University of Colorado at Boulder, 2011.

[16] BJ Bloom, TL Nicholson, JR Williams, SL Campbell, M Bishof, X Zhang, W Zhang, SL Bromley, and J Ye. An optical lattice clock with accuracy and stability at the 10- 18 level. Nature, 506(7486):71–75, 2014.

[17] BJ Bloom, TL Nicholson, JR Williams, SL Campbell, M Bishof, X Zhang, W Zhang, SL Bromley, and J Ye. An optical lattice clock with accuracy and stability at the 10^{-18} level. Nature, 506(7486):71, 2014.

[18] Martha I Bodine, Jean-Daniel Deschênes, Isaac H Khader, William C Swann, Holly Leopardi, Kyle Beloy, Tobias Bothwell, Samuel M Brewer, Sarah L Bromley, Jwo-Sy Chen, et al. Optical atomic clock comparison through turbulent air. Physical Review Research, 2(3):033395, 2020.

[19] Tobias Bothwell, Dhruv Kedar, Eric Oelker, John M Robinson, Sarah L Bromley, Weston L Tew, Jun Ye, and Colin J Kennedy. Jila sri optical lattice clock with uncertainty of 2.0×10^{-18}. Metrologia, 56(065004):16pp, 2019.

[20] Tobias Bothwell, Colin J Kennedy, Alexander Aeppli, Dhruv Kedar, John M Robinson, Eric Oelker, Alexander Staron, and Jun Ye. Resolving the gravitational redshift within a millimeter atomic sample. Nature, 2022.

[21] Martin M Boyd. High precision spectroscopy of strontium in an optical lattice: Towards a new standard for frequency and time. PhD thesis, University of Colorado at Boulder, 2007.

[22] Martin M Boyd, Tanya Zelevinsky, Andrew D Ludlow, Sebastian Blatt, Thomas Zanon-Willette, Seth M Foreman, and Jun Ye. Nuclear spin effects in optical lattice clocks. Physical Review A, 76(2):022510, 2007.

[23] Brian Harold Bransden, Charles Jean Joachain, and Theodor J Plivier. Physics of atoms and molecules. Pearson education, 2003.

[24] Samuel M Brewer, J-S Chen, Aaron M Hankin, Ethan R Clements, Chin-wen Chou, David J Wineland, David B Hume, and David R Leibrandt. Al+ 27 quantum-logic clock with a systematic uncertainty below 10- 18. Physical review letters, 123(3):033201, 2019.

[25] Sarah L Bromley. Many-Body Physics in an Optical Lattice Clock. PhD thesis, University of Colorado at Boulder, 2018.

[26] SL Bromley, S Kolkowitz, T Bothwell, D Kedar, A Safavi-Naini, ML Wall, C Salomon, AM Rey, and J Ye. Dynamics of interacting fermions under spin–orbit coupling in an optical lattice clock. Nature Physics, 14(4):399–404, 2018.

[27] R. C. Brown, N. B. Phillips, K. Beloy, W. F. McGrew, M. Schioppo, R. J. Fasano, G. Milani, X. Zhang, N. Hinkley, H. Leopardi, T. H. Yoon, D. Nicolodi, T. M. Fortier, and A. D. Ludlow. Hyperpolarizability and operational magic wavelength in an optical lattice clock. Phys. Rev. Lett., 119:253001, 2017.

[28] Roger C Brown, Nate B Phillips, K Beloy, William F McGrew, Marco Schioppo, Robert J Fasano, Gianmaria Milani, Xiaogang Zhang, N Hinkley, H Leopardi, et al. Hyperpolarizability and operational magic wavelength in an optical lattice clock. Physical review letters, 119(25):253001, 2017.

[29] Anders Brusch, Rodolphe Le Targat, Xavier Baillard, Mathilde Fouché, and Pierre Lemonde. Hyperpolarizability effects in a sr optical lattice clock. Physical Review Letters, 96(10):103003, 2006.

[30] Gretchen K Campbell, Andrew D Ludlow, Sebastian Blatt, Jan W Thomsen, Michael J Martin, Marcio H G de Miranda, Tanya Zelevinsky, Martin M Boyd, Jun Ye, Scott A Diddams, Thomas P Heavner, Thomas E Parker, and Steven R Jefferts. The absolute frequency of the ^{87}Sr optical clock transition. Metrologia, 45(5):539, 2008.

[31] Gretchen K Campbell, Andrew D Ludlow, Sebastian Blatt, Jan W Thomsen, Michael J Martin, Marcio HG De Miranda, Tanya Zelevinsky, Martin M Boyd, Jun Ye, Scott A Diddams, et al. The absolute frequency of the 87sr optical clock transition. Metrologia, 45(5):539, 2008.

[32] Sara L Campbell. A Fermi-Degenerate Three-Dimensional Optical Lattice Clock. PhD thesis, University of Colorado at Boulder, 2017.

[33] Sara L Campbell, RB Hutson, GE Marti, A Goban, N Darkwah Oppong, RL McNally, L Sonderhouse, JM Robinson, W Zhang, BJ Bloom, et al. A fermi-degenerate three-dimensional optical lattice clock. Science, 358(6359):90–94, 2017.

[34] Anjun Chou. Notes on interactions of ^{87}sr atoms in vertical 1d latttice clock. 2021.

[35] Chin-Wen Chou, David B Hume, Till Rosenband, and David J Wineland. Optical clocks and relativity. Science, 329(5999):1630–1633, 2010.

[36] Chin-wen Chou, DB Hume, JCJ Koelemeij, David J Wineland, and Till Rosenband. Frequency comparison of two high-accuracy al+ optical clocks. Physical review letters, 104(7):070802, 2010.

[37] Claude Cohen-Tannoudji, Bernard Diu, Frank Laloe, and Bernard Dui. Quantum mechanics (2 vol. set), 2006.

[38] Boulder Atomic Clock Optical Network BACON Collaboration. Frequency ratio measurements at 18-digit accuracy using an optical clock network. Nature, 591(7851):564–569, 2021.

[39] Alan Corney. Atomic and laser spectroscopy. Clarendon Press Oxford, 1978.

[40] Robert D Cowan. The theory of atomic structure and spectra. Number 3. Univ of California Press, 1981.

[41] Hans G Dehmelt. Monoion oscillator as potential ultimate laser frequency standard. IEEE transactions on instrumentation and measurement, (2):83–87, 1982.

[42] Pacôme Delva, N Puchades, E Schönemann, F Dilssner, C Courde, Stefano Bertone, F Gonzalez, A Hees, Ch Le Poncin-Lafitte, F Meynadier, et al. Gravitational redshift test using eccentric galileo satellites. Physical review letters, 121(23):231101, 2018.

[43] Andrei Derevianko and Maxim Pospelov. Hunting for topological dark matter with atomic clocks. Nature Physics, 10(12):933, 2014.

[44] Jean-Daniel Deschênes, Laura C Sinclair, Fabrizio R Giorgetta, William C Swann, Esther Baumann, Hugo Bergeron, Michael Cermak, Ian Coddington, and Nathan R Newbury. Synchronization of distant optical clocks at the femtosecond level. Physical Review X, 6(2):021016, 2016.

[45] St Falke, H Schnatz, J S R Vellore Winfred, Th Middelmann, St Vogt, S Weyers, B Lipphardt, G Grosche, F Riehle, U Sterr, and Ch Lisdat. The ^{87}Sr optical frequency standard at PTB. Metrologia, 48(5):399.

[46] Stephan Falke, M. Misera, Uwe Sterr, and Christian Lisdat. Delivering pulsed and phase stable light to atoms of an optical clock. Appl. Phys. B, 107:301–331, 2012.

[47] Jakob Flury. Relativistic geodesy. In Journal of Physics: Conference Series, volume 723, page 012051. IOP Publishing, 2016.

[48] Fabio Franchini. An introduction to integrable techniques for one-dimensional quantum systems. 2017.

[49] Steven M Girvin and Kun Yang. Modern condensed matter physics. Cambridge University Press, 2019.

[50] Markus Glück, Andrey R Kolovsky, and Hans Jürgen Korsch. Wannier–stark resonances in optical and semiconductor superlattices. Physics Reports, 366(3):103–182, 2002.

[51] Markus Glück, AR Kolovsky, Hans Jürgen Korsch, and N Moiseyev. Calculation of wannier-bloch and wannier-stark states. The European Physical Journal D-Atomic, Molecular, Optical and Plasma Physics, 4(3):239–246, 1998.

[52] A Goban, RB Hutson, GE Marti, SL Campbell, MA Perlin, PS Julienne, JP D'incao, AM Rey, and J Ye. Emergence of multi-body interactions in a fermionic lattice clock. Nature, 563(7731):369–373, 2018.

[53] Christian Grebing, Ali Al-Masoudi, Sören Dörscher, Sebastian Häfner, Vladislav Gerginov, Stefan Weyers, Burghard Lipphardt, Fritz Riehle, Uwe Sterr, and Christian Lisdat. Realization of a timescale with an accurate optical lattice clock. Optica, 3(6):563–569, 2016.

[54] Markus Greiner. Ultracold quantum gases in three-dimensional optical lattice potentials. PhD thesis, lmu, 2003.

[55] David J Griffiths and Darrell F Schroeter. Introduction to quantum mechanics. Cambridge University Press, 2018.

[56] Jacopo Grotti, Silvio Koller, Stefan Vogt, Sebastian Häfner, Uwe Sterr, Christian Lisdat, Heiner Denker, Christian Voigt, Ludger Timmen, Antoine Rolland, et al. Geodesy and metrology with a transportable optical clock. Nature Physics, 14(5):437–441, 2018.

[57] Gilbert Grynberg, Alain Aspect, and Claude Fabre. Introduction to quantum optics: from the semi-classical approach to quantized light. Cambridge university press, 2010.

[58] Joseph Carl Hafele and Richard E Keating. Around-the-world atomic clocks: Observed relativistic time gains. Science, 177(4044):168–170, 1972.

[59] John L Hall. Nobel lecture: Defining and measuring optical frequencies. Reviews of Modern Physics, 78(4):1279, 2006.

[60] Theodor W Hänsch. Nobel lecture: passion for precision. Reviews of Modern Physics, 78(4):1297, 2006.

[61] Allan H Harvey, Mark O McLinden, and Weston L Tew. Thermodynamic analysis and experimental study of the effect of atmospheric pressure on the ice point. In AIP Conference Proceedings, volume 1552, pages 221–226. AIP, 2013.

[62] Sven Herrmann, Felix Finke, Martin Lülf, Olga Kichakova, Dirk Puetzfeld, Daniela Knickmann, Meike List, Benny Rievers, Gabriele Giorgi, Christoph Günther, et al. Test of the gravitational redshift with galileo satellites in an eccentric orbit. Physical review letters, 121(23):231102, 2018.

[63] Ingolf V Hertel and Claus-Peter Schulz. Atoms, molecules and optical physics. Springer, 2014.

[64] Ingolf V Hertel and Claus-Peter Schulz. Atoms, molecules and optical physics. Springer, 2015.

[65] I R Hill, R Hobson, W Bowden, E M Bridge, S Donnellan, E A Curtis, and P Gill. A low maintenance Sr optical lattice clock. Journal of Physics: Conference Series, 723(1):012019, 2016.

[66] N Huntemann, C Sanner, B Lipphardt, Chr Tamm, and E Peik. Single-ion atomic clock with 3× 10- 18 systematic uncertainty. Physical review letters, 116(6):063001, 2016.

[67] Ross B Hutson, Akihisa Goban, G Edward Marti, Lindsay Sonderhouse, Christian Sanner, and Jun Ye. Engineering quantum states of matter for atomic clocks in shallow optical lattices. Physical review letters, 123(12):123401, 2019.

[68] Wayne M Itano, James C Bergquist, John J Bollinger, JM Gilligan, DJ Heinzen, FL Moore, MG Raizen, and David J Wineland. Quantum projection noise: Population fluctuations in two-level systems. Physical Review A, 47(5):3554, 1993.

[69] James Jespersen and Jane Fitz-Randolph. From sundials to atomic clocks: understanding time and frequency. Courier Corporation, 1999.

[70] David C Johnston. Noninteracting electrons in a prototypical one-dimensional sinusoidal potential. American Journal of Physics, 88(12):1109–1122, 2020.

[71] Hidetoshi Katori, VD Ovsiannikov, SI Marmo, and VG Palchikov. Strategies for reducing the light shift in atomic clocks. Physical Review A, 91(5):052503, 2015.

[72] Hidetoshi Katori, Masao Takamoto, VG Pal'Chikov, and VD Ovsiannikov. Ultrastable optical clock with neutral atoms in an engineered light shift trap. Physical Review Letters, 91(17):173005, 2003.

[73] Raphael Kaubruegger, Pietro Silvi, Christian Kokail, Rick van Bijnen, Ana Maria Rey, Jun Ye, Adam M Kaufman, and Peter Zoller. Variational spin-squeezing algorithms on programmable quantum sensors. Physical review letters, 123(26):260505, 2019.

[74] Colin J Kennedy, Eric Oelker, John M Robinson, Tobias Bothwell, Dhruv Kedar, William R Milner, G Edward Marti, Andrei Derevianko, and Jun Ye. Precision metrology meets cosmology: improved constraints on ultralight dark matter from atom-cavity frequency comparisons. Physical Review Letters, 125(20):201302, 2020.

[75] Thomas Kessler, Christian Hagemann, C Grebing, T Legero, Uwe Sterr, Fritz Riehle, MJ Martin, L Chen, and J Ye. A sub-40-mhz-linewidth laser based on a silicon single-crystal optical cavity. Nature Photonics, 6(10):687–692, 2012.

[76] S Kolkowitz, SL Bromley, T Bothwell, ML Wall, GE Marti, AP Koller, X Zhang, AM Rey, and J Ye. Spin–orbit-coupled fermions in an optical lattice clock. Nature, 542(7639):66–70, 2017.

[77] Shimon Kolkowitz, Igor Pikovski, Nicholas Langellier, Mikhail D Lukin, Ronald L Walsworth, and Jun Ye. Gravitational wave detection with optical lattice atomic clocks. Physical Review D, 94(12):124043, 2016.

[78] Peter Komar, Eric M Kessler, Michael Bishof, Liang Jiang, Anders S Sørensen, Jun Ye, and Mikhail D Lukin. A quantum network of clocks. Nature Physics, 10(8):582–587, 2014.

[79] Philippe Laurent, Didier Massonnet, Luigi Cacciapuoti, and Christophe Salomon. The aces/pharao space mission. Comptes Rendus Physique, 16(5):540–552, 2015.

[80] Dietrich Leibfried, Rainer Blatt, Christopher Monroe, and David Wineland. Quantum dynamics of single trapped ions. Reviews of Modern Physics, 75(1):281, 2003.

[81] Pierre Lemonde and Peter Wolf. Optical lattice clock with atoms confined in a shallow trap. Physical Review A, 72(3):033409, 2005.

[82] Holly Leopardi, Kyle Beloy, Tobias Bothwell, Samuel M Brewer, Sarah L Bromley, Jwo-Sy Chen, Scott A Diddams, Robert J Fasano, Youssef S Hassan, David B Hume, et al. Measurement of the 27al+ and 87sr absolute optical frequencies. Metrologia, 58(1):015017, 2021.

[83] Holly F Leopardi. Frequency Combs for Precision Optical Metrology. PhD thesis, University of Colorado at Boulder, 2019.

[84] Y-J Lin, Rob L Compton, Karina Jiménez-García, James V Porto, and Ian B Spielman. Synthetic magnetic fields for ultracold neutral atoms. Nature, 462(7273):628–632, 2009.

[85] Jérôme Lodewyck, Michal Zawada, Luca Lorini, Mikhail Gurov, and Pierre Lemonde. Observation and cancellation of a perturbing dc stark shift in strontium optical lattice clocks. IEEE transactions on ultrasonics, ferroelectrics, and frequency control, 59(3):411–415, 2012.

[86] Jérôme Lodewyck, Sławomir Bilicki, Eva Bookjans, Jean-Luc Robyr, Chunyan Shi, Grégoire Vallet, Rodolphe Le Targat, Daniele Nicolodi, Yann Le Coq, Jocelyne Guéna, Michel Abgrall, Peter Rosenbusch, and Sébastien Bize. Optical to microwave clock frequency ratios with a nearly continuous strontium optical lattice clock. Metrologia, 53(4):1123, 2016.

[87] Thomas H Loftus, Tetsuya Ido, Martin M Boyd, Andrew D Ludlow, and Jun Ye. Narrow line cooling and momentum-space crystals. Physical Review A, 70(6):063413, 2004.

[88] Andrew D Ludlow. The strontium optical lattice clock: optical spectroscopy with sub-Hertz accuracy. PhD thesis, University of Colorado at Boulder, 2008.

[89] Andrew D Ludlow, Martin M Boyd, Jun Ye, Ekkehard Peik, and Piet O Schmidt. Optical atomic clocks. Reviews of Modern Physics, 87(2):637, 2015.

[90] Andrew D Ludlow, T Zelevinsky, GK Campbell, S Blatt, MM Boyd, Marcio HG de Miranda, MJ Martin, JW Thomsen, Seth M Foreman, Jun Ye, et al. Sr lattice clock at $1\times$ 10–16 fractional uncertainty by remote optical evaluation with a ca clock. Science, 319(5871):1805–1808, 2008.

[91] Long-Sheng Ma, Peter Jungner, Jun Ye, and John L. Hall. Delivering the same optical frequency at two places: accurate cancellation of phase noise introduced by an optical fiber or other time-varying path. Opt. Lett., 19(21):1777–1779, 1994.

[92] Fouad G Major. The quantum beat: principles and applications of atomic clocks. Springer Science & Business Media, 2007.

[93] G Edward Marti, Ross B Hutson, Akihisa Goban, Sara L Campbell, Nicola Poli, and Jun Ye. Imaging optical frequencies with 100 μ hz precision and 1.1 μ m resolution. Physical review letters, 120(10):103201, 2018.

[94] Michael J Martin. Quantum metrology and many-body physics: pushing the frontier of the optical lattice clock. PhD thesis, University of Colorado at Boulder, 2013.

[95] MJ Martin, M Bishof, MD Swallows, X Zhang, C Benko, J Von-Stecher, AV Gorshkov, AM Rey, and Jun Ye. A quantum many-body spin system in an optical lattice clock. Science, 341(6146):632–636, 2013.

[96] D. G. Matei, T. Legero, S. Häfner, C. Grebing, R. Weyrich, W. Zhang, L. Sonderhouse, J. M. Robinson, J. Ye, F. Riehle, and U. Sterr. 1.5μm lasers with sub-10 mHz linewidth. Phys. Rev. Lett., 118:263202, 2017.

[97] DG Matei, T Legero, S Häfner, Ch Grebing, R Weyrich, W Zhang, L Sonderhouse, JM Robinson, J Ye, F Riehle, et al. 1.5 μ m lasers with sub-10 mhz linewidth. Physical review letters, 118(26):263202, 2017.

[98] WF McGrew, X Zhang, RJ Fasano, SA Schäffer, K Beloy, D Nicolodi, RC Brown, N Hinkley, G Milani, M Schioppo, et al. Atomic clock performance enabling geodesy below the centimetre level. Nature, page 1, 2018.

[99] Tanja E Mehlstäubler, Gesine Grosche, Christian Lisdat, Piet O Schmidt, and Heiner Denker. Atomic clocks for geodesy. Reports on Progress in Physics, 81(6):064401, 2018.

[100] Thomas Middelmann, Stephan Falke, Christian Lisdat, and Uwe Sterr. High accuracy correction of blackbody radiation shift in an optical lattice clock. Phys. Rev. Lett., 109(26):263004, 2012.

[101] William R Milner, John M Robinson, Colin J Kennedy, Tobias Bothwell, Dhruv Kedar, Dan G Matei, Thomas Legero, Uwe Sterr, Fritz Riehle, Holly Leopardi, et al. Demonstration of a timescale based on a stable optical carrier. Physical review letters, 123(17):173201, 2019.

[102] J. Mitroy and J.Y. Zhang. Dispersion and polarization interactions of the strontium atom. Molecular Physics, 108(15):1999–2006, 2010.

[103] Michael F Modest. Radiative heat transfer. Academic press, 2013.

[104] Juan A Muniz, Dylan J Young, Julia RK Cline, and James K Thompson. Cavity-qed measurements of the sr 87 millihertz optical clock transition and determination of its natural linewidth. Physical Review Research, 3(2):023152, 2021.

[105] Warren Nagourney. Quantum electronics for atomic physics and telecommunication. OUP Oxford, 2014.

[106] Takuma Nakamura, Josue Davila-Rodriguez, Holly Leopardi, Jeff A Sherman, Tara M Fortier, Xiaojun Xie, Joe C Campbell, William F McGrew, Xiaogang Zhang, Youssef S Hassan, et al. Coherent optical clock down-conversion for microwave frequencies with 10- 18 instability. Science, 368(6493):889–892, 2020.

[107] Nils Nemitz, Asbjørn Arvad Jørgensen, Ryotatsu Yanagimoto, Filippo Bregolin, and Hidetoshi Katori. Modeling light shifts in optical lattice clocks. Physical Review A, 99(3):033424, 2019.

[108] Nils Nemitz, Takuya Ohkubo, Masao Takamoto, Ichiro Ushijima, Manoj Das, Noriaki Ohmae, and Hidetoshi Katori. Frequency ratio of yb and sr clocks with 5× 10- 17 uncertainty at 150 seconds averaging time. Nature Photonics, 10(4):258–261, 2016.

[109] TL Nicholson, SL Campbell, RB Hutson, GE Marti, BJ Bloom, RL McNally, Wei Zhang, MD Barrett, MS Safronova, GF Strouse, et al. Systematic evaluation of an atomic clock at 2× 10- 18 total uncertainty. Nature communications, 6(1):1–8, 2015.

[110] TL Nicholson, MJ Martin, JR Williams, BJ Bloom, M Bishof, MD Swallows, SL Campbell, and J Ye. Comparison of two independent Sr optical clocks with 1×10^{-17} stability at 10^3 s. Phys. Rev. Lett., 109(23):230801, 2012.

[111] Travis L Nicholson. A new record in atomic clock performance. PhD thesis, PhD thesis, University of Colorado, 2015. https://jila. colorado. edu/yelabs . . . , 2015.

[112] E Oelker, RB Hutson, CJ Kennedy, L Sonderhouse, T Bothwell, A Goban, D Kedar, C Sanner, JM Robinson, GE Marti, et al. Demonstration of 4.8× 10- 17 stability at 1 s for two independent optical clocks. Nature Photonics, 13(10):714–719, 2019.

[113] Frank WJ Olver, Daniel W Lozier, Ronald F Boisvert, and Charles W Clark. NIST handbook of mathematical functions hardback and CD-ROM. Cambridge university press, 2010.

[114] VD Ovsiannikov, VG Pal'chikov, AV Taichenachev, VI Yudin, and Hidetoshi Katori. Multipole, nonlinear, and anharmonic uncertainties of clocks of sr atoms in an optical lattice. Physical Review A, 88(1):013405, 2013.

[115] Nikolaos K Pavlis and Marc A Weiss. A re-evaluation of the relativistic redshift on frequency standards at nist, boulder, colorado, usa. Metrologia, 54(4):535, 2017.

[116] Edwin Pedrozo-Peñafiel, Simone Colombo, Chi Shu, Albert F Adiyatullin, Zeyang Li, Enrique Mendez, Boris Braverman, Akio Kawasaki, Daisuke Akamatsu, Yanhong Xiao, et al. Entanglement on an optical atomic-clock transition. Nature, 588(7838):414–418, 2020.

[117] S. G. Porsev, M. S. Safronova, U. I. Safronova, and M. G. Kozlov. Multipolar polarizabilities and hyperpolarizabilities in the Sr optical lattice clock. Phys. Rev. Lett., 120:063204, 2018.

[118] AM Rey, AV Gorshkov, CV Kraus, MJ Martin, M Bishof, MD Swallows, X Zhang, C Benko, J Ye, ND Lemke, et al. Probing many-body interactions in an optical lattice clock. Annals of Physics, 340(1):311–351, 2014.

[119] Joseph C Richmond. Measurement of thermal radiation properties of solids. NASA SP-31. In Measurement of Thermal Radiation Properties of Solids, volume 31, 1963.

[120] Fritz Riehle. Towards a redefinition of the second based on optical atomic clocks. Comptes Rendus Physique, 16(5):506–515, 2015.

[121] Fritz Riehle, Patrick Gill, Felicitas Arias, and Lennart Robertsson. The cipm list of recommended frequency standard values: guidelines and procedures. Metrologia, 55(2):188, 2018.

[122] Benjamin M Roberts, Geoffrey Blewitt, Conner Dailey, Mac Murphy, Maxim Pospelov, Alex Rollings, Jeff Sherman, Wyatt Williams, and Andrei Derevianko. Search for domain wall dark matter with atomic clocks on board global positioning system satellites. Nature Communications, 8(1):1195, 2017.

[123] MS Safronova, D Budker, D DeMille, Derek F Jackson Kimball, A Derevianko, and Charles W Clark. Search for new physics with atoms and molecules. Reviews of Modern Physics, 90(2):025008, 2018.

[124] MS Safronova, SG Porsev, UI Safronova, MG Kozlov, and Charles W Clark. Blackbody-radiation shift in the Sr optical atomic clock. Physical Review A, 87(1):012509, 2013.

[125] Christian Sanner, Nils Huntemann, Richard Lange, Christian Tamm, Ekkehard Peik, Marianna S Safronova, and Sergey G Porsev. Optical clock comparison for lorentz symmetry testing. Nature, 567(7747):204–208, 2019.

[126] Marco Schioppo, Roger C Brown, William F McGrew, Nathan Hinkley, Robert J Fasano, Kyle Beloy, TH Yoon, Gianmaria Milani, D Nicolodi, JA Sherman, et al. Ultrastable optical clock with two cold-atom ensembles. Nature Photonics, 11(1):48–52, 2017.

[127] C Shi, J-L Robyr, U Eismann, M Zawada, L Lorini, R Le Targat, and J Lodewyck. Polarizabilities of the sr 87 clock transition. Physical Review A, 92(1):012516, 2015.

[128] Anthony E Siegman. Lasers university science books. Mill Valley, CA, 37(208):169, 1986.

[129] Lindsay I Sonderhouse. Quantum Gas Engineering for Atomic Clocks. PhD thesis, University of Colorado at Boulder, 2021.

[130] Daniel A Steck. Quantum and atom optics, 2007.

[131] Simon Stellmer, Benjamin Pasquiou, Rudolf Grimm, and Florian Schreck. Laser cooling to quantum degeneracy. Physical review letters, 110(26):263003, 2013.

[132] M. D. Swallows, M. J. Martin, M. Bishof, C. Benko, Y. Lin, S. Blatt, A. M. Rey, and J. Ye. Operating a ^{87}Sr optical lattice clock with high precision and at high density. IEEE Transactions on Ultrasonics, Ferroelectrics, and Frequency Control, 59(3):416–425, 2012.

[133] Masao Takamoto, Ichiro Ushijima, Noriaki Ohmae, Toshihiro Yahagi, Kensuke Kokado, Hisaaki Shinkai, and Hidetoshi Katori. Test of general relativity by a pair of transportable optical lattice clocks. Nature Photonics, 14(7):411–415, 2020.

[134] Weston L. Tew, Travis Nicholson, and Ross B. Hutson. Calibration of thin-film platinum sensors for use in the JILA Sr II Clock. NIST Technical Note 8046, 2015.

[135] American Society of Heating, Refrigerating and Air-Conditioning Engineers. Fundamentals, IP edition. American Society of Heating, Refrigerating and Air-Conditioning Engineers Inc, pages 1–1, 2009.

[136] Sir William Thomson and Peter Guthrie Tait. Treatise on natural philosophy. 1888.

[137] Guglielmo M Tino, Angelo Bassi, Giuseppe Bianco, Kai Bongs, Philippe Bouyer, Luigi Cacciapuoti, Salvatore Capozziello, Xuzong Chen, Maria L Chiofalo, Andrei Derevianko, et al. Sage: A proposal for a space atomic gravity explorer. The European Physical Journal D, 73(11):1–20, 2019.

[138] P Touboul, B Foulon, B Christophe, and JP Marque. Champ, grace, goce instruments and beyond. In Geodesy for Planet Earth, pages 215–221. Springer, 2012.

[139] Ichiro Ushijima, Masao Takamoto, Manoj Das, Takuya Ohkubo, and Hidetoshi Katori. Cryogenic optical lattice clocks. Nature Photonics, 9(3):185–189, 2015.

[140] Ichiro Ushijima, Masao Takamoto, and Hidetoshi Katori. Operational magic intensity for sr optical lattice clocks. Physical review letters, 121(26):263202, 2018.

[141] Peter Van der Straten and Harold Metcalf. Atoms and molecules interacting with light: Atomic physics for the laser era. Cambridge University Press, 2016.

[142] Léon Van Hove. The occurrence of singularities in the elastic frequency distribution of a crystal. Physical Review, 89(6):1189, 1953.

[143] Gregory H Wannier. Wave functions and effective hamiltonian for bloch electrons in an electric field. Physical Review, 117(2):432, 1960.

[144] P Wcisło, P Morzyński, M Bober, A Cygan, D Lisak, R Ciuryło, and M Zawada. Experimental constraint on dark matter detection with optical atomic clocks. Nature Astronomy, 1(1):0009, 2017.

[145] P. G. Westergaard, J. Lodewyck, L. Lorini, A. Lecallier, E. A. Burt, M. Zawada, J. Millo, and P. Lemonde. Lattice-induced frequency shifts in Sr optical lattice clocks at the 10^{-17} level. Phys. Rev. Lett., 106:210801, 2011.

[146] Ph G Westergaard. Strontium optical lattice clock: In quest of the ultimate performance; horloge a reseau optique au strontium: en quete de la performance ultime. 2010.

[147] Philip G Westergaard, Jérôme Lodewyck, Luca Lorini, Arnaud Lecallier, EA Burt, Michal Zawada, Jacques Millo, and Pierre Lemonde. Lattice-induced frequency shifts in sr optical lattice clocks at the 10- 17 level. Physical review letters, 106(21):210801, 2011.

[148] TJ Wieting and JL DeRosa. Effects of surface condition on the infrared absorptivity of 304 stainless steel. Journal of Applied Physics, 50(2):1071–1078, 1979.

[149] SR Wilkinson, CF Bharucha, KW Madison, Qian Niu, and MG Raizen. Observation of atomic wannier-stark ladders in an accelerating optical potential. Physical review letters, 76(24):4512, 1996.

[150] AM Wittenberg. Total hemispherical emissivity of sapphire. JOSA, 55(4):432–435, 1965.

[151] Xinye Xu, Thomas H Loftus, John L Hall, Alan Gallagher, and Jun Ye. Cooling and trapping of atomic strontium. JOSA B, 20(5):968–976, 2003.

[152] Masami Yasuda and Hidetoshi Katori. Lifetime measurement of the $^3P_2$ metastable state of strontium atoms. Phys. Rev. Lett., 92(15):153004, 2004.

[153] Jun Ye, DW Vernooy, and HJ Kimble. Trapping of single atoms in cavity qed. Physical Review Letters, 83(24):4987, 1999.

[154] Aaron W Young, William J Eckner, William R Milner, Dhruv Kedar, Matthew A Norcia, Eric Oelker, Nathan Schine, Jun Ye, and Adam M Kaufman. Half-minute-scale atomic coherence and high relative stability in a tweezer clock. Nature, 588(7838):408–413, 2020.

[155] Xiaohang Zhang, Michael Bishof, Sarah L Bromley, Christina V Kraus, Marianna S Safronova, Peter Zoller, Ana Maria Rey, and J Ye. Spectroscopic observation of SU(N)-symmetric interactions in Sr orbital magnetism. Science, 345(6203):1467–1473, 2014.

Appendix A

Useful Derivations

A.1 Optical lattice Trap Frequencies

We write down the trapping potential in our optical lattice as

$$U_{lat}(r,z) \approx -U_0 e^{-2r^2/\omega_0^2}\cos^2(kz) \tag{A.1}$$

where U_0 is the peak trap depth, r is the radial position (assuming radial symmetry), ω_0 is the trap waist, k is the lattice wavenumber, and z the axial position along the lattice.

Using normal mode analysis we can then find the axial trapping frequency ω_z as

$$\begin{aligned} m\omega_z^2 &= \left.\frac{\partial^2 U_{lat}(r=0,z)}{\partial z^2}\right|_{z=0} \\ &= 2k^2U_0 \end{aligned} \tag{A.2}$$

and radial trapping frequency ω_ρ as

$$\begin{aligned} m\omega_\rho^2 &= \left.\frac{\partial^2 U_{lat}(r,z=0)}{\partial r^2}\right|_{r=0} \\ &= \frac{4U_0}{\omega_0^2}. \end{aligned} \tag{A.3}$$

Recall that we will usually write our trap depth as u in units recoil energy $E_r = \frac{\hbar^2k^2}{2m}$. We then find the form of ω_z that we will use in our model.

$$\omega_z = \frac{\hbar k^2\sqrt{u}}{m} \tag{A.4}$$

A.2 Harmonic Oscillator Expectation Values

We begin by identifying the position operator $\hat{x}$ in the harmonic basis [55]:

$$\hat{x} = \sqrt{\frac{\hbar}{2m\omega_z}}\left(a^\dagger + a\right) \tag{A.5}$$

where $a(a^\dagger)$ are the standard lowering (raising) operator, m is the mass of the oscillator, and ω_z is the oscillation frequency. In the harmonic basis we then find the following relations.

$$\begin{aligned}
\langle n|\,\hat{x}^2\,|n\rangle &= \frac{\hbar}{m\omega_x}\big(n_x + \frac{1}{2}\big) \\
\langle n|\,\hat{x}^4\,|n\rangle &= \frac{3\hbar^2}{2m^2\omega_x^2}\big(n_x^2 + n_x + \frac{1}{2}\big) \\
\langle n|\,\hat{x}^6\,|n\rangle &= \frac{5\hbar^3}{8m^3\omega_x^3}\big(4n_x^3 + 6n_x^2 + 8n_x + 3\big) \\
\langle n|\,\hat{x}^8\,|n\rangle &= \frac{35\hbar^4}{16m^4\omega_x^4}\big(2n_x^4 + 4n_x^3 + 10n_x^2 + 8n_x + 3\big)
\end{aligned} \tag{A.6}$$

Application of these relations to the axial dimension z is straightforward. Now consider the radial dimension ρ, identifying the radial expectation number $n_\rho = n_x + n_y$. We start with the ρ^2 term. We will assume a 2D isotropic harmonic oscillator, with radial frequency ω_ρ.

$$\begin{aligned}
\langle n|\,\hat{\rho}^2\,|n\rangle &= \langle n|\,\hat{x}^2 + \hat{y}^2\,|n\rangle \\
&= \frac{\hbar}{m\omega_\rho}\big(n_\rho + 1\big)
\end{aligned} \tag{A.7}$$

The expectation for ρ^4 is more tricky owing to the degeneracy of n_ρ. We start by expanding in powers of x and y.

$$\begin{aligned}
\langle n|\,\hat{\rho}^4\,|n\rangle &= \langle n|\,\hat{x}^4 + \hat{y}^4 + 2\hat{x}^2\hat{y}^2\,|n\rangle \\
&= \frac{3\hbar^2}{2m^2\omega_\rho^2}\big(n_x^2 + n_x + n_y^2 + n_y + 1\big) + \frac{2\hbar^2}{m^2\omega_\rho^2}\big(n_x + \frac{1}{2}\big)\big(n_y + \frac{1}{2}\big) \\
&= \frac{\hbar^2}{2m^2\omega_\rho^2}\Big(2n_x^2 - 2n_x n_\rho + 3n_\rho^2 + 5n_\rho + 4\Big)
\end{aligned} \tag{A.8}$$

Notice on the last line we have rewritten $n_y = n_\rho - n_x$. To resolve the aforementioned degeneracy of n_ρ, we take an average over the possible values of n_x.

$$\begin{aligned}
\langle n|\,\hat{\rho}^4\,|n\rangle &= \langle n|\,\hat{x}^4 + \hat{y}^4 + 2\hat{x}^2\hat{y}^2\,|n\rangle \\
&= \frac{\hbar^2}{2m^2\omega_\rho^2}\frac{1}{(n_\rho+1)}\sum_{n_x=0}^{n_\rho}\left(2n_x^2 - 2n_x n_\rho + 3n_\rho^2 + 5n_\rho + 4\right) \\
&= \frac{\hbar^2}{m^2\omega_\rho^2}\left(\frac{4}{3}n_\rho^2 + \frac{8}{3}n_\rho + 2\right)
\end{aligned} \tag{A.9}$$

This is key for reproducing the harmonic model in [28], but is only detailed in [7].

A.3 Expansions

For small x.

$$\begin{aligned}
\cos^2(x) &= 1 - x^2 + \frac{x^4}{3} - \frac{2x^6}{45} + \frac{x^8}{315} \\
\cos^4(x) &= 1 - 2x^2 + \frac{5x^4}{3} - \frac{34x^6}{45} + \frac{13x^8}{63} \\
\sin^2(x) &= x^2 - \frac{x^4}{3} + \frac{2x^6}{45} - \frac{x^8}{315} \\
e^{x} &= 1 + x + \frac{x^2}{2} + \frac{x^3}{6} \\
e^{-a^2x^2} &= 1 - a^2x^2 + \frac{a^4x^4}{2} - \frac{a^6x^6}{6} \\
e^{-2a^2x^2} &= 1 - 2a^2x^2 + 2a^4x^4 - \frac{4a^6x^6}{3}
\end{aligned} \tag{A.10}$$